Now that I have read part of the thesis, it seems to me that the title is a bit generic. did you discuss it with Costas?

If not, I think that mentioning electron neutrinos is kind of necessary.

Search for Sterile Neutrinos at the Short Baseline Neutrino Program

Thesis submitted in accordance with the requirements of the University of Liverpool for the degree of Doctor in Philosophy by

Thomas Ham

December, 2022

Acknowledgements

Abstract

The Short Baseline Neutrino (SBN) program is comprised of three Liquid Argon Time Projection Chamber detectors located along the beam line of the Booster Neutrino Beam at Fermilab. The three detectors are SBND, MicroBooNE and ICARUS and are at 110 m, 470 m and 600 m from the beam source respectively. The program was designed with the goal of either confirming or refuting the existence of light sterile neutrinos, which have been hinted at by the LSND and MiniBooNE experiments as well as results from reactor and gallium based neutrino experiments. The observation of sterile neutrinos would provide physics beyond the Standard Model as well as being a vital component in understanding the mass generation mechanism for neutrinos. One of the defining properties of sterile neutrinos is that they do not weakly interact meaning that direct detection is not viable, however, mixing may occur with the active neutrinos which allows for the appearance and disappearance of active neutrinos to be observed.

The development of electromagnetic shower reconstruction algorithms used in SBND are presented which are crucial for calculating the reconstructed neutrino energy from ν_e CC interactions. The neutrino energy is one of the variables used to calculate the neutrino oscillation probability which is the other major topic that is discussed in this thesis. Assuming a $(3+1)$ neutrino framework, the ν_e appearance and disappearance sensitivities are calculated from a ν_e CC inclusive sample for the SBN program using Monte Carlo events. The ν_e appearance exclusion sensitivities from SBND show a stronger constraint than previous results and the allowed region is compatible with the LSND result. The SBN ν_e disappearance exclusion sensitivity excludes much of the allowed region from the ND280 detector whereas the SBN allowed region is still compatible with that from ND280.

Declaration

Declaration

Contents

Glossary

2p2h 2 Particles 2 Holes.

ADC Analog Digital Converter.

APA Andode Plane Assembly.

ARAPUCA Argon R&D Advanced Program at UniCAmp.

ArgoNeuT Argon Neutrino Test Stand.

BNB Booster Neutrino Beam.

BSM Beyond Standard Model.

CC Charged Current.

CC QE Charged Current Quasi Elastic.

CP charge-parity.

CPA Cathode Plane Assembly.

CRT Cosmic Ray Tagger.

DIS Deep Inelastic Scattering.

DONUT Direct Observation of the Nu Tau.

DUNE Deep Underground Neutrino Experiment.

EM electromagnetic.

ES Elastic Scattering.

Fermilab Fermi National Accelerator Laboratory.

GALLEX Gallium Experiment.

GEANT4 GEometry ANd Tracking.

GENIE Generates Events for Neutrino Interaction Experiments.

ICARUS Imaging Cosmic and Rare Underground Signals.

KARMEN Karlsruhe Rutherford Medium Energy Neutrino.

LAr Liquid Argon.

LArSoft Liquid Argon Software.

LArTPC Liquid Argon Time Projection Chamber.

LEP Large Electron-Positron Collider.

LSND Liquid Scintillator Neutrino Detector.

MC Monte Carlo.

MCT Monte Carlo Template.

MEC Meson Exchange Current.

MicroBooNE Micro Booster Neutrino Experiment.

MiniBooNE Mini Booster Neutrino Experiment.

MINOS Main Injector Neutrino Oscillation Search.

MIP Minimum Ionising Particle.

MSW Mikheyev–Smirnov–Wolfenstein.

NC Neutral Current.

NIST National Institute of Standards and Technology.

P parity.

PDG Particle Data Group.

PDS Photon Detection System.

PMNS Pontecorvo-Maki-Nakagawa-Sakata.

PMT Photo Multiplier Tube.

POT Protons-On-Target.

SAGE Soviet-American Gallium Experiment.

SBN Short Baseline Neutrino.

SBND Short Baseline Near Detector.

SCE Space Charge Effect.

SciBooNE SciBar Booster Neutrino Experiment.

SiPM Silicon Photomultiplier.

SK Super Kamiokande.

SM Standard Model.

SNO Sudbury Neutrino Observatory.

SP Space Point.

T2K Tokai to Kamioka.

TPB Tetraphenyl Butadiene.

TPC Time Projection Chamber.

VUV Vacuum Ultra Violet.

List of Figures

List of Tables

Chapter 1.

Introduction

Neutrinos are a class of neutral leptonic particle that, within the Standard Model (SM), only interact via the weak interaction and gravity [1]. The idea of a neutrino was first proposed in 1930 by Pauli and was not experimentally confirmed until 1956 by Cowan and Reines [2] [3]. Two further types (or flavours) of neutrinos were discovered in 1962 and 2000 by the Alternating Gradient Synchrotron and the Direct Observation of the Nu Tau (DONUT) experiment respectively [4] [5].

Neutrinos were long thought to be massless, but results from the Super Kamiokande (SK) collaboration in 1988 showed that the flavour of a neutrino may oscillate which disabused this idea [6]. Confirmation of neutrino oscillations required non-zero neutrino masses and also helped resolve the long standing *Solar Neutrino Problem* and the *Atmospheric Neutrino Anomaly* [7] [8]. There are, however, still a number of open questions which are of interest to particle physics that are linked to neutrinos, such as;

- The amount, if any, of charge-parity (CP) violation in the lepton sector.
- The absolute mass of the neutrinos.
- The neutrino mass hierarchy.
- The Dirac or Majorana nature of neutrinos. Since neutrinos are neutral particles, it is possible that they may be their own anti-particles (a Majorana particle), a property that would be unique to neutrinos.

- The possible existence of sterile neutrinos which are additional flavours of neutrinos that would only interact via gravity.

this is a bit odd. Oscillations already require physics beyond the SM. why these are worth mentioning again? Are you trying to say something else?

The Majorana nature of neutrinos would allow for neutrinoless double beta decay, a process which does not conserve lepton number [9]. Sterile neutrinos have been hinted at by a number of experiments and are expected to have right handed helicities which is in contrast to the active neutrinos which have all been observed to have left handed helicities [10]. The confirmation of either of these would give direct evidence of physics beyond the SM. All of these question are under active investigation by current and future neutrino experiments.

The focus of this thesis will be on the Short Baseline Neutrino (SBN) program which is currently under development with the main goal being to either confirm or refute the existence of light sterile neutrinos. The SBN program is located at Fermilab and consists of three distinct Liquid Argon Time Projection Chamber (LArTPC) type detectors located along the Booster Neutrino Beam (BNB) beamline [11]. The Short Baseline Near Detector (SBND) will be the nearest detector to the beam source at a distance of a 110 m and is currently under construction with the expectation that data taking will begin in early 2024 [12]. The two other detectors which are part of the SBN program are the Micro Booster Neutrino Experiment (MicroBooNE) detector at 470 m and the Imaging Cosmic and Rare Underground Signals (ICARUS) detector at 600 m from the beam source, both of which are currently taking data. As mentioned, the main goal of the program will be to search for eV scale sterile neutrinos, but there are numerous other aims which include, measuring neutrino-argon interactions (due to the close proximity of SBND to the beam source, the observed statistics will far exceed that of any current dataset), developing large scale LArTPC technology and the search for possible Beyond Standard Model (BSM) processes [13]. All of these will be crucial in the development and physics analysis of future Liquid Argon (LAr) neutrino detectors such as the Deep Underground Neutrino Experiment (DUNE).

The remaining content of this thesis begins with Chapter 2, which gives a brief overview of the ideas and experiments which have lead to the discovery of the three active neutrino flavours. This is then followed by a discussion of the key physics principles describing neutrino behaviour. Finally, the experimental results which are at odds with a 3 flavour paradigm and point towards the presence of sterile neutrinos are considered along with the theory that underpins their possible existence.

Chapter 3 then gives an overview of the SBN program along with the general operating principles of a LArTPC and the BNB. The individual detector specifics and the key components of SBND, MicroBooNE and ICARUS are discussed as well as the expected physics capabilities of the program as a whole.

The different algorithms for calculating the reconstructed electromagnetic (EM) shower energy in SBND that have been developed are presented in Chapter 4. EM shower energy is an important quantity that is used in a number of areas, including calculating the reconstructed neutrino energy. The method that each of the three EM shower reconstruction algorithms that are available as part of the *LArPandoraShower* suite of tools, the *Shower Linear Energy tool*, the *Shower Num Electrons Energy tool* and the *Shower ESTAR Energy tool* use is outlined as well as comparing the reconstruction performance with truth information. The reconstruction performance is validated for showers arising from both electrons and photons as well as evaluating the performance as a function of true shower energy and the direction of a shower within the Time Projection Chamber (TPC).

The necessary inputs, choices, method and results for an oscillation analysis are outlined in Chapter 5 and Chapter 6. First the Monte Carlo (MC) event production and selection are described followed by the systematic uncertainties that are considered. The VALOR framework is used to perform the oscillation analysis with an emphasis on the ν_e appearance and ν_e disappearance channels. Each oscillation channel is considered as an independent analysis and sensitivities are presented from various combinations of detectors and systematic uncertainties. These include exclusion contours and allowed regions for the statistical only case and the case where flux and interaction uncertainties have been included plus an investigation into the possible impact of additional efficiency uncertainties on the exclusion sensitivity.

Chapter 2.

Neutrino Physics

This chapter begins with a historical overview of neutrino flavour discoveries in Section 2.1. Some of the key properties of neutrino physics are then discussed in Section 2.2 along with the associated experiments. These include, helicity, chirality, the weak interaction and neutrino oscillations. Finally, some of the experimental results that point towards the possible existence of light sterile neutrinos are described in Section 2.3 along with possible mass generation mechanisms and neutrino oscillations with the inclusion of sterile neutrino states in Section 2.4.

2.1. A Brief History of Neutrino Flavours

The neutrino was first postulated in 1930 by Pauli in an attempt to explain the continuous energy spectrum observed for the electrons from beta decay experiments [2]. At the time it was assumed that along with the nucleus, an electron was the only other product from beta decays. That is, beta decay was thought to be a two body decay of the form,

$$ {}^{A}_{Z}X \longrightarrow {}^{A}_{Z+1}Y + e^{-}, \tag{2.1} $$

where X and Y are the element undergoing the decay and the resultant element respectively. The continuous energy spectrum of the electron was puzzling as it was expected that the electron would always have a fixed kinetic energy and observing electrons with a range of energies appeared to violate energy conservation. Pauli theorised that in addition to the electron, a neutral particle was also emitted in beta decays and that the sum of the energy of the electron and this neutral particle would be constant [2].

The (electron) neutrino was not experimentally confirmed until 1956 by Cowan and Reines who used a nuclear reactor as their neutrino source [3]. Their detector consisted of two tanks of water in which cadmium chloride had been dissolved, interlaced between three tanks of liquid scintillator. When the electron anti-neutrinos would interact with protons in one of the water tanks via inverse beta decay, a neutron and positron would be produced. The positron would then quickly annihilate with an electron producing two gamma rays. The cadmium would absorb the neutron and then emit a single gamma ray. The liquid scintillator was surrounded by Photo Multiplier Tubes (PMTs) and the signal for the experiment was two gamma rays from the electron-positron annihilation shortly followed by another gamma ray from the absorption of the neutron [3].

The second type of neutrino to be discovered was the muon neutrino by the Alternating Gradient Synchrotron at Brookhaven National Laboratory in 1962. The neutrinos were predominantly produced from charged pion decays which in turn were produced by firing a beam of protons at a beryllium target. The pions were directed in the direction of an iron wall during which they had the chance to decay. The iron wall was designed to absorb muons and other interacting particles. The resulting particles from neutrino interactions were then detected by an aluminium spark chamber located behind the shield. Of the selected events, the majority showed muon-like signatures (e.g. long tracks), with only a small number of events showing shower-like objects. The large disparity between the number of muon-like and electron-like events confirmed that at least two types of neutrino exist. That is the muon neutrino is distinct from the already discovered electron neutrino [4].

Following the discovery of the tau lepton in 1975 by the SLAC National Accelerator Laboratory, the tau neutrino was predicted in order to mirror the structure of the electron and muon lepton both of which have an associated neutrino [14]. The existence of the tau neutrino was eventually confirmed by the DONUT experiment in 2000. The DONUT experiment used a neutrino beam created from the decay of charmed mesons produced by protons from the Tevatron accelerator at Fermi National Accelerator Laboratory (Fermilab). Most of the tau neutrinos were produced from the decay of the D_s meson and the decay from the resulting tau lepton [5].

The three confirmed flavours of neutrinos (ν_e, ν_μ, ν_τ) are consistent with predictions from the SM. The number of ~~expected~~ active neutrinos may be determined from the decay of the Z boson since its lifetime is dependent on the number of flavours. This was shown by the Large Electron-Positron Collider (LEP) experiment, which found the lifetime of the Z boson to be consistent with a three neutrino model [15] [16]. There have, however, been results from experiments which are inconsistent with the 3 neutrino framework. Namely the excess of events observed by the Liquid Scintillator Neutrino Detector (LSND) and Mini Booster Neutrino Experiment (MiniBooNE) experiments, the deficit of events observed by the Soviet-American Gallium Experiment (SAGE) and Gallium Experiment (GALLEX) detectors (dubbed the *Gallium Anomaly*) and the deficit of events observed from nuclear reactors (dubbed the *Reactor Anomaly*) [17] [18] [19] [20] [21] [22]. Additional neutrino flavours may exist and not contradict the statement on the lifetime of the Z boson if they have a mass greater than half that of the Z boson and/or they do not weakly interact and hence do not contribute to the decay rate of the Z boson [15]. The hypothetical neutrinos which do not weakly interact are know as *sterile* neutrinos in order to distinguish them from the *active* ones that do. Sterile neutrinos will be discussed in greater detail in Section 2.3 and Section 2.4.

2.2. Overview of Neutrino Physics

Elementary particles are classified as either fermions or bosons depending on their spin. Fermions have odd half-integer spin whereas bosons have integer spin. Fermions are then sub-divided between leptons and quarks, with one of the defining differences being that quarks experience the strong force along with the other three fundamental forces whereas the leptons only experience gravity, the weak and the electromagnetic forces. Within the SM, bosons are subdivided into vector bosons which have a spin of one and scalar bosons which have a spin of zero [1]. The classification of elementary particles is shown in the flow chart in Figure 2.1.

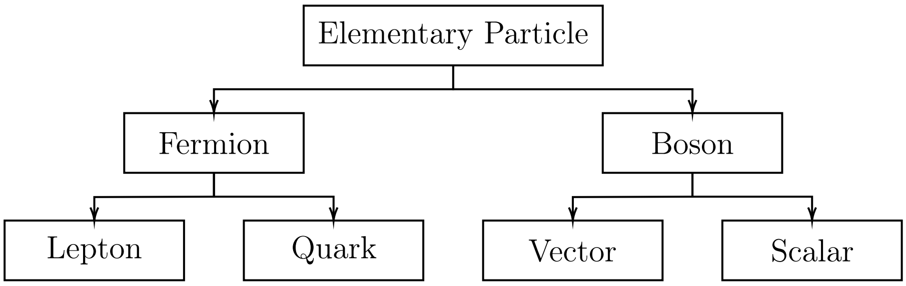

Figure 2.1.: Elementary particle classifications within the SM.

Since neutrinos are neutral fermions, it is possible that neutrinos are their own anti-particle (a Majorana Particle). This idea was first proposed in 1937 by Majorana [23]. Within the SM, all fermions with the possible exception of neutrinos behave as Dirac fermions, that is, the particle and anti-particle are distinct [24]. With the possibility that neutrinos are Majorana in nature, it has lead to the search for neutrinoless double beta decay [25]. This is a variation on ordinary double beta decay in which a nucleus decays by emitting two electrons simultaneously. In ordinary double beta decay there would also be two (anti)neutrinos in the final state, however, if neutrinos are Majorana particles, it can be thought of as one nucleon emitting a neutrino and the other absorbing it hence there are no neutrinos in the final state. Observation of such a decay would confirm the Majorana nature of neutrinos and give direct evidence for physics beyond the SM since the lepton number would not be conserved. Furthermore, neutrino oscillations (which is discussed in Section 2.2.3) are at odds with the SM assumption that neutrinos are massless. With the requirement that neutrinos are indeed massive, the Dirac or Majorana nature of neutrinos is again discussed in Section 2.4.1 within the context of mass generation mechanisms [26].

same comment as in the intro-

2.2.1. Helicity and Chirality

? what is it ? better say "projection along it's propagation direction"

The helicity of a particle is defined as the projection of its spin onto the linear momentum. If the spin is aligned with the direction of motion, the particle is said to be *right-handed* and has an eigenvalue equal to +1 whereas if the spin is aligned in the opposite direction a particle is said to be *left-handed* and has an eigenvalue equal to -1 [27]. It was observed by Goldhaber and others that neutrinos appear to exclusively have left-handed helicities (and right-handed helicities for anti-neutrinos). The experiment they used to determine this was as follows; consider the decay of an isomer of europium via electron capture to an excited state of samarium. The samarium nucleus then decays to its ground state by emitting a photon.

That is true only if the initial momentum is 0. which is the case because the decay by electron capture is dominated by electrons from the s-shell. You have say that the total momentum is 0 or this does not make sense

$$ {}^{152m}Eu + e^- \longrightarrow {}^{152}Sm^* + \nu_e \longrightarrow {}^{152}\ Sm + \gamma \tag{2.2} $$

To conserve momentum, the excited samarium nucleus must recoil in a direction opposite to the emitted neutrino. To conserve angular momentum the spin of the neutrino and the recoiling nucleus must be in opposite directions which means that they both have the same handedness. Finally, the photon emitted will have a spin in the opposite direction to the neutrino and if the photon is emitted in a direction opposite to the neutrino direction, both will have the same helicity. The photons emitted in the direction opposite to the neutrino were identified, their helicity determined and it was found that they were all left-handed [28].

Helicity does commute with the Hamiltonian, however it is not Lorentz invariant (for massive particles) [29]. Since massive particles travel at speeds less than c, it is always possible to boost to a frame such that the direction of motion is reversed. Spin is not affected by this which means that it is possible for the sign of the helicity to change. In contrast to helicity, chirality is a Lorentz invariant quantity that does not commute with the Hamiltonian. The chirality operator is γ^5 and it is defined as $i\gamma^0\gamma^1\gamma^2\gamma^3$ (i.e. i times the product of the gamma matrices). Similarly to helicity, when the chirality operator acts on the eigenfunctions ψ_R and ψ_L it results in an eigenvalue of +1 and -1 respectively. It is commonly expressed in term of projection operators $P_{(L,R)}$ such that,

$$\begin{aligned}\psi_L = P_L\psi \equiv \frac{1-\gamma^5}{2}\psi \\ \psi_R = P_R\psi \equiv \frac{1+\gamma^5}{2}\psi,\end{aligned} \tag{2.3}$$

where ψ is a spinor which can be written in terms of left and right chiral components, $\psi = \psi_L + \psi_R$. By defining $\overline{\psi} \equiv \psi^\dagger\gamma^0$ and noting that $P^\dagger_{(L,R)} = P_{(L,R)}$ and $P_{(L,R)}\gamma^0 = \gamma^0 P_{(R,L)}$, it follows that

$$\overline{\psi_L}\psi_L = \overline{\psi_R}\psi_R = 0. \tag{2.4}$$

It should be noted that for massless particles, helicity is Lorentz invariant and becomes identical to chirality [30].

2.2.2. Weak Interactions and CP violation

The weak force is mediated by the charged $W^\pm$ and neutral Z^0 bosons. It is dubbed *weak* because if the strong or EM forces are also present the weak force is usually subdominant. The active neutrinos only interact via the weak force (and gravity) which is one of the reasons they have been historically difficult to detect.

The weak force has two associated types of interaction: Charged Current (CC) interactions which are mediated by the charged W boson and Neutral Current (NC) interactions which are mediated by the neutral Z boson. The defining difference is that for CC interactions current flows between the interacting fermions (i.e. charge is exchanged), whereas for NC interactions, the total flow of charge between the interacting fermions is zero. The weak component of the SM Lagrangian is therefore comprised of two terms, one representing CC and one representing NC. The CC current, j^{CC}_{weak}, and NC current, j^{NC}_{weak}, components of each of these terms may be expressed as,

$$\begin{aligned} j^{CC}_{weak} &= \frac{g}{\sqrt{2}}\overline{\psi}\gamma^{\mu}P_L\psi, \\ j^{NC}_{weak} &= \frac{g}{2\cos\theta_W}\sum_{i=\nu,l}\overline{\psi}_i\gamma^{\mu}(g^i_V - g^i_A\gamma^5)\psi_i, \end{aligned} \tag{2.5}$$

where g is the weak coupling factor, θ_W is the Weinberg angle, g_V is the vector coupling and g_A is the axial coupling [1] [30] [31]. The weak coupling is related to the Fermi Constant, G_F, and the boson masses such that,

$$\begin{aligned} \frac{g^2}{8m^2_W} &= \frac{G_F}{\sqrt{2}}, \\ \frac{g^2}{8m^2_Z\cos^2\theta_W} &= \frac{G_F}{\sqrt{2}}, \end{aligned} \tag{2.6}$$

where m_W is the mass of the W boson and m_Z is the mass of the Z boson [30].

you haven't explained what that is

It was shown experimentally by Wu that parity (P) conservation is violated and later by Cronin and Fitch that CP conservation is also violated [32] [33]. CP violation is one of the Sakharov conditions required to have a matter-antimatter asymmetry in the universe, however, the amount of CP violation seen in the quark sector is seemingly insufficient to explain the matter dominated universe that is observed [34]. There may also be CP violation from the Pontecorvo-Maki-Nakagawa-Sakata (PMNS) matrix in the lepton sector which could help explain the matter-antimatter asymmetry. However, the amount of CP violation in the lepton sector, if any, is currently unknown [35].

j^{CC}_{weak} has the form of a vector-axial (V–A) interaction, where the vector current is given by $\overline{\psi}\gamma^{\mu}\psi$ and the axial current is given by $\overline{\psi}\gamma^{\mu}\gamma^5\psi$. The axial component remains unchanged under a parity transformation, whereas the sign of the vector component changes. Usually the square of the amplitude is of interest, which in short means taking the square of the weak current. This results in a squared vector and axial component plus a cross term. Since the axial and vector components behave differently under a parity transformation, this cross term leads to parity violation [1] [30]. j_{weak}^{NC} does not have the form of a V–A interaction, but does again have both vector and axial components which lead to parity violation [1].

The SM is constructed such that only the left components of the field couple to the W and Z bosons so it follows that only left-handed particles (and right-handed anti-particles) can weakly interact. Neutrinos only interact via the weak force which means they are therefore produced with a left-handed chirality and since they are ultra-relativistic, for all intents and purposes they also have a left-handed helicity. Additionally, a neutrino that is present in a weak interaction is always in a definite flavour state which corresponds to the associated charged lepton (therefore conserving lepton number) [36].

2.2.3. Neutrino Oscillations

Another unique property of neutrinos are their ability to oscillate. That is, the neutrino flavour may change as it propagates. This phenomenon was first proposed by Pontecorvo in 1957 [37]. In the following years this work was built upon by Maki, Nakagawa, Sakata and Pontecorvo himself [38].

One of the first experimental results to eventually be explained by neutrino oscillations was the Homestake experiment. This was an experiment in the 1960's that was designed to count the number of solar neutrinos. The crux of the experiment was to fill an underground tank with dry-cleaning fluid (perchloroethylene) since it contains chlorine. The solar neutrinos would be detected by inverse beta decay via

$$^{37}Cl + \nu_e \longrightarrow {}^{37}Ar + e^-, \tag{2.7}$$

where the argon would be extracted and counted as it decayed. From this, the number of interacting electron neutrinos was determined, however this number was consistently about a third of the number expected by solar predictions. This inconsistency was later dubbed the *Solar Neutrino Problem* [7].

The ratio of muon to electron neutrinos produced in the atmosphere from the decay of pions and muons was also studied. The predicted rate of neutrinos in the atmosphere was thought to be well understood, however a number of experiments, the most notable of which, SK, all observed ratios significantly below the expected value. This indicated a deficit in the observed muon neutrinos or an excess in electron neutrinos (or both). Mirroring the solar neutrino problem, these observation were dubbed the *Atmospheric Neutrino Anomaly* [8].

In addition to measuring the ratio of atmospheric neutrinos, SK was also able to measure the zenith angle of the incoming neutrinos. This allowed the observed and predicted number of neutrinos to be compared as a function of the zenith angle. It was noted that the number of electron neutrinos agreed reasonably well with the expected value across all angles whereas for low energy muon neutrinos there was a deficit of events for all angles and for high energy muons there was a deficit of events for zenith angles corresponding to large distances travelled (e.g. neutrinos which travelled through the earth and into the detector from below). The observed rate of high energy muons at angles corresponding to travelling directly down from the atmosphere to the detector agreed with predicted values [6].

The results published by SK in 1998 allowed the atmospheric neutrino anomaly to be reconciled with neutrino oscillations and was the first time neutrino oscillations were confirmed to have been observed [6]. Shortly after, in 2001, the Sudbury Neutrino Observatory (SNO) resolved the solar neutrino problem by again explaining the deficit in observed electron neutrinos as a result of neutrino oscillations. The SNO detector was designed with the intention of being able to measure the total neutrino flux (the sum of all three flavours) and the electron neutrino flux in isolation. The detector consisted of a tank of heavy water. Solar neutrinos have sufficient energy to interact via NC interactions with the deuterium in the heavy water regardless of neutrino flavour,

$$\nu + d \longrightarrow \nu + p + n. \tag{2.8}$$

Neutrinos of any flavour may also interact via Elastic Scattering (ES),

$$\nu + e^- \longrightarrow \nu + e^-. \tag{2.9}$$

ES interactions are subdivided into CC and NC components, but since only ν_e's are above the threshold energy for CC interactions, there is no CC component for ν_μ or ν_τ. Therefore, all active neutrino flavours contribute equally to the NC ES flux, but the flux of ν_e's is enhanced due to also having a CC component [39]. Finally, only electron neutrinos may interact via CC,

$$\nu_e + d \longrightarrow p + p + e^-, \tag{2.10}$$

therefore this channel only measured the flux of ν_e. Confirmation that the flux of ν_e was less than the flux from the NC or ES channels coupled with the fact that the ν_e flux was in agreement with previous solar neutrino experiments was sufficient to resolve the solar neutrino problem [40].

Neutrino oscillations is one of the key topics in the field and this thesis. The remainder of this section will discuss the theory of neutrino oscillations. The three flavour states (ν_e, ν_μ, ν_τ) have already been established, but it is expected that the neutrino mass states (ν_1, ν_2, ν_3) are distinct in order to explain neutrino oscillations. The flavour eigenstate of a neutrino is what is observed, however, each flavour state is a superposition of the three mass states. As a neutrino propagates, the relative phase between the mass states is continuously changing. When a neutrino then interacts, the mass states may have a relative phase that is different to that when the neutrino was created. At the point of interaction, the flavour superposition will then collapse into a single flavour and this is what is then detected. This is the mechanism which allows neutrino flavours to oscillate.

The transformation between the flavour and mass states is expressed as

$$|\nu_\alpha\rangle = \sum_k U^*_{\alpha k}|\nu_k\rangle, \tag{2.11}$$

where $\alpha \in$ (e, μ, τ), k $\in$ (1, 2, 3) and U is a unitary matrix. In the case of three flavour neutrino oscillations, U, is known as the PMNS mixing matrix which is a 3×3 matrix representing the three different states [30]. The PMNS matrix is parameterised in terms of three mixing angles ($\theta_{12}, \theta_{13}, \theta_{23}$) and a single physical

Thoughts. You mention the majorana problem many times.

Do we need to mention the additional phases in the PMNS matrix when we have Majorana neutrinos?

CP violating phase, δ_{cp}, as

$$
\begin{aligned}
U &= \begin{pmatrix} U_{e1} & U_{e2} & U_{e3} \\ U_{\mu 1} & U_{\mu 2} & U_{\mu 3} \\ U_{\tau 1} & U_{\tau 2} & U_{\tau 3} \end{pmatrix} \\
&= \begin{pmatrix} 1 & 0 & 0 \\ 0 & c_{23} & s_{23} \\ 0 & -s_{23} & c_{23} \end{pmatrix} \begin{pmatrix} c_{13} & 0 & s_{13}e^{-i\delta_{cp}} \\ 0 & 1 & 0 \\ -s_{13}e^{i\delta_{cp}} & 0 & c_{13} \end{pmatrix} \begin{pmatrix} c_{12} & s_{12} & 0 \\ -s_{12} & c_{12} & 0 \\ 0 & 0 & 1 \end{pmatrix}
\end{aligned}
\tag{2.12}
$$

where $c_{kj} = \cos\theta_{kj}$, $s_{kj} = \sin\theta_{kj}$ and the other 5 phases of the unitary matrix have been absorbed by rephasing the lepton fields.

The time dependent Schrödinger equation is given by

$$
i\frac{\mathrm{d}}{\mathrm{d}t}|\nu_k(t)\rangle = H|\nu_k(t)\rangle, \tag{2.13}
$$

and since neutrino mass states are eigenstates of the Hamiltonian, H, it follows that the solution to Equation 2.13 is given by a plane wave solution

$$
|\nu_k(t)\rangle = e^{-iE_k t}|\nu_k\rangle. \tag{2.14}
$$

The amplitude of a transition, $A_{\nu_\alpha \to \nu_\beta}(t)$, is defined as the projection of the final state onto the initial state, so for flavour oscillations the amplitude is given by

$$
A_{\nu_\alpha \to \nu_\beta}(t) \equiv \langle \nu_\beta | \nu_\alpha(t) \rangle. \tag{2.15}
$$

The probability of transition, $P_{\nu_\alpha \to \nu_\beta}(t)$, is then given by the absolute square of the amplitude

$$
P_{\nu_\alpha \to \nu_\beta}(t) = |A_{\nu_\alpha \to \nu_\beta}(t)|^2. \tag{2.16}
$$

It follows from Equation 2.11 and Equation 2.14 that

$$|\nu_\alpha(t)\rangle = \sum_k U^*_{\alpha k} e^{-iE_k t} |\nu_k\rangle \tag{2.17}$$

and that the transition amplitude is given by

$$A_{\nu_\alpha \to \nu_\beta}(t) = \sum_k U^*_{\alpha k} U_{\beta k} e^{-iE_k t} \tag{2.18}$$

where the fact that $\langle \nu_j | \nu_k \rangle = \delta_{jk}$ has been used since the mass eigenstates are orthonormal. It then follows that the oscillation probability is given by

$$P_{\nu_\alpha \to \nu_\beta}(t) = \sum_{k,j} U^*_{\alpha k} U_{\beta k} U_{\alpha j} U^*_{\beta j} e^{-i(E_k - E_j)t}. \tag{2.19}$$

Under the assumption that neutrinos are relativistic, the mass state energy, E_k, may be expressed in terms of the neutrino energy, E,

$$E_k = \sqrt{|\vec{p}|^2 + m_k^2} \simeq E + \frac{m_k^2}{2E}. \tag{2.20}$$

By noting that the mass splitting, Δm^2_{kj}, is defined as

$$\Delta m^2_{kj} = m_k^2 - m_j^2 \tag{2.21}$$

and that for highly relativistic particles $t \approx L$, where L is known as the baseline (i.e. the distance the neutrino has travelled), the oscillation probability may be written as

$$P_{\nu_\alpha \to \nu_\beta}(L, E) = \sum_{k,j} U^*_{\alpha k} U_{\beta k} U_{\alpha j} U^*_{\beta j} e^{-i\frac{\Delta m^2_{kj} L}{2E}}. \tag{2.22}$$

Finally, in a two flavour oscillation regime, the oscillation probability may be simplified to

$$P_{\nu_\alpha \to \nu_\beta} = \begin{cases} \sin^2(2\theta)\sin^2\left(\frac{\Delta m^2 L}{4E}\right), & \nu_\alpha \neq \nu_\beta \\ 1 - \sin^2(2\theta)\sin^2\left(\frac{\Delta m^2 L}{4E}\right), & \nu_\alpha = \nu_\beta, \end{cases} \tag{2.23}$$

where the mixing matrix has been reduced to a rotation matrix [30].

It should be noted that what neutrino experiments probe is the mass splitting and not the absolute neutrino masses. It is understood from oscillation experiments that Δm^2_{21}, known as the solar mass splitting, is equal to 7.5×10^{-5} eV^2 and that $|\Delta m^2_{31}|$, known as the atmospheric mass splitting, is equal to 2.4×10^{-3} eV^2. The sign of the atmospheric mass splitting is however unknown i.e. it is an open question whether m_3 is the heaviest or the lightest neutrino mass state. This leads to two possibilities, the so called *normal hierarchy* where the neutrino mass states increase from $m_{1\to2\to3}$ or the *inverted hierarchy* where the mass states increase from $m_{3\to1\to2}$. The best fit values for oscillation parameters and the CP violating phase from a 3-flavour neutrino framework are shown in Table 2.1 for both the normal and inverted hierarchy. The numbers have been provided by the 2020 edition of the Particle Data Group (PDG) collaboration [41].

The nature of the neutrino hierarchy has major impacts on several areas. Within the inverted hierarchy, there is a lower bound on the Majorana mass of the electron neutrino mass. If neutrinoless double beta decay experiments can put bounds on the neutrino mass below this, the inverted hierarchy may be ruled out (under the assumption that neutrinos are Majorana in nature). Alternatively, if the inverted hierarchy is realised, neutrinoless double beta decay experiments are promising ways to determine whether neutrinos are Majorana particles or not. There are also a number of theories which predict either the normal or inverted hierarchy, so determining the hierarchy will be a strong motivator in determining the credibility of a given theory [42].

I hate to be annoying but your wrote Δm^2_{13} is Δm^2_{atm} and yet here it Δm^2_{23} it's inconsistent.

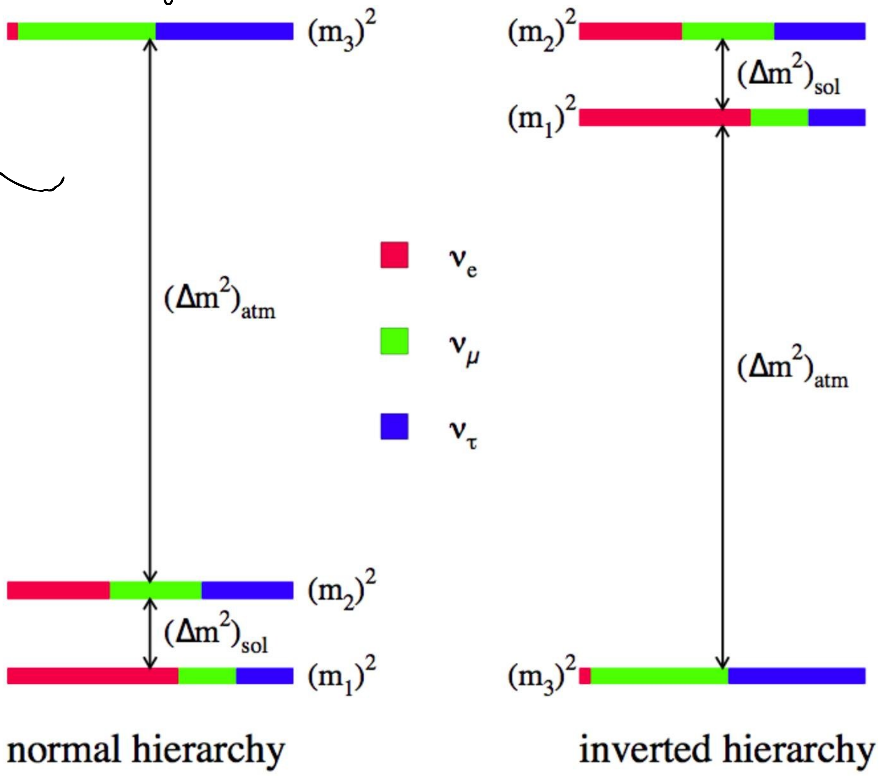

Figure 2.2.: Diagrammatic representation of the normal hierarchy (left) and the inverted hierarchy (right). The flavour contributions to each mass state are illustrated by the different colours [43].

Parameter	Best Fit	
	Normal Hierarchy	Inverted Hierarchy
$sin^2 2\theta_{12}$	0.307 ± 0.013	0.307 ± 0.013
$sin^2 2\theta_{13}$	$(2.20 \pm 0.07) \times 10^{-2}$	$(2.20 \pm 0.07) \times 10^{-2}$
$sin^2 2\theta_{23}$	0.546 ± 0.021	0.539 ± 0.022
Δm^2_{21}	$(7.53 \pm 0.18) \times 10^{-5}$ eV^2	$(7.53 \pm 0.18) \times 10^{-5}$ eV^2
Δm^2_{32}	$(2.453 \pm 0.033) \times 10^{-3}$ eV^2	$(-2.536 \pm 0.034) \times 10^{-3}$ eV^2
δ_{CP}	$1.36^{+0.20}_{-0.16}\pi$ rad	$1.36^{+0.20}_{-0.16}\pi$ rad

Table 2.1.: The best fit values for 3-flavour neutrino oscillation parameters from the 2020 PDG [41].

2.2.4. Matter Effect

The neutrino oscillations discussed so far have assumed that the neutrinos are propagating in a vacuum. It was shown by Wolfenstein that neutrinos propagating in matter experience a potential due to coherent forward scattering with the electrons and nucleons [44]. This potential may be thought of as an effect similar to the index of refraction in a material [30]. Both CC and NC scattering may occur, however, CC scattering may only occur for electron neutrinos whereas NC scattering may occur for all active neutrino flavours equally. The total Hamiltonian for neutrinos propagating in matter, H_T, is therefore the vacuum Hamiltonian as seen in Equation 2.13 plus the Hamiltonian due to the additional potential from matter effects, H_m. That is

$$H_T = H + H_m \qquad \text{with,} \quad \begin{aligned} H|\nu_k\rangle &= E_k|\nu_k\rangle \\ H_m|\nu_k\rangle &= V_m|\nu_k\rangle, \end{aligned} \tag{2.24}$$

where V_m is the effective potential the neutrinos are subjected to [30]. In the three neutrino mass basis,

$$H_T = \frac{1}{2E}\begin{pmatrix} m_1^2 & 0 & 0 \\ 0 & m_2^2 & 0 \\ 0 & 0 & m_3^2 \end{pmatrix} + U^\dagger \begin{pmatrix} V_e & 0 & 0 \\ 0 & 0 & 0 \\ 0 & 0 & 0 \end{pmatrix} U, \tag{2.25}$$

where V_e is the effective potential due to CC scattering. It may be shown that

$$V_e = \pm\sqrt{2}G_F n_e, \tag{2.26}$$

where the positive value is used for neutrinos and the negative value for anti-neutrinos, G_F is the Fermi constant and n_e is the electrons density in the medium. The NC component is omitted since it contributes equally to all neutrino flavours and therefore has no impact on the oscillation probability [31].

If only two neutrino species are considered, the mass splitting in matter, Δm_m^2, is given by

$$\Delta m_m^2 = m_{2m}^2 - m_{1m}^2 = \Delta m^2 \sqrt{(\cos 2\theta - A/\Delta m^2)^2 + \sin^2 2\theta}, \tag{2.27}$$

and the mixing angle in matter, θ_m, is given by

$$\tan 2\theta_m = \frac{\sin 2\theta}{\cos 2\theta - A/\Delta m^2}, \tag{2.28}$$

where Δm^2 and θ are the vacuum mass splitting and vacuum mixing angle respectively and $A \equiv 2EV_e$. The oscillation probability is the same as is shown in Equation 2.23, but substituting in the relevant matter mixing angle and mass splitting instead of the vacuum values. It should be noted that if $\theta = 0$, then $\theta_m = 0$, which means that oscillations in matter can only occur if oscillations in a vacuum are possible. Furthermore, if $A = \Delta m^2 \cos 2\theta$, Equation 2.28 diverges. This critical value of A is knowns as the Mikheyev–Smirnov–Wolfenstein (MSW) resonance and corresponds to $\theta_m = \pi/4$, which means that the oscillation probability is maximal. Therefore, for any non-zero vacuum oscillation probability, there exists a value of A where the matter oscillation probability is a 100% [31].

Another key feature of Equation 2.28 is that the matter mixing angle depends on the sign of Δm^2. This is not the case for vacuum oscillations. Therefore, unlike vacuum oscillations, matter oscillations are one of the possible ways that the neutrino mass hierarchy may be determined [45].

NO! otherwise what is the point of JUNO? even in vacuum you have a term sensitive to the sign of Δm^2

2.3. Experimental Evidence for Sterile Neutrinos

There have been a number of experimental results which are not consistent with oscillations in a three neutrino model. Most of these anomalous results can be explained by oscillations with one or more eV scale neutrinos pointing towards the existence of at least one light sterile neutrino. The experiments which have seen results seemingly in favour of eV scale sterile neutrinos will be discussed in the upcoming sections. There are however tensions between the results in favour of additional neutrino flavours and the null results from experiments such as Karlsruhe Rutherford Medium Energy Neutrino (KARMEN) and Main Injector Neutrino Oscillation Search (MINOS) [46]. The KARMEN experiment was sensitive to $\nu_\mu \to \nu_e$ and $\bar{\nu}_\mu \to \bar{\nu}_e$ over a baseline of 17.6 m. No evidence of oscillations were found and a 90% confidence level exclusion limit was placed on $\Delta m^2 > 100\ eV^2$ with $\sin^2 2\theta < 4 \times 10^{-2}$ and $\sin^2 2\theta < 8.5 \times 10^{-3}$ for neutrinos and anti-neutrinos respectively [47]. The MINOS experiment used a predominantly muon-neutrino beam with a peak energy of 3 GeV with the near detector being at a baseline of 1.04 km. Again, no evidence of oscillations was observed. For a mass splitting of $\Delta m^2_{42} = 0.5$ eV^2, the value of $\sin^2 2\theta_{24}$ was constrained to be less than 0.016 for a 90% confidence level [48].

2.3.1. LSND

The LSND experiment involved a close to 800 MeV proton beam which produced mainly π^+ and was designed to focus on the search for $\bar{\nu}_\mu \to \bar{\nu}_e$ appearance where the $\bar{\nu}_\mu$'s were a result from the decay of anti-muons which in turn were produced from the decay of at rest π^+. The detector consisted of a tank filled with 167 tons of liquid scintillator positioned 30 m from the neutrino beam source and was able to detect both Cerenkov and scintillation light. The $\bar{\nu}_e$ appearance signal was identified from the $\bar{\nu}_e + p \to e^+ + n$ reaction with the signature of the reaction being the energy of the e^+ and the energy of a gamma as a result of neutron capture on a free proton. The LSND experiment observed an excess of $87.96\ \pm 22.46\ \pm 6.0$ events from $\bar{\nu}_e + p \to e^+ + n$ reactions which corresponds to

stat syst ?

a 3.8σ excess which is shown in Figure 2.3 [17]. This was the first experiment to point towards the existence of an eV scale neutrino.

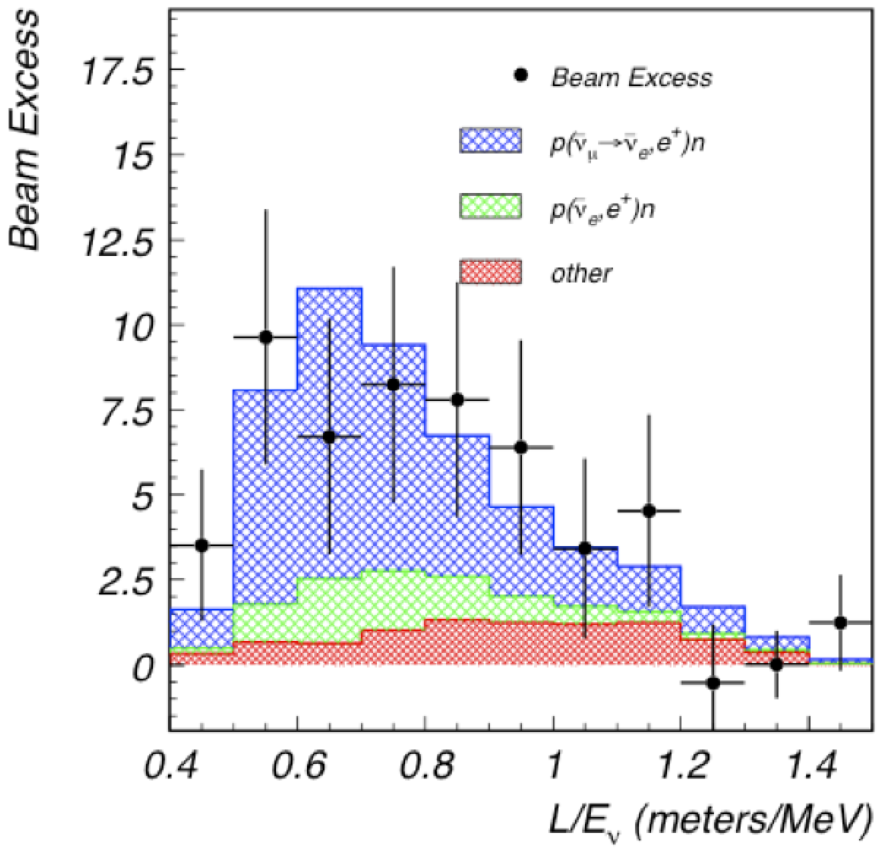

Figure 2.3.: The LSND excess as a function of the neutrino L/E value. Events require a positron in the energy range $20 < E < 60$ MeV and a likelihood ratio of > 10 that the associated gamma was correlated (i.e. $\frac{\mathcal{L}_\gamma(correlated)}{\mathcal{L}_\gamma(accidental)} > 10$) [17].

2.3.2. MiniBooNE

MiniBooNE collected data from the BNB operating in both neutrino and anti-neutrino mode. The BNB is described in detail in Section 3.2. The (anti-)neutrinos had an energy range of $200 < E_\nu < 1250$ MeV and the baseline of the experiment was 541 m. Similar to LSND, MiniBooNE was searching for $\overset{(-)}{\nu}_e$ appearance from a predominantly $\overset{(-)}{\nu}_\mu$ beam. In neutrino mode, MiniBooNE observed an excess of 381.2 ± 85.2 Charged Current Quasi Elastic (CC QE) events which corresponds to a 4.5σ excess. This is shown in Figure 2.4. Combining this with the anti-neutrino data, an excess of 460.5 ± 99.0 CC QE events (4.7σ) were observed. A two neutrino model is assumed so that a comparison with LSND data can be made, however this results in the appearance and disappearance data not being compatible with one another. This may be resolved by assuming a different model to the 3+1 neutrino framework. The results are consistent with those seen by LSND and again point to the existence of additional neutrino flavours beyond the three predicted by the SM [18].

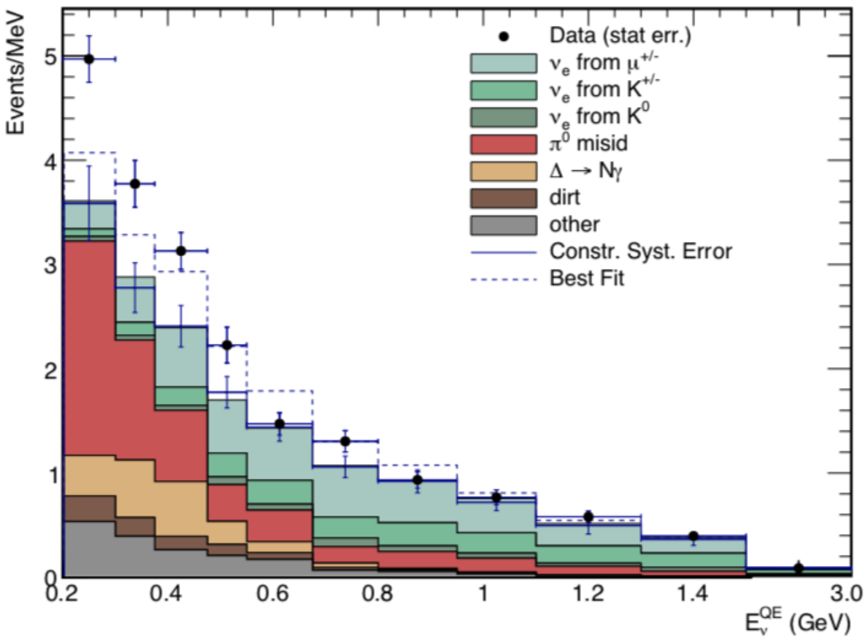

Figure 2.4.: The MiniBooNE excess from ν_e CC QE events. The best fit line assumed two neutrino oscillations [18].

2.3.3. Gallium Anomaly

The *Gallium Anomaly* refers to the apparent deficit of electron neutrinos observed by placing radioactive sources which decay via electron capture in the solar neutrino experiments, SAGE and GALLEX. The GALLEX experiment utilised two separate ^{51}Cr neutrino sources. The key measured quantity was the production of ^{71}Ge due to transformation of ^{71}Ga via inverse beta decay. The strength of the ^{51}Cr neutrino sources was measured directly and via the production of ^{71}Ge. The combined ratio of the strength of the two sources was found to be 0.93 ± 0.08 [19]. A later reanalysis of the results from GALLEX with new technical data gave a ratio of 0.902 ± 0.078 [20]. Similar to the GALLEX experiment, the SAGE experiment also compared the strength of a neutrino source from direct measurements and the production of ^{71}Ge. SAGE used both a ^{51}Cr and a ^{37}Ar source. SAGE observed a ratio 0.95 ± 0.12 for the ^{51}Cr source and a ratio of $0.79^{+0.09}_{-0.10}$ for the ^{37}Ar source. The weighted average from the results from the two sources from SAGE and the reevaluated values from the two GALLEX sources is 0.88 ± 0.05 [21]. This is consistent with a 2.3σ significance and is consistent with $\bar{\nu}_e$ disappearance due to mixing with a sterile neutrinos [49].

2.3.4. Reactor Anomaly

The *Reactor Anomaly* refers to the apparent deficit of anti-electron neutrinos produced from neutron rich fission products such as $^{235}U,^{238}U,^{239}Pu$ and ^{241}Pu undergoing β-decay. For most cases this involves placing a detector within a 100m of a reactor and measuring the ratio of observed to predicted event rates. The average ratio is 0.943 ± 0.023. It is acknowledged that the reactor fluxes may not be perfectly understood which could be the cause for such a deficit, however it should be noted that other experiments have observed similar deficits for comparable L/E ranges [22].

2.4. Theory of Sterile Neutrinos

Assuming that the mass generation of neutrinos follows similar rules to that of other Dirac mass terms, there is motivation to try and attempt to include sterile neutrinos into theoretical models since right handed fields are required. Some of the potential options for neutrino mass generation are discussed in Section 2.4.1. The initial mass scale for sterile neutrinos is unconstrained, however one of the more well motivated models is the "Type 1" *seesaw model* which attempts to explain the relative size of neutrino masses and points towards very heavy sterile neutrino masses ($\gg$ 1 eV). Variations of the Seesaw model have also been proposed that incorporate light sterile neutrinos [10].

2.4.1. Neutrino Mass

The SM Lagrangian, $\mathcal{L}$, for a fermion is given by

$$\mathcal{L} = \overline{\psi}(i\gamma^{\mu}\partial_{\mu} - m)\psi \tag{2.29}$$

with the associated Euler-Lagrange equation being the Dirac equation which is given by [30]

$$(i\gamma^{\mu}\partial_{\mu} - m)\psi = 0. \tag{2.30}$$

Dirac Mass

Within the SM Lagrangian, the Dirac mass term is given by $m_D\overline{\psi}\psi$ where ψ is the Dirac spinor. By dividing this into left and right components it follows that

$$\begin{aligned} m_D\overline{\psi}\psi &= m_D(\overline{\psi_L + \psi_R})(\psi_L + \psi_R) \\ &= m_D(\overline{\psi_L}\psi_R + \overline{\psi_R}\psi_L), \end{aligned} \tag{2.31}$$

where the second step follows from Equation 2.4. Naturally, to have a non-zero Dirac mass term, particles require a left and right handed chiral state. This is the mass generation method that all particles in the SM follow and hence why

No, that's not the reason.
you require the Higgs boson because the left-handed particles in the SM are in doublets, so you cannot simply say $\overline{\nu_L}\,\nu_R$ because ν_L does not exist.

neutrinos are massless in the SM. To give the neutrino mass in this way, a field associated with a right handed neutrino could be introduced. This would usually correspond to the left handed neutrinos being the *active* ones, whilst the right handed neutrinos would be considered *sterile*. In order for the mass terms to actually acquire mass, the SM requires two scalar fields to be introduced. These fields are provided by the Higgs mechanism and allow for spontaneous symmetry breaking [50]. The Dirac mass is given by,

→ instead of allow I would say preserve but I'm not sure what you are trying to say

$$m_{Di} = \frac{y_i v}{\sqrt{2}}, \tag{2.32}$$

where y is the Yukawa coupling and v gives the vacuum expectation value from the Higgs field ($v \simeq 246$ GeV). A concern with generating neutrino masses in this way is the required size of the Yukawa coupling. To generate a mass of say 0.1 eV, the Yukawa coupling would need to be very small (~ 6 orders of magnitude less than that of the electron). This small number is sometimes considered unnatural and provides motivation to search for alternative mass mechanisms to explain the neutrino masses [30].

Majorana Mass

To generate mass without the requirement of a right handed field, it is required that the neutrino be a Majorana particle. It may be shown that

$$P_R C \overline{\psi_L}^T = C \overline{\psi_L}^T, \tag{2.33}$$

which means that $C\overline{\psi_L}^T$ is a right handed object, where the superscript T indicates the transpose and $C = i\gamma^2\gamma^0$ which is the charge conjugation operator. By defining $\psi_L^C = C\overline{\psi_L}^T$, the Majorana field mass term in the Lagrangian can be written as

$$\frac{m_L}{2}(\overline{\psi_L^C}\psi_L + \overline{\psi_L}\psi_L^C), \tag{2.34}$$

where the factor of 1/2 arises due to double counting. As is the case for the Dirac mass, the SM requires the introduction of additional fields to allow for spontaneous symmetry breaking [30].

Seesaw mechanism

If both Dirac and Majorana mass terms are present, the mass component of the Lagrangian, $\mathcal{L}_{mass}$, may be written as a matrix equation. For one active and one sterile neutrino, this has the form

$$\mathcal{L}_{mass} = \frac{1}{2}\begin{pmatrix}\overline{\psi_L^C} & \overline{\psi_R}\end{pmatrix}\begin{pmatrix}m_L & m_D \\ m_D & m_R\end{pmatrix}\begin{pmatrix}\psi_L \\ \psi_R^C\end{pmatrix} + h.c. \tag{2.35}$$

where the central 4×4 matrix is known as the mass matrix, $\mathcal{M}$ [10]. By diagonalising $\mathcal{M}$ into mass eigenstates, m_1, m_2, and assuming $m_L = 0$ (since it is not allowed in the SM) and that $m_R \gg m_D$, the mass eigenvalues may be expressed as

$$\begin{aligned} m_1 &\simeq \frac{m_D^2}{m_R} \\ m_2 &\simeq m_R. \end{aligned} \tag{2.36}$$

Since $m_R \gg m_D$, m_2 is also large and m_1 is small since the value of m_D^2 is suppressed by the large value of m_R in the denominator. Furthermore, the larger the value of m_2, the smaller the value of m_1. This linked relationship gives rise to the so-called Type I [1] *seesaw mechanism*. m_1 would give the mass scale of the active neutrinos whereas m_2 would be a heavy sterile neutrino. This mechanism requires neutrinos to be Majorana particles, but can be extended to include three active neutrinos and an arbitrary number of sterile neutrinos and does provide an explanation on the relative smallness of the neutrino masses compared with other SM particles [30].

[1] A number of other seesaw mechanisms exist which typically involve the exchange of a particle such as a heavy Majorana neutrino as is the case in the Type I mechanism [10].

2.4.2. Sterile Neutrino Oscillations

An overview of the physics describing neutrino oscillations within the active sector was presented in Section 2.2.3. This approach may be extended to included an arbitrary number of additional neutrino states by expanding the PMNS matrix to include the desired number of sterile neutrinos

$$U_{sterile} = \begin{pmatrix} U_{e1} & U_{e2} & U_{e3} & U_{e4} & \dots \\ U_{\mu 1} & U_{\mu 2} & U_{\mu 3} & U_{\mu 4} & \dots \\ U_{\tau 1} & U_{\tau 2} & U_{\tau 3} & U_{\tau 4} & \dots \\ U_{s1} & U_{s2} & U_{s3} & U_{s4} & \dots \\ \vdots & \vdots & \vdots & \vdots & \ddots \end{pmatrix}. \tag{2.37}$$

For simplicity, often only the case with one sterile neutrino is considered. This is known as the $(3+1)$ neutrino framework which takes into account the three usual active neutrinos with the addition of one sterile neutrino. Within a $(3+1)$ framework and assuming that $\Delta m^2_{41} \gg |\Delta m^2_{31}|, \Delta m^2_{21}$, short baseline oscillation are well represented by the two flavour oscillation probability,

$$P_{\nu_\alpha \to \nu_\beta} = \delta_{\alpha\beta} - 4|U_{\alpha\beta}|^2(\delta_{\alpha\beta} - |U_{\alpha\beta}|^2)\sin^2\left(\frac{\Delta m^2_{41} L}{4E}\right), \tag{2.38}$$

where $\delta_{\alpha\beta}$ is the Kronecker delta between states α and β, $U_{\alpha\beta}$ are the relevant entries from the PMNS matrix and Δm^2_{41} is the mass splitting involving the sterile neutrino state [13].

When performing a search for sterile neutrinos, typically there are three channels, one or more of which may be probed (plus their corresponding anti-neutrino variants). For each of these channels, the relevant PMNS matrix elements are parameterised in terms of mixing angles such that,

$$\nu_\mu \text{ disappearance } (\nu_\mu \to \nu_\mu) \quad : \sin^2 2\theta_{\mu\mu} \equiv 4|U_{\mu 4}|^2(1 - |U_{\mu 4}|^2) \tag{2.39}$$

$$\nu_e \text{ appearance } (\nu_\mu \to \nu_e) \quad : \sin^2 2\theta_{\mu e} \equiv 4|U_{\mu 4}|^2|U_{e4}|^2 \tag{2.40}$$

$$\nu_e \text{ disappearance } (\nu_e \to \nu_e) \quad : \sin^2 2\theta_{ee} \equiv 4|U_{e4}|^2(1 - |U_{e4}|^2). \tag{2.41}$$

It should be noted that ν_e appearance depends on $U_{\mu 4}$ and U_{e4}, which ν_μ and ν_e disappearance depend on respectively. The observation of ν_e appearance would therefore automatically imply that ν_μ and ν_e disappearance is also present. Additionally, this allows these parameters to be over constrained [13]. The current global best fit values for the three mixing angles and the mass splitting term, Δm^2_{41} are outlined in Table 2.4.2.

Oscillation Parameter	Best Fit Value
$\sin^2 2\theta_{\mu\mu}$	0.07157
$\sin^2 2\theta_{\mu e}$	0.0009809
$\sin^2 2\theta_{ee}$	0.05310
Δm^2_{41}	1.32 eV^2

Table 2.2.: The global best fit values for the (3 + 1) sterile neutrino oscillation parameters [46].

Chapter 3.

The Short Baseline Neutrino Program

The SBN program is comprised of three distinct LArTPC type detectors located at Fermilab. The three detectors are SBND, MicroBooNE and ICARUS and all three lie along the axis of the BNB. In order to minimise systematic uncertainties, the three detectors share many of the same technologies. The general operating principles of a LArTPC are described in Section 3.1 and the specific details of each detector are discussed in Section 3.4 (SBND), Section 3.5 (MicroBooNE) and Section 3.6 (ICARUS). The BNB consists predominantly of muon neutrinos with energies of the order 1 GeV and is discussed in detail in Section 3.2. The three detectors are positioned at 110m, 470m and 600m from the neutrino beam source respectively [13].

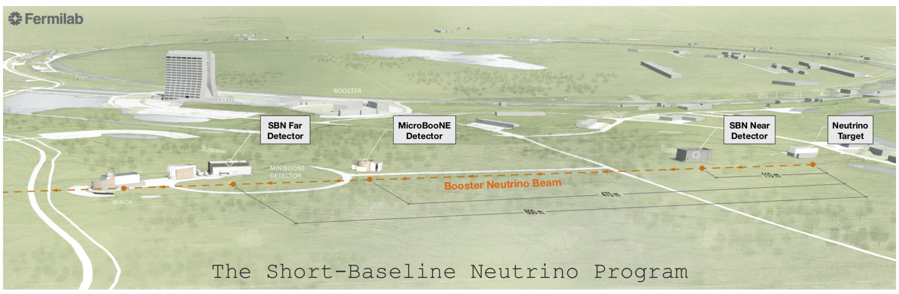

Figure 3.1.: A view of the Fermilab complex highlighting the position of the SBN detectors [13].

One of the primary aims of the SBN program is to provide a definitive test to either confirm or refute the existence of light sterile neutrinos which have been hinted at by a number of experiments discussed in Section 2.3. Other major aims of the SBN program include investigating neutrino argon cross-sections and developing large scale LArTPC technologies. The close proximity of SBND to the BNB source means that SBND will observe neutrino argon interactions with high statistics allowing statistical uncertainties to be minimised and will allow for the exploration of rare channels such as neutrino-electron scattering. Both the development of LArTPC technology and an improved understanding of neutrino interaction cross-sections will be invaluable for future neutrino experiments such as DUNE [13].

3.1. Liquid Argon Time Projection Chambers

The idea of a LArTPC was first proposed in 1977 by Rubbia in an attempt to consolidate the high resolution but low number of interactions obtained from 'bubble chamber' style detectors and the high rate but low resolution interactions obtained from 'counter' experiments. This would be achieved by propagating the complete image of an event through a noble element and then electronically reconstructing the 3D event by combining the 2D information collected and the drift time [51].

Liquid argon was identified as the most suitable medium to use for such a detector due to the following properties [51];

- High density (1.4 gcm^{-3}) with a sufficiently high atomic mass to allow for a reasonable probability of neutrino interactions.
- Argon is a noble element, meaning the electrons will not combine with the argon resulting in long drift times, assuming a good enough purity is obtained
- Argon is a noble element, meaning that any energy absorbed by the argon atom can only be used to ionise the atom or is again released in the form of scintillation light. The energy cannot be consumed by actions such as vibrations or rotations.

- A high electron mobility, meaning the electrons may drift quickly across the detector.
- Argon is relatively cheap and easy to purify.
- Argon may be liquefied easily using liquid nitrogen.

3.1.1. LArTPC Operating Principles

The general design of a single chamber LArTPC is shown in Figure 3.2. Most LAr detectors consist of one or more TPCs with a cathode and anode plane at either end inducing an electric field across the TPC. The resulting particles from a neutrino interaction will ionise argon atoms as they traverse through the TPC. The electric field causes the ionisation electrons to drift towards the anode where they will induce a current on a series of wire planes. The most rear wire plane (the one furthest away from the cathode) is known as the collection plane and the one or more wire planes in front of the collection plane are known as induction plane(s). There is a further potential difference between the induction and collection planes which ensures that the electrons will also reach the collection plane. The wire planes are orientated so that the wire angles between the planes are different which allows for 2D position reconstruction. A series of PMTs surround the detector which collect scintillation light. The scintillation light has two components, *fast* and *slow*, which are due to two distinct scintillation mechanisms. The time period to detect the fast component is $\sim$6 ns, whereas for the slow component it is $\sim$1.6 μs [11]. The electron drift velocity in a 500 V/cm field is $\sim$1.6 mm/μs [52]. Since the scintillation light is detected almost instantaneously when compared to the the time taken for the electrons to drift to the wire planes, the horizontal drift distance may be determined. Combining this with the 2D information from the wire planes allows for 3D event reconstruction. The induced current on the wire planes is interpreted in terms of signal waveforms. If the waveforms are above some threshold value such that they can be distinguished from noise, *hits* are constructed which encapsulate the signal. Each hit contains information such as the associated wire plane, wire number and charge and it is this information which is used to obtain reconstructed information about an event [53]. The specific designs of the three LArTPCs used in the SBN program are discussed in Section 3.4 (SBND), Section 3.5 (MicroBooNE) and Section 3.6 (ICARUS).

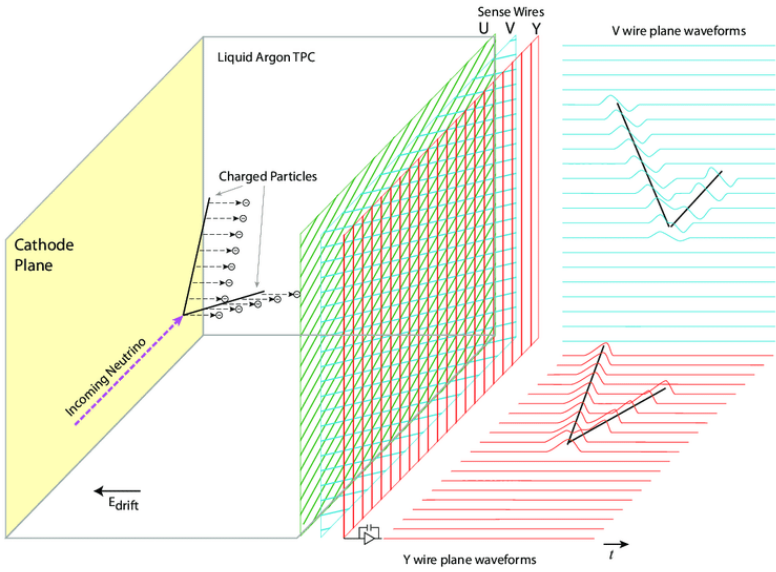

Figure 3.2.: A schematic of the operating principle of a LArTPC detector. A neutrino interacts in the argon producing secondary particles which ionise the argon atoms as they travel across the TPC. The electric field causes the ionisation electrons to drift towards the wire planes where their energy deposits are recorded. [53]

Along with the global volume of a detector which is defined by its dimensions, there are usually two other volumes associated with LArTPCs: the *active* volume and the *fiducial* volume. The active volume is defined as the volume which is enclosed within the TPC and is the volume of the detector which allows for event detection. The fiducial volume is not directly defined by the physical design of the detector, but is instead the region within the active volume where event reconstruction is thought to be well understood. Events occurring right at the edge of the TPC may be difficult to reconstruct and are therefore poorly understood. Additionally, background events tend to occur close to the edge of the TPC, so by only considering events within the fiducial volume, the percentage of well understood signal events is maximised [31]. The active and fiducial volumes used in each of the SBN detectors is defined in Appendix B.

3.1.2. Detector effects

Despite the many desirable properties of liquid argon, there are still a number of effects which have to be considered when performing event reconstruction.

Diffusion

Diffusion is the process in which the drifting electrons do not drift in such a way that they will continue to perfectly represent the initial image of an event. That is to say that the electrons will disperse as they drift in the detector. This happens in both the transverse and longitudinal directions with respect to the direction of the electric field and impacts the spatial resolution of the detector [54].

For the case of a zero electric field and with the electrons in thermal equilibrium, the diffusion is isotropic and the diffusion coefficient, D, is given by the Einstein relation such that

$$D = \frac{kT}{e}\mu_0, \tag{3.1}$$

where k is Boltzmann's constant, T is the temperature, e is the elementary charge and μ_0 is the electron mobility (for the case of no electric field) [54].

In the presence of an electric field, the electron mobility is no longer given by μ_0, but instead by μ and the electrons are no longer in thermal equilibrium. The diffusion also becomes anisotropic, leading to distinct diffusion coefficients for the longitudinal and transverse directions, D_L and D_T respectively which are given by

$$\begin{aligned} D_L &= \frac{kT}{e}(\mu + E\frac{\partial \mu}{\partial E}) \\ D_T &= \frac{kT}{e}\mu. \end{aligned} \tag{3.2}$$

In general, the diffusion in the transverse direction is greater than the diffusion in the longitudinal direction [54] [55].

Electron Lifetime

Electron lifetime is a measure of the free electrons lost due to attachment to impurities in the liquid argon whilst drifting across the detector [56]. It is also the quantity that drives the width to which a TPC is constructed. Naturally, the electron lifetime, τ_e, is coupled to the purity of the argon such that

$$\tau_e \propto 1/k_e, \tag{3.3}$$

where k_e is the impurity concentration. The rate of charge loss is then given by

$$Q = Q_0 e^{-t/\tau_e}, \tag{3.4}$$

where Q is the charge remaining after correcting for electron lifetime, Q_0 is the initial charge and t is the drift time [56]. The lowest electron lifetime (during a period where the purity was considered stable) that MicroBooNE has observed is 18.0 ms [57]. Currently, the SBND simulation uses a default value of 10.0 ms for the electron lifetime, whereas the ICARUS simulation uses a value of 15.0 ms. By requiring that the maximum charge loss is only of the order 10%, this results in a maximum drift distance (TPC width) of $\sim$1.5 m.

Recombination

When argon atoms are ionised, the resulting ionised electron may immediately recombine with a nearby argon ion instead of being separated by the electric field in the detector. This is known as the recombination effect and the magnitude of the effect is largely determined by the local electric field. A number of different approaches to model the recombination effect exist, however, for liquid argon detectors, a form of the box model or Jaffé model are usually used [54].

The Jaffé model is based on the idea that recombination depends on the charge density of both nearby electrons and ions. The model assumes a cylinder surrounding the ionisation track and recombination may occur between any of the ionised electrons and ions, not just the electron with its associated parent ion which is were the Jaffé model largely differs from earlier models [58]. The recombination effect from the Jaffé model is given by

$$Q = \frac{Q_0}{1 + q_0 F(E \sin\phi)}, \tag{3.5}$$

where Q_0 is the initial charge, Q is the charge after recombination, q_0 is the initial density of electron-ion pairs and F is a function depending on the electric field E, the angle between the field and the ionisation track, ϕ and other quantities which describe the diffusion. Equation 3.5 is commonly approximated by Birks' law with a normalisation parameter to help fit the model to the experimental data [54].

In their development of the box model, Thomas and Imel assumed the diffusion and ion mobility to be zero and instead of the cylindrical column used in the Jaffé model, they considered a box with a uniform charge distribution such that,

$$Q = Q_0 \frac{1}{\xi} \ln(1 + \xi), \tag{3.6}$$

where $\xi = \alpha Q_0 / E$. α is a free parameter and Q and Q_0 are defined as in Equation 3.5 [54] [59].

In addition to being model dependant, the exact recombination value is often presented as a function of dE/dx. For an electric field of 0.5 kV/cm, the recombination value has a maximum of $\sim$0.7 at a dE/dx value of $\sim$1 MeV/cm and falls to a minimum of $\sim$0.1 as the dE/dx value increases to $\sim$30 MeV/cm [54].

Space Charge

The electric field in a TPC is usually designed to be uniform between the cathode and the anode, however, particularly for surface level detectors this often does not end up being the case. Cosmic muons may enter the detector ionising the argon atoms. The ionised electrons and argon ions then drift towards the anode and cathode respectively, however, the drift time for the ions is much greater than the electron drift time. If the flux of cosmic muons entering the detector is sufficiently large, this results in a significant positive charge build up towards the cathode. This effect is known as *space charge* and directly impacts the recombination effect since it is linked to the magnitude of local electric field as well as affecting the drifting electrons [60].

The ion drift velocity, $\vec{v}$, is given by

$$\vec{v} = \mu \vec{E}, \tag{3.7}$$

where μ is the ion mobility and $\vec{E}$ is the electric field. The build up of charge density, ρ, is given by the continuity equation,

$$\vec{\nabla} \cdot \vec{J} + \frac{\partial \rho}{\partial t} = K, \tag{3.8}$$

where $\vec{J} = \rho \vec{v}$ and K is the volume rate at which ion pairs are created ($[K]$ = ion pairs/volume/second) [61].

With the simplified assumption that the build up of charge is constant (time-independent) and that the drift direction is only in the x-direction which is the same as the electric field, Equation 3.8 may be reduced to

$$\frac{d\rho v}{dx} = K. \tag{3.9}$$

Gauss's law states that,

$$\nabla \cdot \vec{E} = \frac{\rho}{\epsilon}, \tag{3.10}$$

where ϵ is the dielectric constant of the medium. By combining Equation 3.9 and Equation 3.10 it follows that

$$\frac{dE}{dx} = \frac{Kx}{\mu E \epsilon}. \tag{3.11}$$

By defining the coordinates of the system such that the anode is at $x = 0$ and $0 \leq x \leq D$ where D is the position of the cathode, Equation 3.11 may be integrated via,

$$\int_{E_A}^{E} E' dE' = \int_0^x \frac{Kx'}{\mu\epsilon} dx', \tag{3.12}$$

where E_A is the electric field at the anode and both E' and x' are dummy variables. This gives an x dependent electric field solution,

$$E(x) = \sqrt{E_A^2 + \frac{Kx^2}{\mu\epsilon}} = E_0\sqrt{\left(\frac{E_A}{E_0}\right)^2 + \alpha^2 \frac{x^2}{D^2}}, \tag{3.13}$$

where $E_0 = V/D$ is the nominal electric field, V is the difference in the voltage between the anode and cathode and $\alpha = \frac{D}{E_0}\sqrt{\frac{K}{\epsilon\mu}}$ which is a dimensionless parameter [61].

3.2. Booster Neutrino Beam

The BNB is produced by firing 8 GeV protons onto a beryllium target resulting in a secondary beam of hadrons [62]. A toroidal focusing horn surrounds the target and focuses or defocuses charged particles depending on the sign of their charge. The focused hadrons then travel down a 50 m tunnel where most of them will decay producing muon neutrinos and small fraction of electron neutrinos. At the end of the 50 m decay region is a concrete and steel absorber designed to absorb any non-neutrino particles [63]. A schematic of the BNB layout is shown in Figure 3.3. The decay modes of the hadrons resulting in a neutrino and the corresponding branching ratios are listed in Table 3.1.

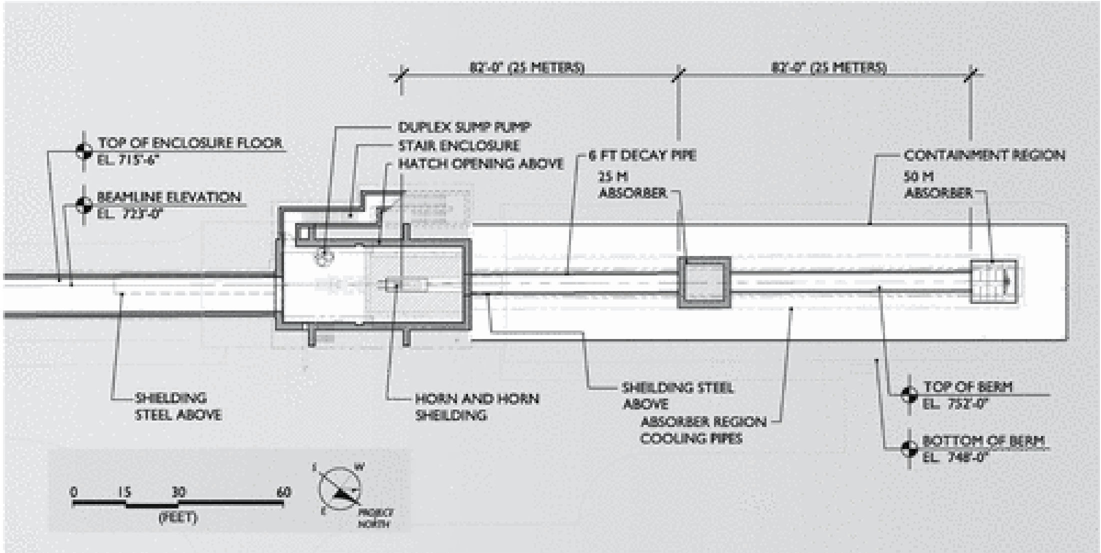

Figure 3.3.: A schematic of the layout of the BNB [64].

Particle	Decay Mode	Branching Ratio (%)
π^+	$\mu^+ + \nu_\mu$	99.9877
	$e^+ + \nu_e$	0.0123
K^+	$\mu^+ + \nu_\mu$	63.44
	$\pi^0 + e^+ + \nu_e$	4.98
	$\pi^0 + \mu^+ \nu_\mu$	3.32
K^0	$\pi^- + e^+ + \nu_e$	20.333
	$\pi^+ + e^- + \bar{\nu}_e$	20.197
	$\pi^- + \mu^+ + \nu_\mu$	13.551
	$\pi^+ + \mu^- + \bar{\nu}_\mu$	13.469
μ^+	$e^+ + \nu_e + \bar{\nu}_\mu$	100

Table 3.1.: The decay modes of the hadrons produced by the BNB when running in neutrino mode. The branching ratio of each of the decay modes is also given [64].

A current of 174 kA is supplied to the magnetic horn in 143 μs pulses which corresponds to the frequency of the incident protons. The direction of the current may be reversed allowing for the focusing of positively or negatively charged particles. Since the charge of the decaying hadrons is linked to the type of neutrino produced, the ability to focus both positively and negatively charged particles allows the BNB to run in neutrino or anti-neutrino mode [64]. Pions are the primary particle produced from the incident protons hence the BNB is muon (anti-)neutrino dominated. The percentage neutrino flavour composition of the BNB is given in Table 3.2 for both neutrino and anti-neutrino mode.

Neutrino Flavour	% in Neutrino Mode	% in Anti-neutrino Mode
ν_μ	93.6	15.71
$\bar{\nu}_\mu$	5.86	83.73
ν_e	0.52	0.2
$\bar{\nu}_e$	0.05	0.4

Table 3.2.: The neutrino flavour composition of the BNB when it is running in either neutrino or anti-neutrino mode [64].

The neutrino flux of the BNB was simulated by the MiniBooNE collaboration for both neutrino and anti-neutrino mode [64]. The flux of the electron and muon (anti-)neutrinos in each of the three SBN detectors is shown in Figure 3.4. The

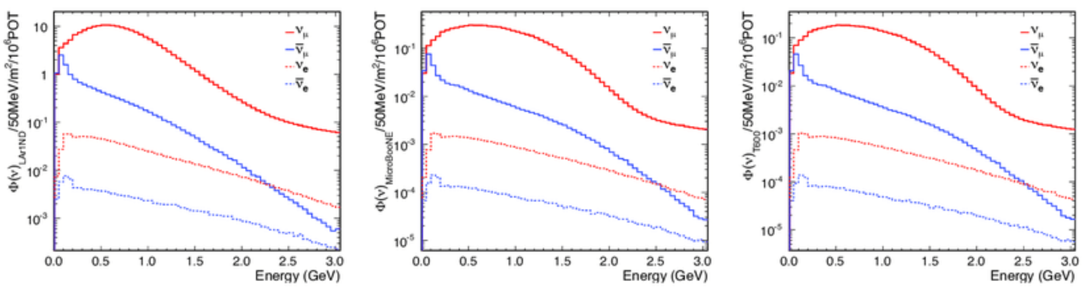

Figure 3.4.: The predicted flux of the BNB at SBND (left), MicroBooNE (middle) and ICARUS (right) for both electron and muon neutrinos and anti-neutrinos [11].

systematic uncertainties associated with the BNB account for an error of $\sim$9% at the peak of the ν_μ flux with a larger error for energies either side of the peak. The systematic uncertainties are mainly due to determining the rate and spectrum of neutrinos for each proton on target, determining the rate and spectrum of secondary particles produced from protons interacting with the beryllium target, the rate of hadronic interactions, the focusing properties of the magnetic horn and the beamline geometry [64].

3.3. Neutrino Interactions

The following section outlines some of the most common CC and NC interaction processes in SBN. The associated CC and NC Feynman diagrams for these processes are shown in Figure 3.6 and Figure 3.7 respectively (the possible 2 Particles 2 Holes (2p2h) interactions are shown separately in Figure 3.5). Only examples of neutrino interactions are shown, however, these may be easily adapted to the anti-neutrino case. Additionally, interaction flavours are kept general with l representing the lepton flavour. In principle $l \in \{e, \mu, \tau\}$, however, within SBN only the electron and muon flavours are relevant.

Elastic and Quasi-Elastic

When particles interact via elastic scattering, the initial particles do not change. Since neutrinos are neutral particles that weakly interact, NC elastic scattering being mediated by the Z^0 boson may occur with a neutrino scattering off a proton via

$$\nu_l + p \rightarrow \nu_l + p. \tag{3.14}$$

Quasi-elastic scattering is similar to elastic scattering, however, charge is exchanged and therefore the interaction is mediated by the W^+ boson. CC QE interactions are defined by the production of a charged lepton plus a (semi-) stable baryon. The dominant form of these interactions occur when the incoming neutrino scatters off a neutron and is converted to its charged lepton counterpart whilst the neutron changes to a proton via

$$\nu_l + n \rightarrow l^- + p. \tag{3.15}$$

CC QE interactions are the most abundant in the GeV range, which is the energy range of the BNB [65].

Resonant

At higher energies, the neutrino-nucleon interaction may cause the nucleon to be excited into a baryon resonance. The resonance will then decay back into a nucleon plus a pion. Using the Delta resonance (Delta baryon) as an example, CC interaction occur via

$$\nu_l + N \rightarrow l^- + \Delta \rightarrow l^- + N + \pi, \tag{3.16}$$

whereas NC interactions occur via,

$$\nu_l + N \rightarrow \nu_l + \Delta \rightarrow \nu_l + N + \pi. \tag{3.17}$$

In both cases, N represents some nucleon with Δ and π being one of the possible Delta resonances and pions appropriate for a given interaction [65] [66].

2 Particles 2 Holes

Within the nuclear environment, there is a correlation between the distribution of nucleons. Therefore, some of the nucleons are bounded in pairs and these bound nucleon pairs may be thought of as being bound due to the exchange of virtual mesons.[1] In this type of interaction, multiple nucleons are excited in a quasi-elastic fashion. The boson may couple to either a nucleon or the meson that is being exchanged. This leads to a number of possibilities such as; 1) the boson couples to the exchanged meson (pion-in-flight diagram), 2) the boson couples at the vertex between the nucleon and exchanged meson (seagull diagram), 3) the meson exchange occurs with a virtual intermediate nucleon to which the boson couples, 4) as in case 3), but the intermediate particle is a Delta resonance instead of a nucleon. Feynman diagrams of these 4 possibilities are shown in Figure 3.5 [65] [67] [68].

[1] This exchange of mesons is sometimes also known as a Meson Exchange Current (MEC). MECs are a subset of 2p2h interaction where the W boson couples directly to the exchanged meson, however, these terms are sometimes used interchangeably.

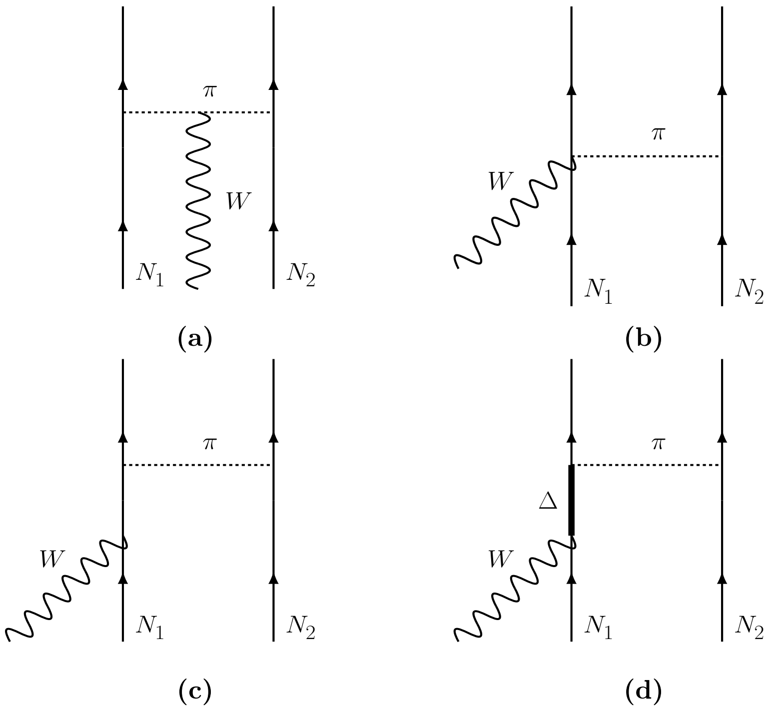

Figure 3.5.: Feynman diagrams of possible 2p2h interactions. The boson may couple to (a) the pion-in-flight, (b) the 2p2h vertex (seagull diagram), (c) an intermediate nucleon, (d) an intermediate Delta resonance [65].

Deep Inelastic Scattering

At even higher energies than those for resonant interactions ($> \mathcal{O}(5 \text{ GeV})$), Deep Inelastic Scattering (DIS) interactions become dominant. In DIS interactions, the neutrino scatters off individual quarks rather than the nucleon as a whole. This results in the break-up of the nucleon, but since the strong force prevents single quarks from existing, a hadronic shower X is produced [30] [65]. A CC DIS interaction occurs via

$$\nu_l + N \rightarrow l^- + X, \tag{3.18}$$

whereas the NC interaction occurs via

$$\nu_l + N \rightarrow \nu_l + X. \tag{3.19}$$

Coherent Production

Coherent interactions occur when the neutrino scatters off the whole nucleus with a negligible momentum transfer. This results in final state particles such as pions, rho mesons or photons being produced, but leaves the target nucleus unaltered. Coherent scattering may occur for both CC and NC interactions (with pions in the final state being used as an example) via

$$\nu_l + A \rightarrow l^- + A + \pi^+ \tag{3.20}$$

and

$$\nu_l + A \rightarrow \nu_l + A + \pi^0 \tag{3.21}$$

respectively [66] [67].

Neutrino Electron Scattering

Instead of scattering off the nucleus, neutrinos may also scatter off the electrons in an atom via,

$$\nu_l + e^- \to \nu_l + e^-. \tag{3.22}$$

This is an elastic process that has both a CC and NC component, however, for typical neutrino energies only ν_e CC interaction are kinematically allowed [30].

Not really.

if it's ν_e you cannot distinguish between NC and CC

also what are the components in this case?

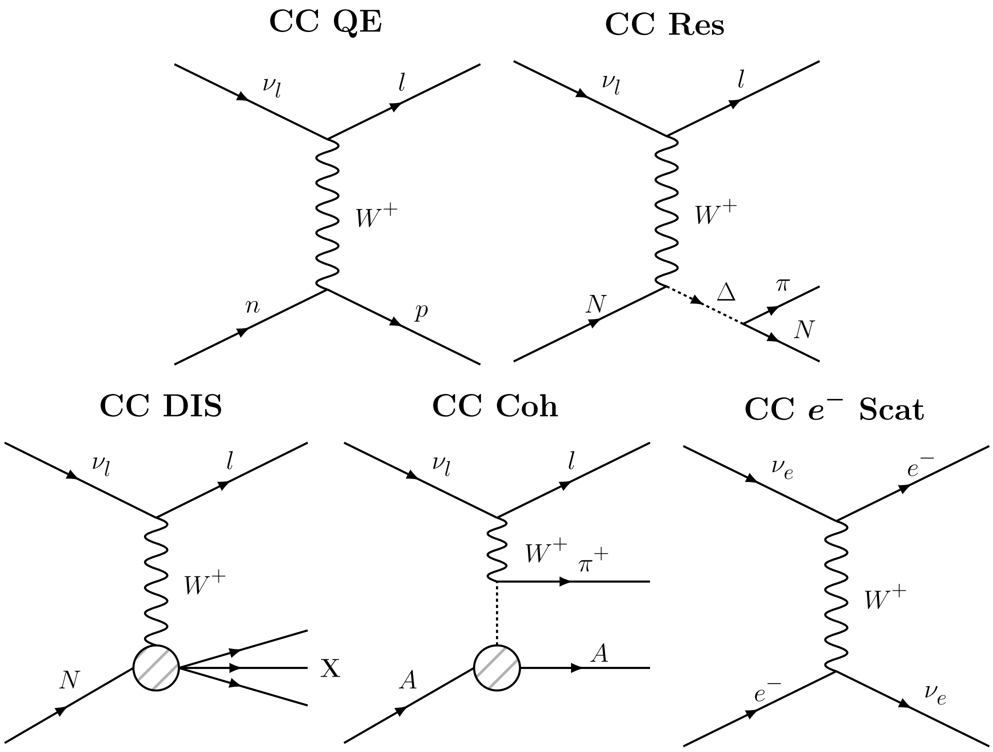

Figure 3.6.: Feynman diagrams of the CC processes most commonly expected in SBN. ν_l corresponds to the neutrino with leptonic flavour l, with l typically being either an electron or a muon. Δ denotes one of the possible Delta resonances, N denotes a nucleon, X denotes some set of final hadrons and A denotes a nucleus.

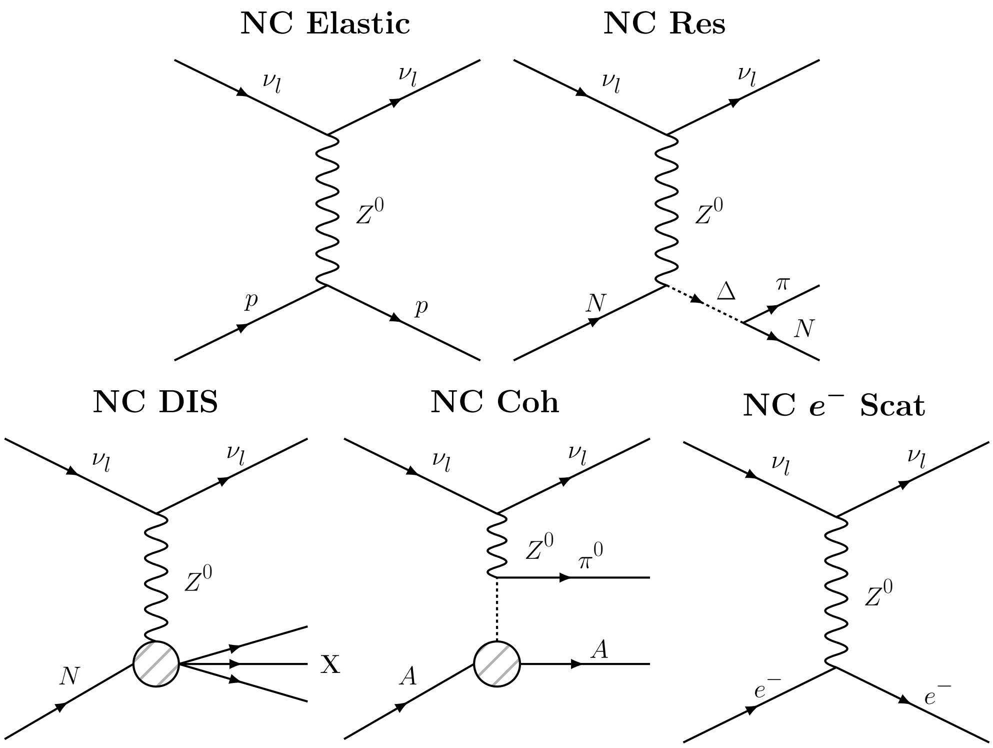

Figure 3.7.: Feynman diagrams of the NC processes most commonly expected in SBN. ν_l corresponds to the neutrino with leptonic flavour l, with l typically being either an electron or a muon. Δ denotes one of the possible Delta resonances, N denotes a nucleon, X denotes some set of final hadrons and A denotes a nucleus.

3.4. SBND

Not clear that there are 2 active volumes. Add a specification

SBND was purposely designed to be the near detector of the SBN program and has an active volume with dimensions (4, 4, 5) m containing 112 tons of liquid argon. It consists of two TPCs, where the central shared cathode sits in the middle of the detector with an anode either side as is shown in Figure 3.8. Each of the Andode Plane Assemblys (APAs) consist of three wire planes where the first and second induction plane are orientated at $\pm 60^{\circ}$ to the vertical and the collection plane is vertical. In all cases, the wire plane spacing and the wire pitch are 3 mm. The nominal electric field in each of the TPCs is 500 V/m [11].

In the Miniboone case you specify that its z-axis is aligned with the beam direction. here you don't say anything. try to give the same information for the 3 detectors.

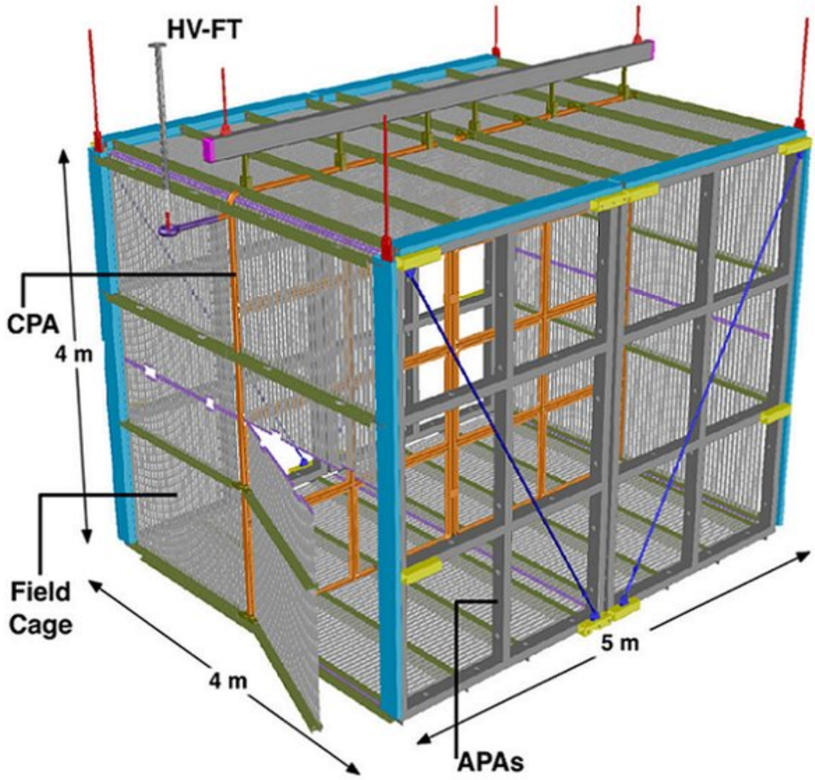

Figure 3.8.: Schematic showing the dimensions of the SBND detector. The Cathode Plane Assembly (CPA), APAs (only one is labelled) and field cage are shown. The Photon Detection System (PDS) is not shown, but the 12 squares on the near APA represent the location where the PDS boxes will be positioned. [69]

Cosmic Ray Tagger

SBND is considered to be a surface level detector with no overburden. Consequently, the cosmic ray flux will be significant with an average of 3 cosmic rays seen in each neutrino event [11]. This will be the most abundant background in SBND and therefore it will be crucial to be able to identify the cosmic ray muons. In order to do this, SBND will use a Cosmic Ray Tagger (CRT) system which consists of a total of 7 panels, one for each side of the detector plus an additional one for the top face as this is where most of the cosmic rays will be entering the detector from. Figure 3.9 shows how the CRT panels will be positioned. Each CRT plane consists of two layers, where one layer is comprised of 2×5 X-oriented modules and the other layer is comprised of 2×4 Y-oriented modules. Each of these modules is comprised of 16 scintillator strips. Two fibres are attached to each strip which are in turn attached to Silicon Photomultipliers (SiPMs). The orthogonal two layer setup coupled with the SiPM readout allows the location of an interaction in the CRT to be determined [70]. The CRT system monitors the crossing time and coordinates of the particles and compares them with the information from the light detection system and the beam time rejecting the events that are identified as cosmic muons. [71].

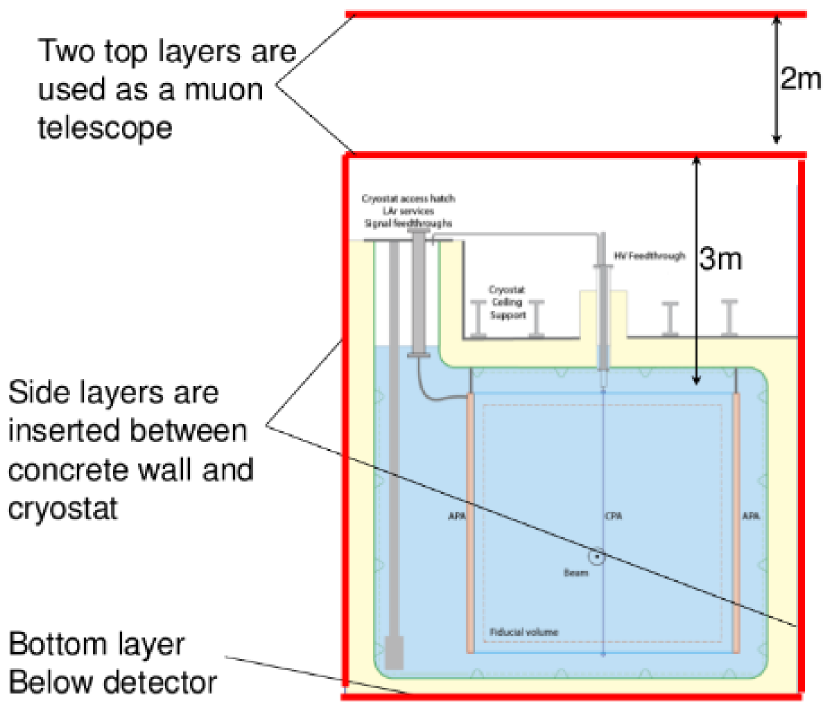

Figure 3.9.: Diagram showing how the CRT will surround SBND on all sides with an additional panel above the top surface [11].

Photon Detection System

The PDS consists of a total of 24 *boxes*, 12 of which will be mounted behind each APA. Each box houses 5 PMTs and 8 Argon R&D Advanced Program at UniCAmps (ARAPUCAs) (specifically, X-ARAPUCA's are used which are an advancement over the initial ARAPUCA design) as shown in Figure 3.11. The

4 outer PMTs of each box are coated with Tetraphenyl Butadiene (TPB) whilst the central one remains uncoated. The scintillation light produced by argon has wavelengths in the Vacuum Ultra Violet (VUV) region, however, the PMTs are only able to detect visible light. The TPB coating shifts the wavelength of the VUV light into the visible region allowing it to be detected. Therefore, the coated PMTs are sensitive to both visible and VUV light whilst the uncoated PMTs are only sensitive to visible light [69].

ARAPUCAs are a novel light trap which consist of a box where the internal surfaces are highly reflective. The surface of the ARAPUCA which faces the incoming light consists of dichroic filter with a wavelength shifter either side of the filter. The wavelength of the light which is incident on the outermost shifter is shifted such that it may pass through the dichroic filter and after passing through the filter the light is again wavelength shifted so that it may no longer pass through the filter and thus remains trapped in the ARAPUCA. A schematic of the ARAPUCA design is shown on the left of Figure 3.10. The inside of the ARAPUCA module contains a SiPM photo-sensor in order to detect the light. Due to the highly reflective nature of the inside of the ARAPUCA, only a small region needs to be exposed to a photo-sensor in order to detect the trapped photons [72]. The X-ARAPUCA improves on the initial design by replacing the inner wavelength shifter with an acrylic slab with the wavelength shifter implanted in the slab and the photo-sensor being directly attached to the slab. Light entering the X-ARAPUCA may be detected in same way as was done in the original ARAPUCA (Figure 3.10: Left), however the photons may also become trapped in the slab by total internal reflection and travel within the slab to the photo-sensor (Figure 3.10: Middle) or if the light enters at a large angle, the photons may become trapped between the surface of the slab and the filter and will travel to the photo-sensor without ever entering the slab (Figure 3.10: Right). The middle scenario of Figure 3.10 represents a direct improvement over the original ARAPUCA design because the number of reflections on the internal sides of the X-ARAPUCA module is reduced which in turn increases the photon detection efficiency [73].

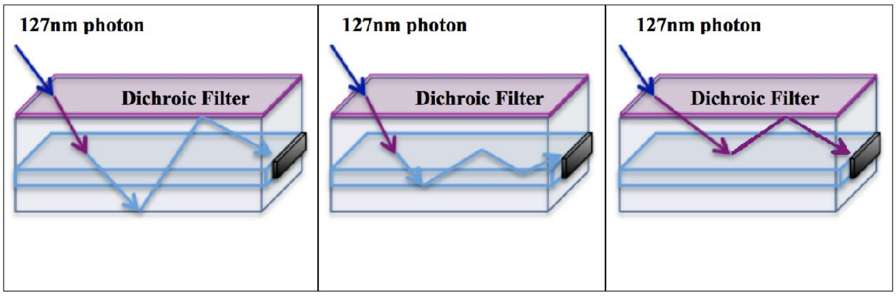

Figure 3.10.: The three possibilities for trapping light in an X-ARAPUCA. Left: The standard ARAPUCA design. Light is wavelength shifted in order to pass through the dichroic filter. Once passed the filter, it is wavelength shifted again so that may not exit through the filter again. The photons are reflected within the ARAPUCA until they are detected by the photo-sensor. Middle: an acrylic slab containing the inner wavelength shifter is placed in the X-ARAPUCA and the photo-sensor is attached to the slab. Light may be become trapped within the slab by total internal reflection. Right: Incident light at a large angle may become trapped between the surface of the slab and the filter [73].

Another component of the PDS is covering each side of the CPA with a 19 m^2 of TPB coated reflective covering. This means that VUV light directed towards the CPA will be wavelength shifted into the visible spectrum and reflected back to towards the PMTs where it may be detected. Since one of the PMTs in each of the boxes remains uncoated, it will allow SBND to distinguish between light that is initially directed towards the PMTs and the reflected light because the reflected light will be visible in all PMTs whereas only the four outer PMTs will be able to detect direct light [69].

3.5. MicroBooNE

The MicroBooNE detector is located slightly upstream of its predecessor, MiniBooNE. The detectors are at 470 m and 541 m from the BNB source respectively. The principal design goal of MicroBooNE is to investigate the low energy excess of events observed by MiniBooNE and it began its operations in 2015 were it was initially used as a stand alone detector before becoming part of the larger SBN program [74].

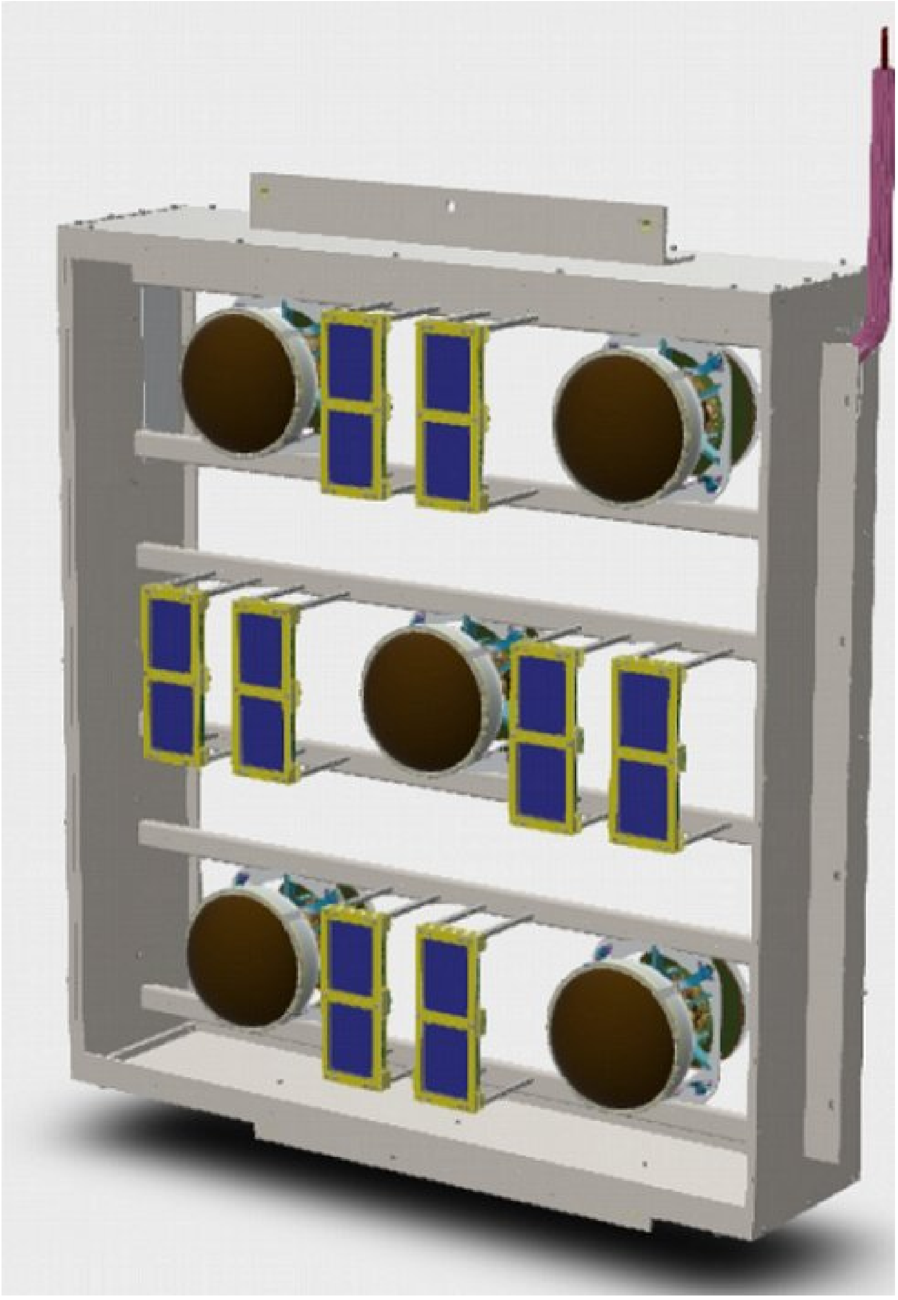

Figure 3.11.: Schematic of the PDS box showing the position of the 5 PMTs and the 4 pairs of X-ARAPUCA'S. The central PMT is left uncoated, whilst the 4 outer PMTs are coated with TPB [69].

The MicroBooNE detector consists of a single TPC enclosed within a cryostat as is shown in Figure 3.12. The TPC has dimensions of (2.560, 2.325, 10.368) m and

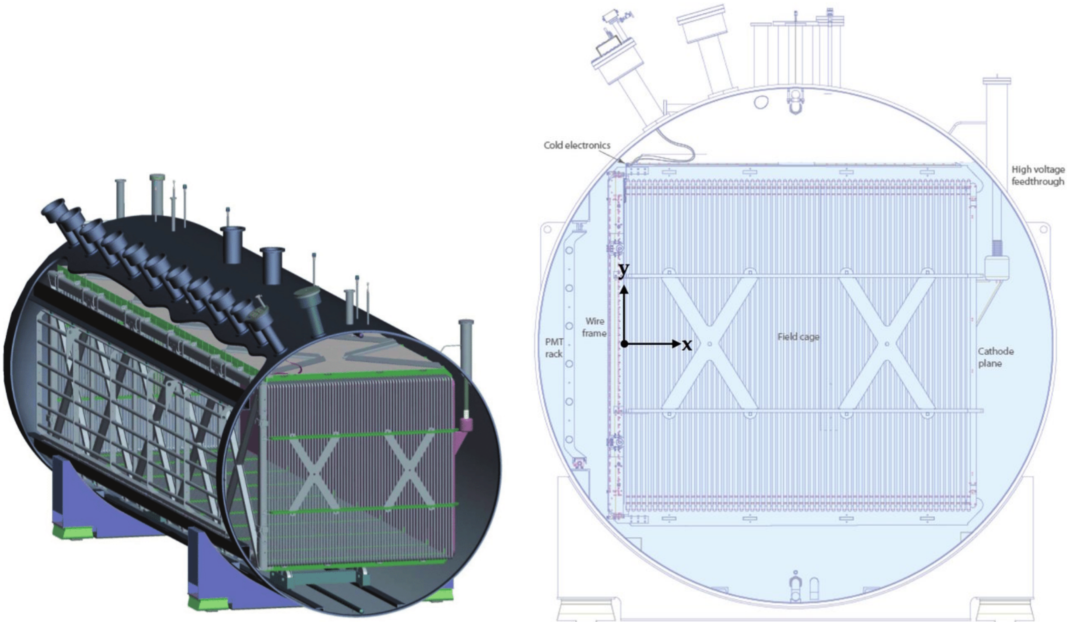

Figure 3.12.: Diagram of the MicroBooNE LArTPC inside the cryostat with the open front and left side showing the field cage and anode planes respectively (Left). Cross-section schematic of the MicroBooNE detector orientated such that the beam direction (z-direction) is orientated out of the page [74].

is orientated such that the z-direction is along the neutrino beam line with the cathode to the left of the beam and the anode to the right. The active volume is defined as the volume enclosed by the LArTPC field cage which has a liquid argon mass of 90 tonnes out of a total 170 tonnes. The APA consists of three wire planes with the wires on the two induction planes orientated at $\pm 60^{\circ}$ to the vertical and the wires of the collection plane orientated vertically. Both the wire plane spacing and the wire pitch of each plane is 3 mm. Unlike SBND and ICARUS, the nominal electric field in MicroBooNE is 273 V/cm. The light collection system consists of a series of 32 PMTs and 4 lightguide paddles which are located directly behind the anode planes. The lightguides have a large collection area and their purpose is to guide light to the PMTs (the lightguide paddles were disfavoured once the ARAPUCA technology was developed.) [74].

MicroBooNE is also considered a surface level detector being only ~ 6 m underground and as there is no overburden present, a large flux of cosmic rays are observed. A CRT system similar to the one described in Section 3.4 for SBND was implemented. The CRT system consists of 73 scintillating modules, however it is only sensitive to the four sides of the X and Y coordinates of the detector [71].

3.6. ICARUS

The ICARUS detector was first operated in 2010 and located at the Gran Sasso National Laboratory in Italy where it was used to detect events from cosmic rays and from the neutrino beam which is directed from CERN to Gran Sasso. In 2013 the decommissioning process began and the detector was taken to CERN for refurbishment before making its way to Fermilab and becoming part of the SBN program [11].

The ICARUS detector consists of two *modules* within a single cryostat with each module containing two TPCs. A schematic of this design is shown in Figure 3.13. Similar to SBND, the two TPCs within each module share a common cathode. The dimensions of each module are (3.6, 3.9, 19.6) m and the cryostat contains 760 tonnes of liquid argon with an active volume of 476 tonnes. Again, the APAs consists of three wire planes with a wire plane spacing and wire pitch of 3 mm. In contrast to SBND and MicroBooNE however, the wire planes are orientated horizontally for the first induction plane and at $\pm 60^{\circ}$ for the second induction plane and the collection plane. The choice of having a horizontal wire plane is due to ICARUS being initially designed to detect cosmic rays which would predominantly enter the detector from above and therefore be travelling perpendicular to the horizontal. The nominal electric field in each of the TPCs is 500 V/m [11].

Again, consistency with information content.

The light collection system for ICARUS is comprised of a series of 74 PMTs positioned behind the wire planes. The layout of the PMTs is, however, asymmetric with the east module having a 3×9 array of PMTs for each TPC whereas the two TPCs in the west module have a single row of 9 PMTs plus two additional PMTs located centrally above and below the main row in the right chamber. Since the light is again produced with wavelengths in the VUV region, the PMTs are coated with TPB in order to shift the wavelength into the visible region [11].

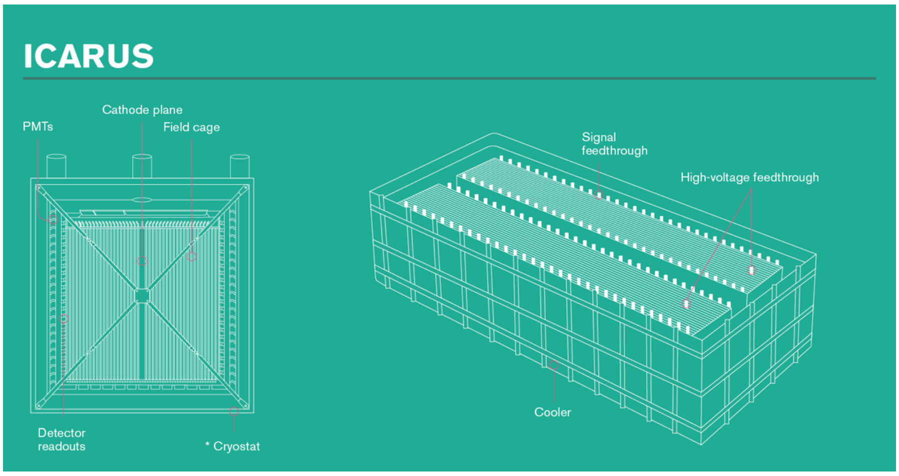

Figure 3.13.: Schematic of of the ICARUS detector. The left image shows a cross-section of one of the two modules whereas the right images shows the whole detector with the the two modules side by side [75].

The ICARUS CRT system surrounds the detector on all sides however the actual position is not always the same due to design choices. The CRT on the top most side which experiences the highest flux of cosmic rays, is located outside the TPC, about 3m from the top face above the readout electronics. It consists of two planes of scintillating modules with the readout coming from the same electronics board as is used by SBND. The CRT for the vertical sides are again outside the TPC and behind the PMT arrays and close to the cryostat walls. The scintillator modules from the MINOS experiment are being reused for this purpose. The CRT for the bottom face are the repurposed spare modules from the veto shield from the Double Chooz experiment and are located within the cryostat. Only about 50% of the bottom face is covered by the CRT because of limited space due to the supporting structure of the cryostat [11] [76].

3.7. SBN Physics Capabilities

The SBN program was designed with the aim of resolving the contentious results observed by a number of experiments as was discussed in Section 2.3. Since it was purposely planned with this in mind, the SBN program has a number of advantages over previous experiments in the hopes of detecting eV scale sterile neutrinos: it has a multi detector design, the near and far detector are positioned such that the oscillation signal is close to maximal for an expected set of oscillation parameters, the detectors use the same technology and have the same target medium [13].

The top two plots of Figure 3.14 show the expected oscillation probability for the ν_e appearance channel as a function of the baseline for two sets of oscillation parameters, $(\sin^2 2\theta_{\mu e},\ \Delta m^2_{41}) = (0.015,\ 0.3\ \text{eV}^2), (0.002,\ 1.5\ \text{eV}^2)$ and a neutrino energy of 700 MeV. The neutrino energy corresponds to the peak energy of the BNB and the oscillation points are chosen as the upper and lower limits of the global ν_e appearance data. In both cases there is a clear difference in the oscillation probability between the near and far detector showing that the SBN program is sensitive to oscillations within this parameter range [13]. The bottom two plots show the oscillation probability for the same two oscillation points as a function of neutrino energy for baselines of 110 m and 600 m. The ratio of the oscillation probability at 600 m to that at 110 m is also shown. Again, there is a clear difference in the oscillation probability for most energies showing that the SBN program is sensitive to a wide range of neutrino energies [13]. The ν_e appearance oscillation sensitivity constructed at the time of the proposal is shown in Figure 3.15. These contours include the relevant backgrounds and systematic uncertainties with the exception of detector systematics.

As Figure 3.14 shows, SBND will observe no or very few oscillated events and will give a measure of the absolute flux and interaction cross-section whereas both MicroBooNE and ICARUS are able to detect oscillated events with significant probability. Typically the BNB flux uncertainties and interaction cross-section uncertainties are fairly large, however, since SBND, MicroBooNE and ICARUS use the same interaction medium and the same technology to detect interactions, the uncertainties may be constrained [13].

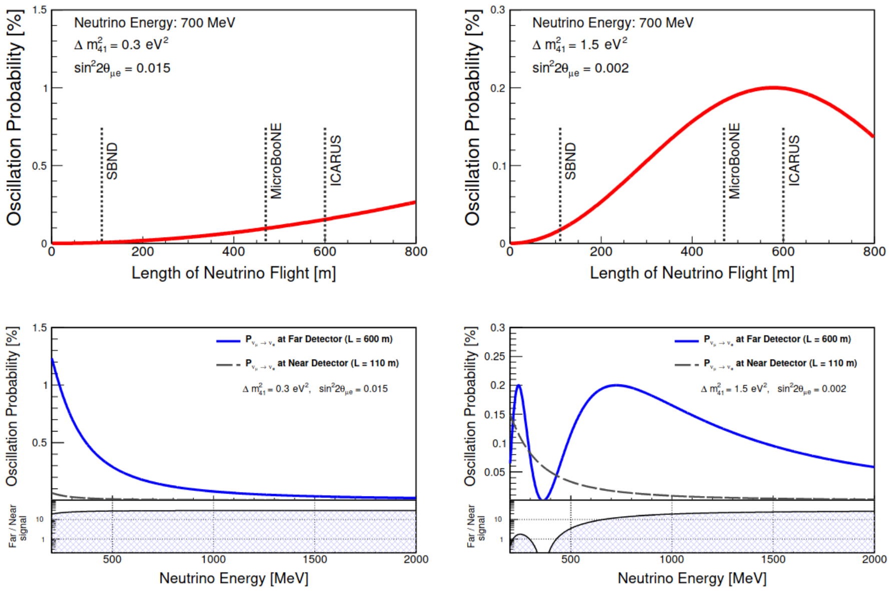

Figure 3.14.: The oscillation paramters used in the two left and right plots are $(\sin^2 2\theta_{\mu e},\ \Delta m^2_{41}) = (0.015,\ 0.3\ \text{eV}^2), (0.002,\ 1.5\ \text{eV}^2)$ respectively. Top: The oscillation probability as a function of the baseline for the ν_e appearance channel. A neutrino energy of 700 MeV is used in both cases. Bottom: The oscillation probability is shown as a function of neutrino energy in both the near and far detector. Additionally, the ratio of the oscillation probabilities between the two detectors is also shown. [13]

This main goal of the SBN program revolves around sterile neutrino oscillation analyses, however, the close proximity of the SBN detectors and in particular SBND to the neutrino beam source will allow for a high statistics study of neutrino argon interactions. This will provide valuable information for future liquid argon based experiments such as DUNE. SBND is expected to observe on the order of 2 million neutrino CC interactions a year which is sufficient to be able to minimise the associated uncertainty to a point such that systematic uncertainties become dominant. As the BNB consists predominantly of ν_μ's, most events will also be ν_μ based, however the ν_e fraction of the BNB is sufficient to expect 12,000 ν_e events a year in SBND which is enough to perform both inclusive and exclusive analyses. There is also the opportunity to measure rare channels with a big increases in statistics or possibly even for the first time such as final states involving hyperons or $\nu_e \to \nu_e$ elastic scattering [13] [77].

not clear what this is, what would be the target? or do you mean ν-e elastic scattering?

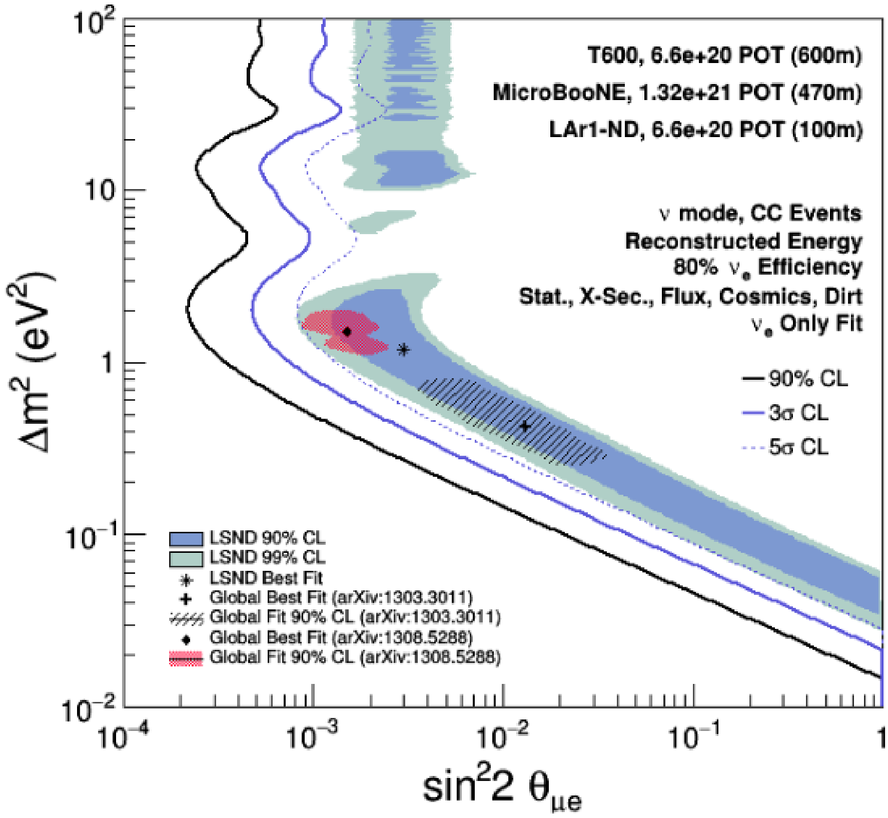

Figure 3.15.: The expcted ν_e appearance sensitivity from the SBN program using inputs constructed at the time of the SBN proposal. Limits from LSND and global best fit results are also shown [11].

The large event rate and the high resolution event reconstruction provided may allow the SBN program to be sensitive to BSM physics other than sterile neutrino oscillations [13]. The potential areas include, but are not limited to,

- Light Dark Matter - Assuming a dark matter particle has an associated light mediator particle which interacts with quarks, the high intensity proton beam will produce a dark matter beam alongside neutrinos. The dark matter particles will propagate to the detectors alongside the neutrinos where they may scatter off the argon nuclei. Neutrinos will however represent a large background in such a search [13].
- Large Extra Dimensions - The neutrino mass scale could be explained by the presence of additional dimensions. The right handed neutrinos would be

able to propagate in the extra dimensions whilst the active neutrinos would be confined to the standard dimensions [13].

- Heavy Sterile Neutrinos - If heavy sterile neutrinos such as those present in the seesaw-mechanism discussed in Section 2.4.1 are of an MeV mass scale, they may be produced in the BNB via meson decay. They would then propagate along the beam line and their decay products may be observed in the detectors [13] [78].

- Dark Neutrinos - A beam neutrino interacts with an argon nucleus and scatters to a dark neutrino. The dark neutrino decays to a dark boson (and neutrino) and in turn the dark boson decays to an $e^+ e^-$ pair. This mechanism could provide an explanation to the MiniBooNE low energy excess [13] [79].

Chapter 4.

Electromagnetic Shower Energy Reconstruction in SBND

The EM shower energy is an important quantity that is used in a number of areas especially in the context of a ν_e analysis. One of the primary uses is in calculating the reconstructed electron neutrino energy, which is a key component of neutrino oscillations since the oscillation probability depends on $\frac{L}{E}$. The neutrino energy is usually found by summing up the energy of all the outgoing products of a neutrino interaction to which (for ν_e CC QE interactions) the shower energy is expected to make the dominant contribution [80]. ~~Another use is in the ν_e event selection (which is detailed in Section 5.3.2) where a direct cut based on the shower energy is applied to the events.~~

get rid of this.

Give an overview of the structure of the chapter. it's not clear what the reader is supposed to expect.

4.1. Event Simulation and Reconstruction

Event simulation and analysis is performed using the Liquid Argon Software (LArSoft) framework which interfaces with a number of other frameworks such as Generates Events for Neutrino Interaction Experiments (GENIE) for neutrino interaction generation, GEometry ANd Tracking (GEANT4) for simulated particle tracking and Pandora for pattern recognition and 3D reconstruction [81] [82] [83] [84]. LArSoft has been designed to work for many liquid argon based neutrino experiments, including the SBN program, with many of the underlying algorithms being common to all experiments [85] [86].

Reconstructed quantities are the main focus of this chapter and these are typically derived from the reconstructed charge which is obtained in the following steps;

1. Drifting electrons induce current on a wire at the anode.

2. Apply signal processing techniques to remove the effects of the E-field, electronics and some frequency dependent noise.

3. A hit finding algorithm identifies any significant waveforms and classifies these as hits across a certain time window (number of ticks).

4. The Pandora pattern recognition software clusters the hits together such that they represent an individual particle. This is initially done in 2D, followed by matching the clusters between the wire planes in order to produce 3D clusters.

5. The lineage of the particles is identified and the particles are classified as either track- or shower-like.

A number of different hit finding algorithms exist, but the default one used by LArSoft is the *GausHitFinder*. Once the algorithm has identified a waveform that peaks above some threshold (the threshold in SBND is 10 Analog Digital Converter (ADC) counts), it attempts to fit one or more Gaussians to the waveform. For each peak, the centre and width are identified and these values are used to produce the associated Gaussian fit. For most cases the *GausHitFinder* works well, but two areas where it can struggle are resolving hits which are closely spaced and fitting a Gaussian to waveforms that are not well represented by a Gaussian. The latter tends to occur when charge is directed towards the wire planes (e.g. from a shower that was produced at a large angle to the beam line instead of being mostly forward going) which causes a long pulse train on but a few wires. This results in ~~long~~ waveforms where the ADC count is above threshold for many ticks and is without a clear central peak. These ~~long~~ waveforms may be better represented by a series of N-Gaussians, however, this is still far from perfect and fitting a large number of peaks can appreciably increase computing time [87]. Figure 4.1

the length of the waveform is the same because it's the same readout window shows examples of some waveforms in blue along with the attempted Gaussian fit in red. The top plot shows an example waveform that is well represented by a Gaussian, whereas in the bottom plot there is a long waveform with a number of different peaks to which the *GausHitFinder* has attempted to fit a single Gaussian. This long waveform is not representative of a single Gaussian and therefore the associated reconstructed charge will deviate significantly from the true value.

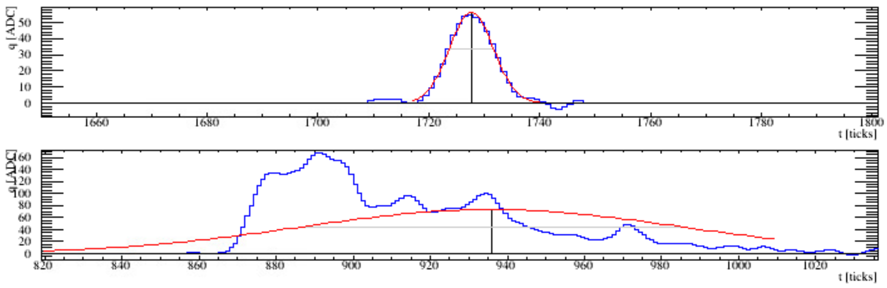

Figure 4.1.: Waveforms (blue) that have been fitted with a Gaussian (red) from the *GausHitFinder*. Top: an example of a waveform that is well represented by a Gaussian. Bottom: an example of waveform that is not well represented by a Gaussian.

4.2. Overview of Shower Energy Reconstruction in SBND

Currently, there are three algorithms available for reconstructing EM shower energy within SBND as part of the *LArPandoraShower* suite of tools, each of which is described below. Regardless of the algorithm used, the initial approach is the same for all three methods which is as follows,

1. Identify the hits associated with a given wire plane.
2. Integrate the hits to obtain the associated charge in ADC units whilst correcting for electron lifetime.
3. Convert the charge in ADC units to a conventional charge (number of electrons) using the calibration constant which is part of the calorimetry algorithm (this step was not performed in the case of the *Linear Energy tool*).

Once the charge of a hit has been determined, the final steps which involve converting the charge to energy become method dependent. The other major detector effect that still needs to be considered is recombination, which is modelled by the Modified Box Recombination Model and given by

$$\frac{dE}{dx} = \frac{\exp\left(\frac{\beta}{\rho\mathcal{E}} W_{ion} \cdot \frac{dQ}{dx}\right) - \alpha}{\frac{\beta}{\rho\mathcal{E}}}, \tag{4.1}$$

where $\frac{dE}{dx}$ is the deposited energy per unit length, $\frac{dQ}{dx}$ is the deposited charge per unit length, $\mathcal{E}$ is the electric field in the detector, ρ is the density of liquid argon, $W_{ion} = 23.6$ eV which is the energy required to ionise an argon atom, $\alpha = 0.93 \pm 0.02$ and $\beta = 0.212 \pm 0.002$ (kV/cm)(g/cm^2)/MeV. The values for parameters α and β are results from the Argon Neutrino Test Stand (ArgoNeuT) experiment [88]. The recombination correction, R, is given by $\frac{\frac{dQ}{dx} \cdot W_{ion}}{\frac{dE}{dx}}$.

Since the recombination model is $\frac{dE}{dx}$ dependent, an accurate path length, dx, is needed which requires 3D reconstruction of the direction. Because a shower is treated as a single object, which means the trajectory of constituent components are not tracked, it is therefore not straightforward to directly correct for the recombination effect [89]. Two different approaches have been considered and are discussed in the relevant energy reconstruction methods below: 1) assume a nominal recombination value for all hits and 2) use a lookup curve which relates the collected charge to energy which circumvents the need to evaluate a recombination correction directly because it already gets accounted for in the curve.

In the analysis and validation of the shower reconstruction, a number of *true* and *reconstructed* quantities are considered. Care must be taken that it is clear what each value relates to. For clarity, the following quantities are explicitly described;

- Collected charge (or energy): This is the charge that is seen by the wire planes.
- Deposited charge (or energy): This is the charge that is initially deposited in the detector. Typically this would be obtained from the collected charge by correcting for the electron lifetime and the recombination effect.

- Hit energy: This is the energy associated with each individual hit. Both true and reconstructed values may be obtained.
- Energy of showering particle: This is the energy of the particle which results in the shower which is being investigated.

4.2.1. Linear Energy Tool

The first shower energy reconstruction method developed was the *Shower Linear Energy tool*. This tool relies on the linear relationship between the true energy deposited in the detector and the reconstructed charge from Minimum Ionising Particle (MIP) muons. A sample of simulated muons are used as calibration because the $\frac{dE}{dx}$ value for electrons and MIP muons are not dissimilar. The relationship between the charge obtained from the hits due to the muons and the energy deposited by the muons is shown in Figure 4.2. A linear relationship such as this is comparable to assuming a constant recombination factor.

To estimate the reconstructed shower energy, the charge found to be associated with a shower would be used to directly read off the associated energy from the linear calibration. A further recombination correction is not required as it has already been accounted for in the charge to energy conversion. It should be noted that along with the recombination correction, hit reconstruction and pattern recognition inefficiencies are also corrected for in the calibration curve. The *Shower Linear Energy tool* has been largely disfavoured since the development of the two other reconstruction tools.

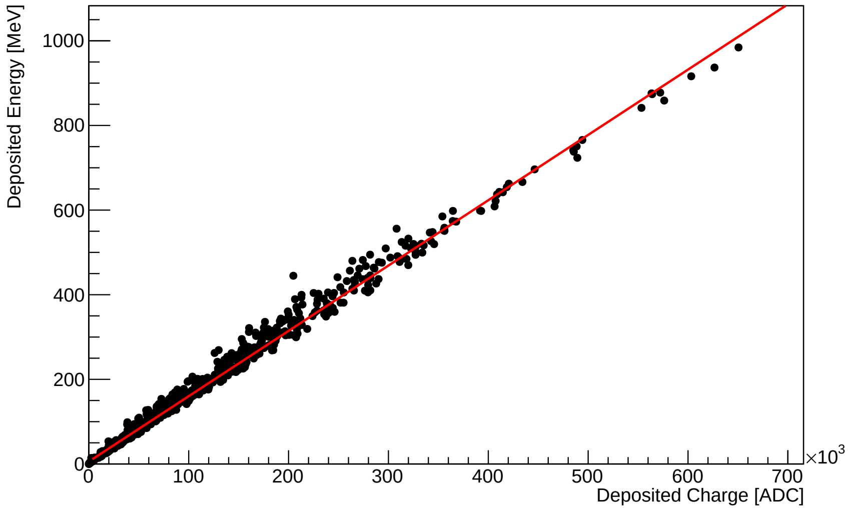

Figure 4.2.: The linear relationship between deposited charge and energy. Produced from a sample of muons used for calibrating the *Shower Linear Energy tool*.

4.2.2. Number of Electrons to Energy

The *Shower Num Electrons Energy tool* was developed to move away from being reliant on in-house calibration curves and instead use the pre-existing calibration available in the SBND portion of the LArSoft framework. This has the advantage of being much more flexible to physics changes. For example a change in the recombination correction could be investigated by changing a single number, whereas, for the *Shower Linear Energy tool*, the calibration curves would have to be regenerated. The number of electrons are found from the ADC charge and are then directly converted to energy using a scale factor which is the inverse of the energy required to ionise an argon atom. A nominal recombination value of 0.64 is assumed which is applied to all hits.

The nominal recombination value was calculated by simulating electrons whilst using a large (effectively infinite) value for the electron lifetime and setting both the transverse and longitudinal diffusion coefficients to zero. The only detector effect remaining that may impact the collected energy is the recombination effect and therefore taking the ratio between the collected and deposited energy will give a value for the recombination effect. For electrons, it was found that the what units?

recombination effect was fairly constant at a value of 0.64 across a broad range of energies [90].

4.2.3. ESTAR Method

The *Shower ESTAR Energy tool* combines the ESTAR database provided by the National Institute of Standards and Technology (NIST) along with the Modified Box recombination model in an approach that was first used by the ArgoNeuT experiment [91]. The ESTAR database provides the track length of electrons in various materials, including liquid argon, for energies ranging from 0.01 MeV to 1000 MeV [92].

$\frac{dE}{dx}$ values may be calculated by dividing the energy by the track length for each entry in the ESTAR database. The deposited charge, Q, can then be found by using Equation 4.1 to find $\frac{dQ}{dx}$ and multiplying by the track length, dx. This now allows the collected charge and energy to be related. If $\mathcal{E}$ in Equation 4.1 is taken to be a variable, the above process may be repeated whilst iterating over a set values of $\mathcal{E}$. This results in a 3D curve relating both the deposited charge and electric field to energy as is shown in Figure 4.3. The energy may then be interpolated from the collected charge and the appropriate electric field. As with the *Shower Linear Energy tool*, a direct correction for recombination is not needed as it is again accounted for in the lookup curve.

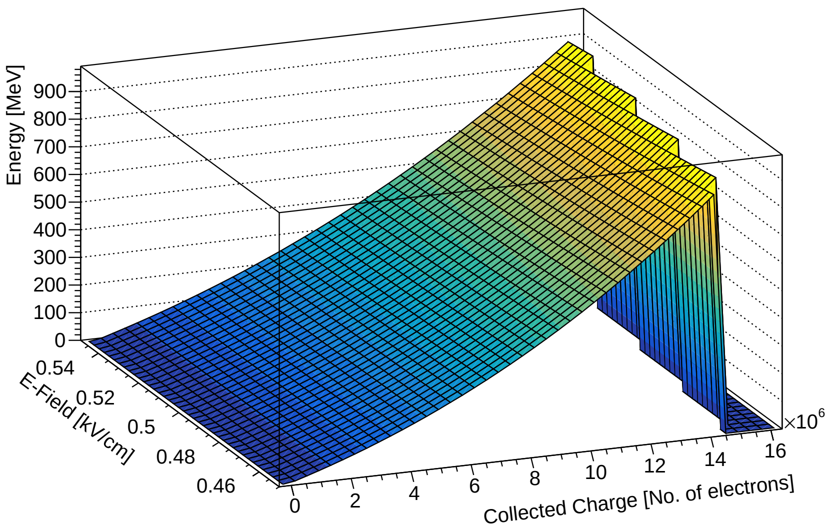

Figure 4.3.: ESTAR lookup curve generated from the ESTAR database and the Modified Box Recombination Model.

4.3. Shower Energy Reconstruction Performance

In order to assess the performance of the different reconstruction methods, a comparison with *truth* information is performed. Depending on the approach, a few other inefficiencies should be considered, namely that the hit reconstruction and Pandora pattern recognition are not perfect [84]. This results in hits missing due to not being reconstructed plus the addition of the clusters that Pandora produces being incomplete. Therefore, there are typically fewer hits than there would be if the shower in question were to be perfectly reconstructed. Reconstructing the energy of the showering particle, is desirable for a number of analyses, however, due to these issues, it is not realistic to expect agreement ~~to~~ within a few percent. Improving the hit reconstruction or the pattern recognition within Pandora would clearly help, but it is likely that a non-negligible bias would remain. Work on Pandora, the hit reconstruction and addressing any remaining bias is however beyond the scope of this chapter. To circumvent the inefficiencies in Pandora's pattern recognition, Pandora is run in *cheating* mode, which means that truth information is used to perform the clustering. This decouples the reconstruction methods from any effects due to Pandora's pattern recognition. For comparison, a number of figures showing the reconstruction performance without using Pandora in cheating mode are shown in Appendix C.

To purely gauge the performance of a given reconstruction method, it is probably best to compare the truth and reconstructed energy of a shower by only considering the available hits. This way, the reconstruction method is only validated from the available information and is additionally decoupled from hit reconstruction inefficiencies. However, additional care must be taken when using the true energy of the hits. What is considered a hit is user defined in that the width that defines a hit is a parameter that may be changed. Therefore, the true energy associated with a hit is dependant on the chosen width. Within LArSoft, the default width of a hit is 1σ which is chosen to try and find a balance between covering a sufficient amount of charge whilst still being able to resolve multiple hits which are closely spaced. The hit width considered here has been left at the default value of 1σ.

Generally, the validation is performed on a shower-hit level. This means that for a given shower, the energy of each hit is reconstructed and then summed together to obtain the energy of the shower. The exception to this is in the case of the *Linear Energy tool*. During its development, it was customary to sum up the charge of all the hits and then convert to energy. This is why the calibration curve in Figure 4.2 has energies on the order of a shower level and not a hit level (individual hit energies are usually $\lesssim 5$ MeV) and also why it is possible to evaluate shower energies above 1000 MeV using the ESTAR method.

4.3.1. Validation of a BNB Sample

In order to validate the reconstruction methods, an $e^- + \pi^+$ vertex sample with BNB-like properties was produced where the electron is the showering particle. The pattern recognition is comprised of a number of steps some of which rely on the reconstructed vertex. It is therefore important to correctly reconstruct the vertex to avoid inaccuracies in the pattern recognition and it is usually easier to accurately reconstruct the vertex of an event if two particles are emanating from a single point rather than just one particle. Unless otherwise stated, all the validation has been performed using the collection plane.

The true vs reconstructed energy is shown in Figure 4.4 for all three methods where the true energy has been calculated from the shower hits. The results from the *Shower Linear Energy tool* and the *Shower ESTAR Energy tool* are similar and show good agreement between true and reconstructed energies across the whole energy range whereas the *Shower Num Electrons Energy tool* tends to overestimate the hit energies. Figure 4.5 is similar, but instead the true energy is the energy of the showering electron. This gives a measure of the bias each method can expect due to the inefficiencies mentioned above. Both the *Shower Linear Energy tool* and the *Shower ESTAR Energy tool* underestimate the true energy of the showering electron as is expected. The *Shower Num Electrons Energy tool* shows better agreement due to systematically applying a higher energy to individual hits which compensates for other inefficiencies.

what are they?

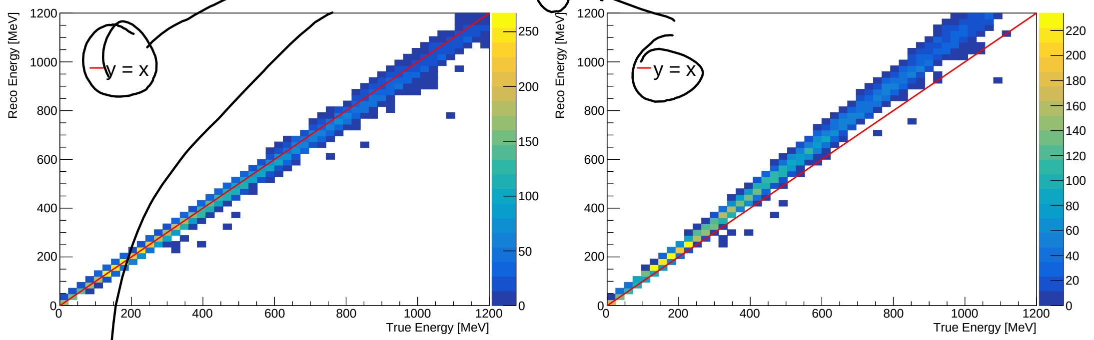

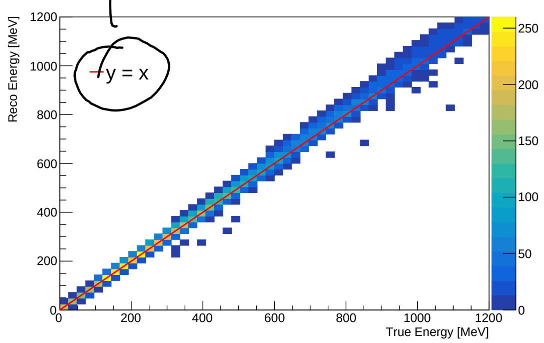

Figure 4.4.: True vs reconstructed energy from a showering electron. The true energy has been evaluated from the hits of each shower. Top Left: *Shower Linear Energy tool*, Top Right: *Shower Num Electrons Energy tool* and Bottom Left: *Shower ESTAR Energy tool*.

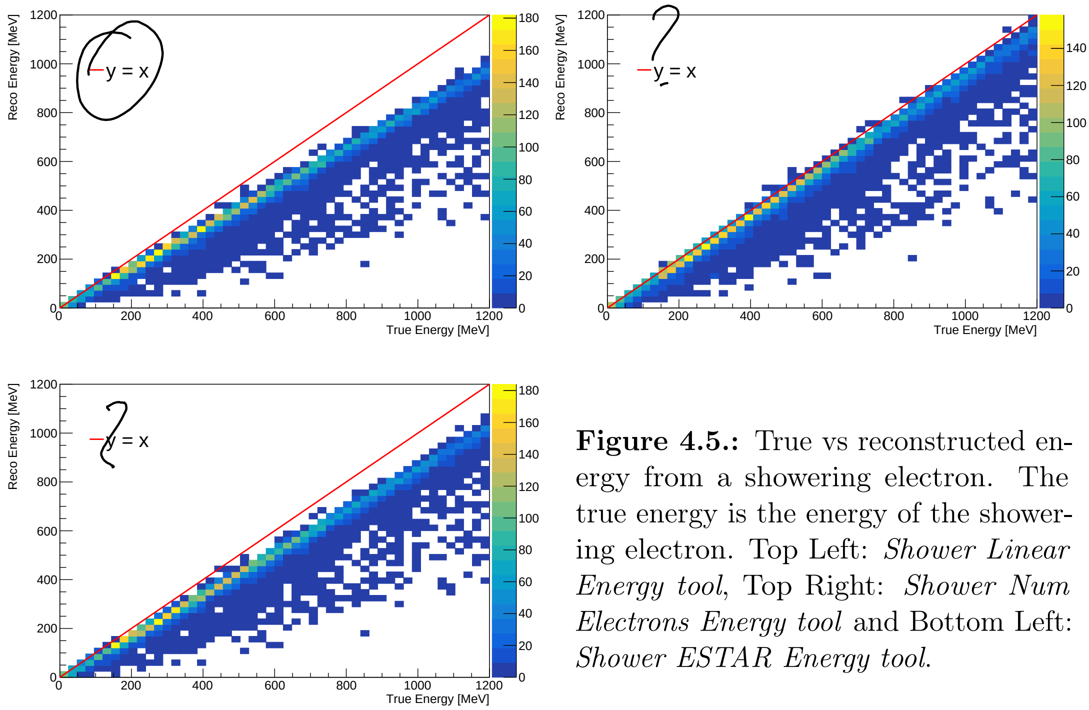

Figure 4.5.: True vs reconstructed energy from a showering electron. The true energy is the energy of the showering electron. Top Left: *Shower Linear Energy tool*, Top Right: *Shower Num Electrons Energy tool* and Bottom Left: *Shower ESTAR Energy tool*.

A comparison of the fractional energy separation, which is defined as $\frac{Reco-True}{True}$, is shown in Figure 4.6 for both true energies. When comparing with the true energy of the hits, the *Shower ESTAR Energy tool* peaks quite tightly around zero as does the *Shower Linear Energy tool*. The *Shower Num Electron Energy tool* peaks to the right of the zero line again indicating that the reconstructed quantity is an overestimate. All three distributions peak to the left of the zero line when comparing with the true energy of the showering particle with the *Shower Num Electrons Energy tool* giving the closest result.

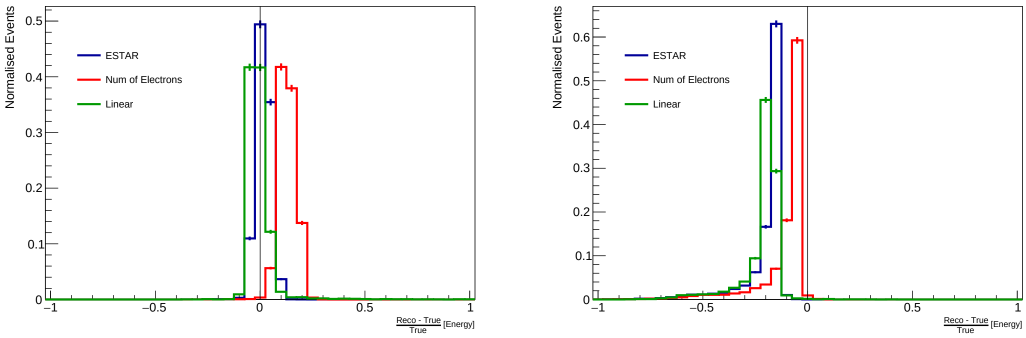

Figure 4.6.: Comparison of the fractional shower energy separation for the *Shower Linear Energy tool*, the *Shower Num Electrons Energy tool* and the *Shower ESTAR Energy tool*. Left: Using the true energy of the hits. Right: Using the true energy of the showering particle.

To get a measure of the resolution, which is defined as the width of the distribution, a Gaussian of the form

$$A \exp\left(-0.5\left(\frac{x-\mu}{\sigma}\right)^2\right), \tag{4.2}$$

is fitted to each distribution, where A is a constant that defines the peak of the Gaussian, μ is the mean value and σ^2 is the variance. σ is the quantity that defines the width of the Gaussian fit and will therefore also give a measure of the resolution of the associated distribution. For the distributions which use the true energy of the hits (the left plot of Figure 4.6), Gaussians are fitted to the entire distribution, whereas for the distributions using the true energy of the showering electron (the right plot of Figure 4.6), Gaussians are only fitted to the central region which encompasses the peak of the distribution. The reason for not fitting a Gaussian to the entire distribution in the second case is in order to avoid having the fit be influenced by the non Gaussian tail which is usually caused by issues in the reconstruction. Since the tail in the first case is minimal, this is not a concern and therefore a fit to the whole distribution is suitable.

The Gaussian fits to the fractional energy separation distributions of each of the three reconstruction algorithms are shown in Figure 4.7 and Figure 4.8 for the comparison with the true energy of the hits and the true energy of the showering electron respectively. In order for the resolution comparisons to remain valid, the Gaussian fits in Figure 4.8 are produced by considering the same x-axis range size. Additionally, the binning range has been chosen such that the distribution shapes are comparable in order to minimise binning effects on the fit width whilst maintaining the same bin width for each method. The corresponding σ values for each of the Gaussian fits is shown in Table 4.1.

The Gaussian fits in Figure 4.7 for the *Shower Linear Energy tool* and the *Shower ESTAR Energy tool* are fairly similar with *Shower Num Electrons Energy tool* having a slightly broader fit. This is likely due to the *Shower Num Electrons Energy tool* systematically assigning higher energy values to each of the hits which makes event migration across bins more likely. It should be noted that the Gaussian fits will be influenced by binning artefacts in the distributions which are then mapped to the resolution. The Gaussian fits for all three methods have a similar width in Figure 4.8. The effect from event migration across bins likley to be reduced due to the larger difference in energy between the sum of the hits and the showering electron.

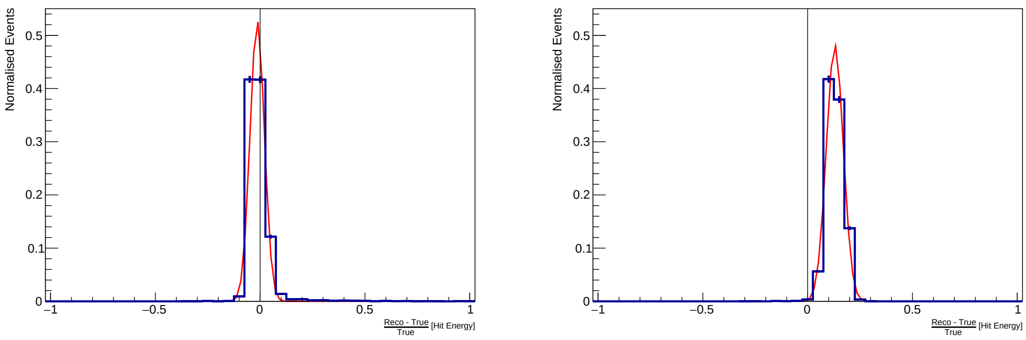

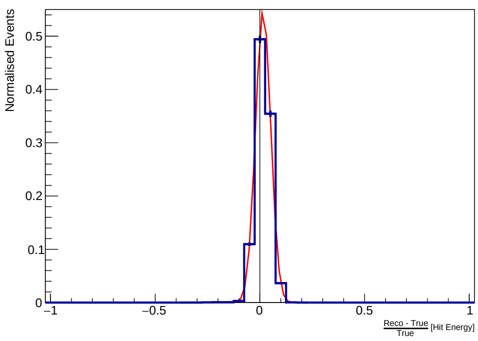

Figure 4.7.: The fractional energy separation using the true energy of the hits with an associated Gaussian fit of the entire distribution. Top Left: *Shower Linear Energy tool*, Top Right: *Shower Num Electrons Energy tool* and Bottom Left: *Shower ESTAR Energy tool.*

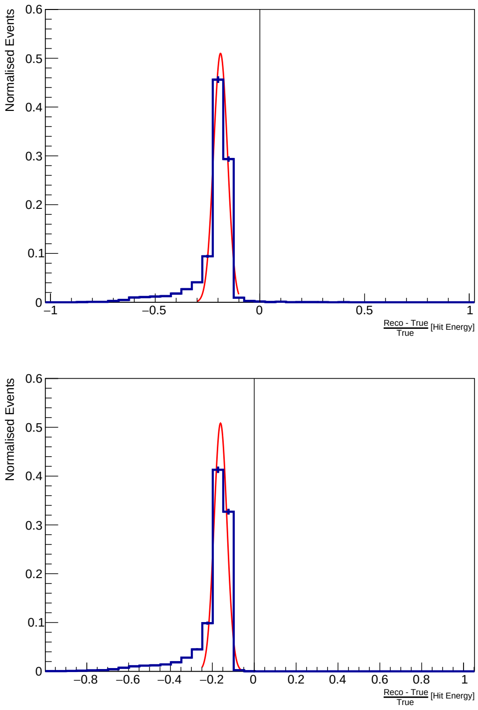

Figure 4.8.: The fractional energy separation using the true energy of the showering electron with an associated Gaussian fit of the entire distribution. Top Left: *Shower Linear Energy tool*, Top Right: *Shower Num Electrons Energy tool* and Bottom Left: *Shower ESTAR Energy tool*.

	σ of the Gaussian Fit	
Algorithm	Hits	Showering Electron
Linear	0.034	0.033
Num of Electrons	0.040	0.031
ESTAR	0.036	0.031

Table 4.1.: The σ value used in the Gaussian fit to the fractional energy separation distributions of each algorithm. Both the distributions which use the true energy of the hits (Figure 4.7) and the true energy of the showering electron (Figure 4.8) are shown.

To confirm that the reconstruction performance is comparable across all wire planes, the true vs reconstructed energy was also plotted for the two induction planes using the ESTAR method. This is shown in Figure 4.9 where the comparison has been made with the true energy of the hits.

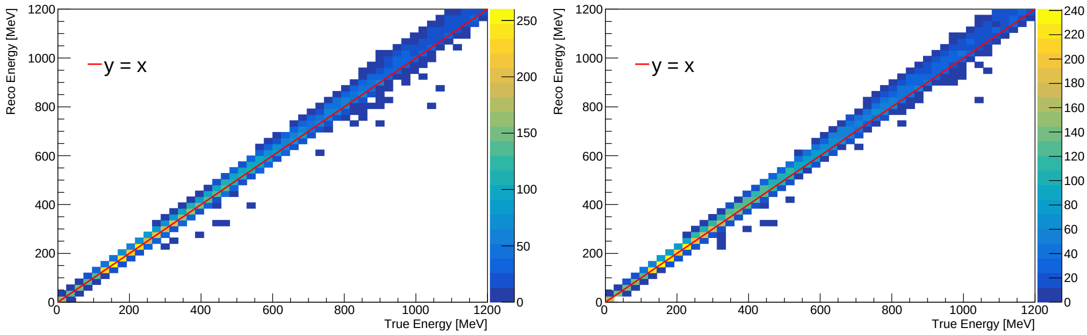

Figure 4.9.: True vs reconstructed energy from a showering electron for the first induction plane (Left) and the second induction plane (Right) using the ESTAR method. The true energy has been evaluated from the hits of each shower.

Since photons also produce EM showers, a BNB-like $\gamma + \pi^+$ sample was produced to verify that the reconstruction works equally well in this case. Figure 4.10 shows this using the ESTAR method with the hits from the collection plane.

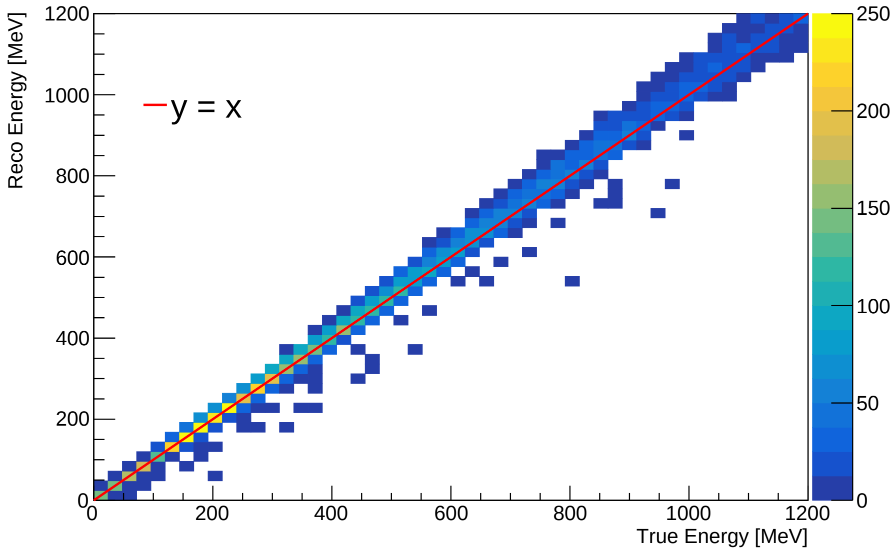

Figure 4.10.: True vs reconstructed energy from a showering photon using the ESTAR method with the hits from the collection plane. The true energy has been evaluated from the hits of each shower.

4.3.2. Performance as a Function of Angle

From a BNB neutrino sample, most of the showers are expected to be predominantly forward going. A fraction of showers will however be directed at large angles to the beamline. As was mentioned in Section 4.1, showers directed towards the wire planes tend to produce waveforms which are not well represented by Gaussians. Since the *GausHitFinder* has trouble applying a suitable fit to these cases, a degradation in the reconstruction performance is expected as a function of angle.

In order to verify this, an $e^- + \pi^+$ sample was produced with the electron being directed in all θ_{xz} angles. Otherwise, this sample is also BNB-like. θ_{xz} is the angle between the beamline and the positive x-direction and is defined in terms of the SBND coordinate system which is shown in Figure 4.11. The reconstruction performance is shown in Figure 4.12 using the ESTAR method for both definitions of true energy. Profiles of the histograms in Figure 4.12 are shown in Figure 4.13 where the y-axis error bars are the standard deviations. As is expected, a degradation in the reconstruction performance is observed in both cases as θ_{xz} tends away from $0°$. It should be noted that the degradations are in opposite directions which may be explained by the fact that at large angles, the reconstruction method tends to overestimate the energy of the available hits, but the hit reconstruction also suffers, so the overall fraction of hits representing the shower is reduced. Both the *Shower Linear Energy tool* and *Shower Num Electrons Energy tool* have a constant recombination correction and therefore the conversion from charge to energy is linear. The *Shower ESTAR Energy tool* is not perfectly linear but it is close, especially in the region up to $\mathcal{O}(10\text{ MeV})$. Therefore, there is essentially no angular variation among the three methods so results akin to Figure 4.12 for the *Shower Linear Energy tool* and the *Shower Num of Electrons Energy tool* would look almost identical only with the y-axis scaled appropriately.

if you need to define θ_{xz} θ_{yz} you need to add a vector in the diagram or it won't make sense

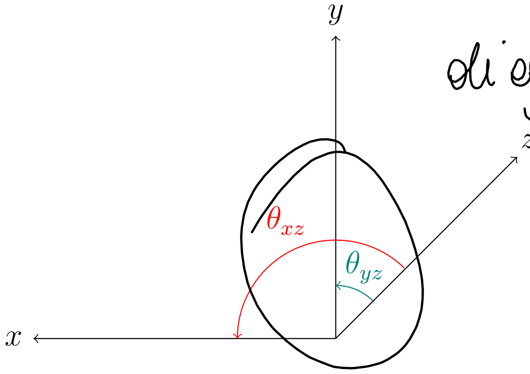

Figure 4.11.: The SBND coordinate system. The origin is located at the centre of the upstream face of the detector which is defined to be at (0, 200, 0) cm with the z direction being along the beamline.

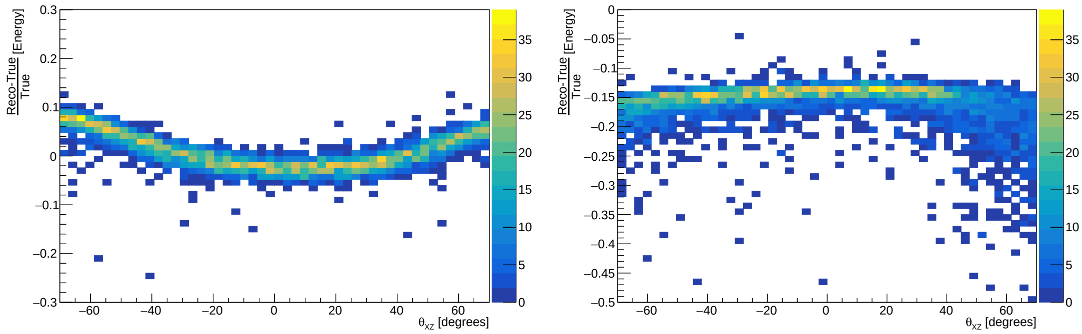

Figure 4.12.: The fractional energy separations as a function of θ_{xz} using the ESTAR method. Left: true energy is calculated from the hits. Right: true energy is the energy of the showering electron.

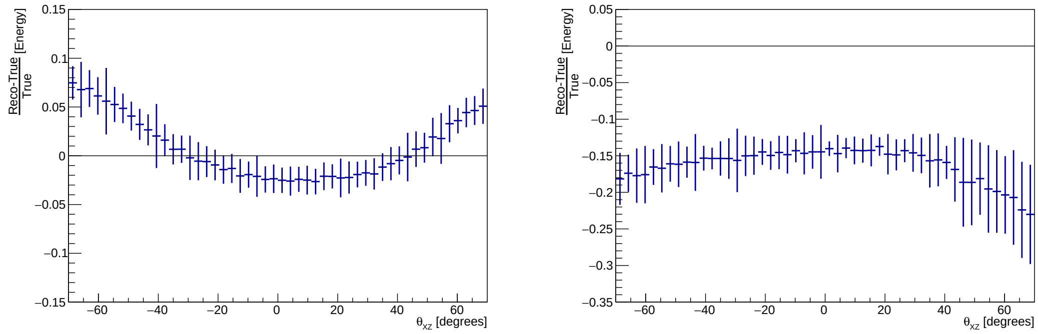

Figure 4.13.: Profile histograms of the fractional energy separation as a function of θ_{xz} using the ESTAR method. The profile histograms are constructed from Figure 4.12 and the y-axis error bars are the standard deviations. Left: true energy is calculated from the hits. Right: true energy is the energy of the showering electron.

4.3.3. Performance as a Function of Energy

The EM showers produced in SBND from the BNB are expected to have energies up to around a GeV. Since the energy range is relatively broad, the reconstruction performance is evaluated as a function of the energy in order to confirm that the reconstruction methods work sufficiently well for all energies. As was the case for the angular dependence, the performance as a function of true energy is expected to not be method dependent. The only difference would be a y-axis scaling due the different reconstruction performances.

On the whole, the fractional separation is observed to be fairly constant across all energies when comparing with both the true energy of the hits and the true energy of the showering particle as can be seen in Figure 4.14. The fractional energy separation is slightly lower at the lowest energies especially when comparing with the true energy of the showering particle. This is highlighted in Figure 4.15 which shows the profiles of the histograms of the fractional energy separation as a function of true energy and can likely be explained by a greater fraction of the hits not passing the threshold cut.

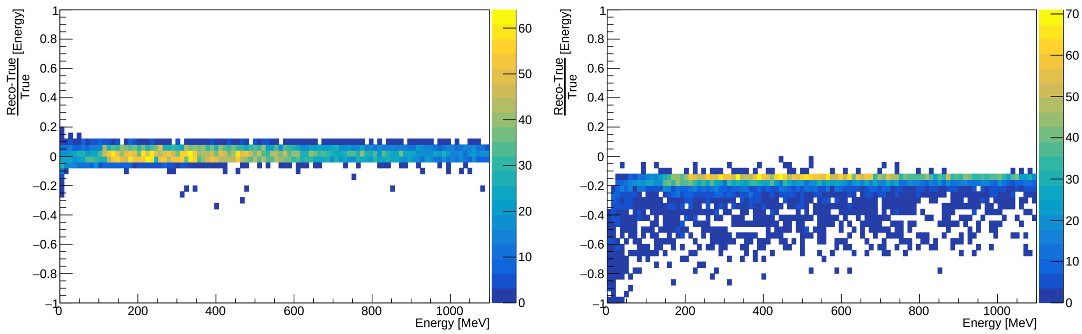

Figure 4.14.: The fractional energy separations as a function of true energy using the ESTAR method. Left: true energy is calculated from the hits. Right: true energy is the energy of the showering electron.

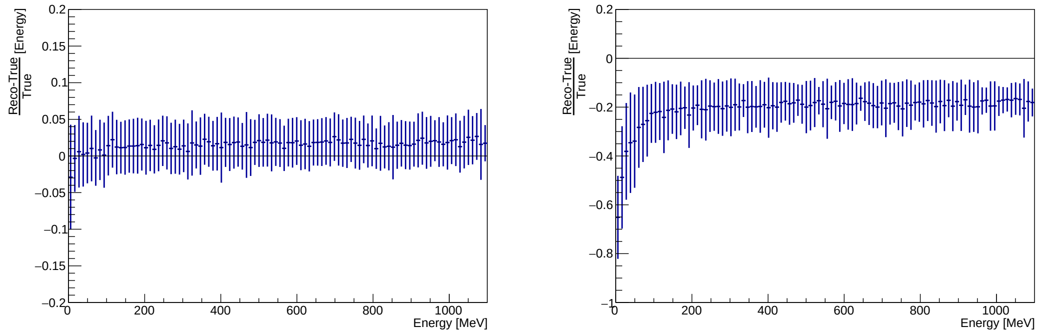

Figure 4.15.: Profile histograms of the fractional energy separation as a function of true energy using the ESTAR method. The profile histograms are constructed from Figure 4.14 and the y-axis error bars are the standard deviations. Left: true energy is calculated from the hits. Right: true energy is the energy of the showering electron.

4.4. Summary of EM Shower Reconstruction

The EM shower reconstruction algorithms have been demonstrated to work consistently across all three wire planes in SBND for showers originating from both electrons and photons. The reconstructed energy obtained from the *Shower Linear Energy tool* and the *Shower ESTAR Energy tool* show good agreement with the true energy of 1σ width hits with the *Shower ESTAR Energy tool* performing slightly better. The *Shower Num Electrons Energy tool* systematically assigns a slightly higher energy to each of the hits. All three methods underestimate the true energy of the showering particle due to inefficiencies in the hit reconstruction plus the expected presence of an overall bias. The *Shower Num Electrons Energy tool* has the closest agreement with the true energy of the showering particle due to assigning higher energies to the individual hits.

The reconstruction performance is fairly consistent across all shower energies that are expected to be seen by the BNB. There is however a slight dip in performance at the lowest energies when comparing with the true energy of the showering particle. This is due to a greater percentage of hits having energies below the threshold value. The reconstruction performance also degrades as the angle at which showers are produced to the beamline increases. This is not expected to be much of a concern as the majority of showers will be forward going.

Chapter 5.

Sterile Neutrino Oscillation Inputs Within SBN

In order to perform an oscillation analysis, a number of inputs and analysis choices are required. Typically this involves generating some event sample in each detector for a given analysis, applying a physics hypothesis and some set of systematic uncertainties. A fit comparing the observed and predicted event rate is then performed giving the confidence level of the applied physics hypothesis. This is summarised in Figure 5.1 which shows the generic overview of the procedure coupled with the different components. Many of these items are common to all oscillation analyses and are agnostic to the fitting framework. The remainder of this chapter highlights some of the key inputs to the oscillation analysis along with some of the decisions that were made. The actual analysis results are detailed in Section 6 in addition to explaining how the VALOR framework processes or consumes these inputs where appropriate.

5.1. Monte Carlo Event Production

The events used in this oscillation analysis are truth based with a *pseudo reconstruction* applied. Work on the reconstruction is still in progress and at the time of writing has not been sufficiently completed for it to be possible to generate a fully reconstructed event sample. The pseudo reconstruction involves applying

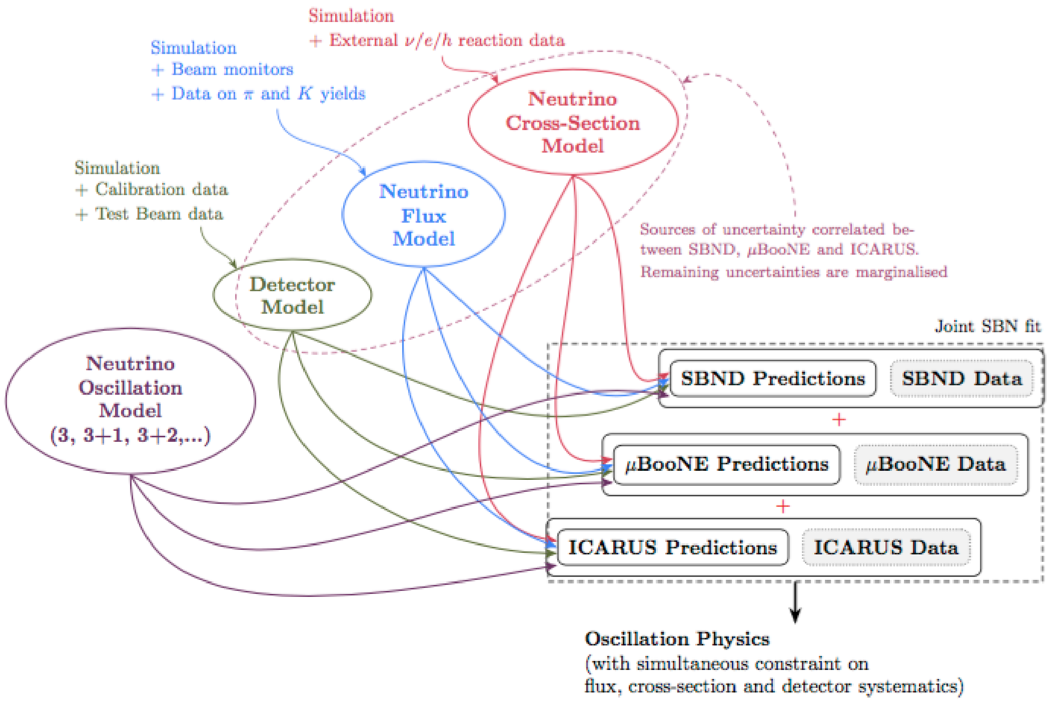

Figure 5.1.: Overview of the SBN oscillation analysis paradigm. A given model for the neutrino oscillation, detector, neutrino flux and neutrino cross-section are combined with the appropriate data to give the prediction for the respective detector. Individual detector predictions may be combined to give an overall SBN prediction.

energy smearing and a series of cuts to try and emulate a fully reconstructed sample. The details of the cuts and smearing that were applied to each of the analyses are discussed in Section 5.3.

Both the events for the ν_μ and ν_e sample were generated using GENIEv3 (specifically the G18_10a_02_11a tune) and then propagated through GEANT4 using the LArSoft framework [81] [93] [94] [82] [85]. For the ν_μ sample, this involved generating $\sim$1,000,000 intrinsic ν_μ events in each detector. The ν_e sample is a little more involved since in addition to generating an intrinsic sample, an oscillated $\nu_\mu \to \nu_e$ sample, a dirt sample and a cosmic sample also needed to be produced. The oscillated sample is used to mimic the ν_e appearance signal whereas the dirt and cosmic samples are backgrounds. The other major background associated with a ν_e analysis involves ν_μ. A dedicated sample was not produced to emulate this, but instead, the events from the ν_μ production were also run through the ν_e

selection. Table 5.1 outlines the number of events produced for the ν_e sample for each sub-sample for each detector. Additionally, the number of events that were selected from each sample are shown for all three detectors. The dirt events were produced with an additional filter at the generation stage which discarded any events where a shower above 10 MeV in the active volume was not present. This filter was used in order to remove any delta rays. Only about 1% of dirt events would pass this filter so the number of dirt events used in the ν_e selection was $\sim$100,000.

Sample	Produced	Selected		
		SBND	MicroBooNE	ICARUS
Intrinsic ν_e	$\sim$1,000,000	$\sim$150,000	$\sim$140,000	$\sim$130,000
Oscillated ν	$\sim$1,000,000	$\sim$180,000	$\sim$150,000	$\sim$140,000
ν_μ	Used ν_μ sample	$\sim$2,000	$\sim$3,000	$\sim$3,000
Dirt	$\sim$10,000,000	$\sim$80	$\sim$100	$\sim$300
Cosmic	$\sim$100,000	$\sim$1	0	$\sim$30

Table 5.1.: The number of events produced and selected for each sub-sample of the ν_e analysis. The same number of events were produced in each of the three SBN detectors.

The actual number of real ν_μ events expected in SBND is well over 5 million for about 3 years of data taking [95]. Generating this many events is not feasible as part of a MC production, hence the above number of events were generated. The MC events produced have an associated Protons-On-Target (POT) so the number of events may be scaled to the nominal POT of each experiment. For SBND and ICARUS the nominal POT is 6.6×10^{20} which corresponds to around 3 years of data taking. Since MicroBooNE has already been collecting data for some time, the nominal POT is 1.32×10^{21}. Due to scaling the generated event rate to the nominal POT this results in non-integer number of events.

5.2. Event Reconstruction

To emulate reconstructed energies, the true energy of particles are smeared. For the ν_μ sample the following conditions are applied. Primary tracks (which is the leading muon in the final state) contained in the active volume, have their true energy smeared by scaling the energy with a Gaussian which has a standard deviation of 0.02. If the primary track is not contained, the energy is instead smeared by a Gaussian with a standard deviation that is given by $-A\ln(BL)$, where L is the track length and $A = 0.102$ and $B = 0.000612$ cm^{-1} [11]. This emulates the multiple scatterings of the track, but in order for the track to have sufficient resolution, a minimum track length of 100 cm is required. Parameters A and B were chosen based on the work of [96]. Non-primary tracks with a true energy of less than 21 MeV are removed (21 MeV is the kinetic energy threshold for reconstructing tracks [11]) and any remaining tracks are smeared with a Gaussian which has a standard deviation of 0.05 [11]. An additional condition that the minimum smeared energy is 0 MeV is applied which ensures that negative energies do not occur.

The values used to determine the degree of energy smearing for the ν_e sample are different to the ν_μ sample. The energy of electron and photon showers are smeared with a Gaussian that has a standard deviation of $0.15/\sqrt{E_{true}}$. Contained muons are smeared with a Gaussian that has a standard deviation of 0.15 whereas the smearing of non-contained muons is not considered. Finally, the hadrons are smeared with a Gaussian that has a standard deviation of 0.05. The same condition ensuring that negative energies are not allowed is again applied. A check is also performed to see if there is more than 50 MeV of hadronic activity at the vertex, which is the threshold for the vertex to be considered visible [11]. Additionally, the reconstruction is assumed to only be sufficiently accurate for showers above 200 MeV, therefore any events with showers that do not exceed this energy threshold are removed.

When reconstructed quantities are considered, background events may mimic the key signature of signal events, resulting in events being misidentified. Some of the most common backgrounds to a CC inclusive sample in SBN will be due to:

- ν_μ sample: Charged pions which may be produced by NC interactions will result in a track that can resemble a muon. Most of the tracks produced by pions will be relatively short at less than 50 cm.
- ν_e sample: Final state neutral pions which are a result of NC interactions decay into two photon showers.
- ν_e sample: If the track length is short (< 1 m) and has a single associated EM shower, ν_μ CC events with a $\mu + \gamma$ in the final state may be mistaken for ν_e CC events with a $\pi + e$ in the final state.
- ν_e sample: Cosmic photons may produce electrons in the TPC via pair production or Compton scattering. The cosmic photons may be produced in the atmospheric shower or by cosmic muons passing through the detector [11].

5.3. Event Selection

The event selections are performed in order to first identify ν_μ or ν_e-like interactions which form a ν_μ or ν_e CC inclusive sample. The selection steps are designed to produce as pure as possible CC inclusive sample by rejecting contributions from other samples such as NC or cosmics, the details of which are outlined below.

5.3.1. ν_μ Selection

The selection criteria for the ν_μ sample are as follows:

1. Remove any events whose interaction vertex is not located in the fiducial volume. The fiducial volume used is outlined in Table B.1.
2. If no muon or charged pion track are produced, remove the event.
3. If the primary track has a length less than 50 cm and is fully contained in the detector, remove the event.
4. If the primary track exits the detector and has a length less than 100 cm, remove the event.

5. A weight of 0.8 is applied to all selected events to account for an assumed 80% reconstruction efficiency [11].

5.3.2. ν_e Selection

The ν_e selection follows a similar basis to the ν_μ selection described in section 5.3.1, however, different criteria for the selection were applied to beam induced TPC events, dirt events and cosmic events, each of which are outlined below.

Beam induced active volume events

1. Remove any events whose interaction vertex is not located in the fiducial volume. The fiducial volume used is outlined in Table B.1.
2. If more than one shower arising from the vertex has an energy above a 100 MeV, the event is removed.
3. If there is only one photon candidate in the event, a conversion gap cut is applied rejecting any event where the photon shower occurs more than 3 cm from the vertex.
4. A weight of 0.06 is applied to the remaining photons which undergo a dE/dx cut resulting in a 94% background rejection.
5. If a misidentified photon originates from a resonant ν_μ CC interaction, the muon lepton is identified. Events where a muon travels greater than 1 m are assumed to be from ν_μ CC interactions and the event is removed.
6. A weight of 0.8 is applied to all selected events to account for an assumed 80% reconstruction efficiency [97].

Dirt Events

The selection procedure for dirt events is similar to that of beam induced events outlined above. However, since the vertex for dirt events occurs outside the detector volume, the conversion gap and muon track length cuts are not undertaken [97].

Cosmic Events

A largely separate analysis is applied for cosmic events which is as follows:

1. If a cosmic photon initially interacts outside the fiducial volume the event is removed.
2. Cosmic events which occur outside the beam spill time window are removed if there is no other activity in the TPC during the beam spill time.
3. 95% of cosmic events occurring within the beam spill window are removed by use of the PDS and CRT systems and taking advantage of the bucket structure of the beam.
4. Same dE/dx cut as described above.
5. A topological cosmic cylinder cut is applied to cosmic photons which originate from cosmic muons that pass through the TPC. These can be removed by a fiducial volume cut corresponding to a cylinder of radius 15 cm around the cosmic muon [97].

5.4. Reaction Modes

The reaction modes define the topology of neutrino interactions. Categorising neutrino events is a requirement for handling systematic uncertainties since these are reaction mode dependent. The reaction modes are grouped into two sets[1]: the *fine* reaction modes which outline the complete list of all possible reaction modes and the *coarse* reaction modes which define a broader class of interaction which encompass one or more fine reaction mode. The fine reaction modes are listed in Table 5.2 and are typically used at the analysis level. The coarse reaction modes used depend on the analysis channel and are listed in Table 5.4. They are usually only used when displaying data such as in a breakdown of event rate spectra since using the complete list of reaction modes would be impractical.

[1]The CC QE 0π mode is sometimes simply written as CC QE.

	Fine Reaction Modes	
ν_μ, $\bar{\nu}_\mu$	ν_e, $\bar{\nu}_e$	$\nu_\mu \rightarrow \nu_e, \bar{\nu}_\mu \rightarrow \bar{\nu}_e$
CC QE 0π	CC QE 0π	CC QE 0π
NC Elastic	NC Elastic	CC 2p2h
CC, NC 2p2h	CC, NC 2p2h	CC $1\pi^\pm$
CC, NC $1\pi^\pm$	CC, NC $1\pi^\pm$	CC $1\pi^0$
CC, NC $1\pi^0$	CC, NC $1\pi^0$	CC $2\pi^\pm$
CC, NC $2\pi^\pm$	CC, NC $2\pi^\pm$	CC $2\pi^0$
CC, NC $2\pi^0$	CC, NC $2\pi^0$	CC Coh
CC, NC $\pi^\pm\pi^0$	CC, NC $\pi^\pm\pi^0$	Elastic Scattering
CC, NC Coh	CC, NC Coh	CC Other
CC, NC Elastic Scattering	CC+NC Elastic Scattering	
NC 1γ	NC 1γ	
CC, NC Other	CC, NC Other	
	Cosmic & Dirt	

Table 5.2.: The complete list of reaction modes considered in an SBN analysis. The 2p2h mode is defined as having a charged lepton + 2 nucleon topology distinguishing it from the other topologies.

Coarse Reaction Modes	
ν_μ, $\bar{\nu}_\mu$	ν_e, $\bar{\nu}_e$
ν_μ CC QE 0π	ν_e CC QE 0π
ν_μ CC 2p2h	ν_e CC 2p2h
ν_μ CC 1π	ν_e CC 1π
ν_μ CC 2π	ν_e CC 2π
ν_μ CC Other	ν_e CC Other
$\bar{\nu}_\mu$ CC	$\bar{\nu}_e$ CC
ν_e & $\bar{\nu}_e$ CC	ν_μ CC
NC	$\bar{\nu}_\mu$ CC
Cosmic	Oscillated ν_e CC
Dirt	NC 0π
	NC Other
	Cosmic
	Dirt

Table 5.3.: The *coarse* reaction modes used for both the ν_μ and ν_e channels. These are a broader definition of the reaction modes where one or more of the *fine* reaction modes listed in Table 5.2 would come under the umbrella of a given coarse reaction mode.

5.5. Systematic Uncertainties

A number of uncertainties associated with the neutrino flux, neutrino interactions and detector effects have to be considered. Within the simulation, predictions on the event rate and the properties of an event are required to reflect changes in these uncertainty parameters.

The majority of flux and interaction systematic parameters considered are implemented using well validated reweighting schemes provided by MicroBooNE and GENIE respectively (the two exceptions are the POT normalisation and 2p2h uncertainty) [64] [98]. For each MC event and systematic parameter included in the reweight schemes, *universes* are simulated where the given parameter is randomly varied within its limits. Each universe will therefore have a single parameter which is tweaked from its nominal value and for each parameter, 500 universes are simulated each with a different tweaked value for the parameter. This allows changes in event rate spectra to be related to systematic parameter variations. The systematic parameters considered are described below along with a table quoting their estimated uncertainty.

Currently, uncertainties due to detector effects remain largely unconstrained and therefore a dedicated package describing their effects does not exist. They are instead handled internally and are described in Section 5.5.3.

5.5.1. Flux Systematics

The flux systematics are grouped into 3 distinct sets with different origins as part of the MicroBooNE reweight scheme which are detailed below plus the additional POT normalisation.

Optical Flux Systematics

The optical flux systematics are comprised of two parameters: the *skin effect* and the *horn current*. The horn current parameter is simply the uncertainty of the supplied current to the focusing horn. Since the current is linked to the focusing properties of the horn, uncertainty on the current leads to an uncertainty on the neutrino flux. The focusing horn is surrounded by a conductor where currents travel on the surface of the conductor. The skin effect is a measure of how much these surface currents penetrate into the conductor which in turn affects the internal fields of the conductor. Therefore, due to the skin effect, the strength of the magnetic field that particles propagating through the horn experience may vary [64].

Parameter	Description	Uncertainty
$f_{SkinEffect}$	Depth that the current penetrates the horn conductor	$< 18\%$
$f_{HornCurrent}$	Current running in the horn conductor	$\pm 0.6\%$

Table 5.4.: Optical systematic flux uncertainties associated with the current in the horn [64].

Secondary Hadron Interaction Cross-Sections

The proton interaction rate in the BNB target is largely dependent on the hadronic cross-sections with the beryllium target and aluminium horn. The total cross-section, σ_{TOT}, is defined as the sum of the elastic, σ_{EL} and inelastic, σ_{INEL}, cross-sections, with the quasi-elastic cross-section, σ_{QE}, being a subset of the σ_{INEL} cross-section. The σ_{TOT} variations are based on comparing calculations with neutron-nucleus measurements. The model describing σ_{TOT} is assumed to work sufficiently well for $\pi^{\pm}$-nucleus interactions and is extended to include these interactions in addition to all nucleon-nucleus interactions. σ_{INEL} is estimated directly from the available data and the deviations are therefore noticeably smaller than for σ_{TOT}. σ_{QE} variations are again estimated from a combination of the available data and models [64].

The above approach is applied for both beryllium and aluminium nuclei and the uncertainty associated with the total, quasi-elastic and inelastic cross-sections for both nucleons and pions for the two nuclei are shown in Table 5.5.

Parameter	Description	Uncertainty	
		Be	Al
$f_{\sigma^N_{INEL}}$	Secondary inelastic nucleon cross-section in the target (Be) and horn (Al)	$\pm 5\%$	$\pm 10\%$
$f_{\sigma^N_{QE}}$	Secondary quasi-elastic nucleon cross-section in the target (Be) and horn (Al)	$\pm 20\%$	$\pm 45\%$
$f_{\sigma^N_{TOT}}$	Secondary total nucleon cross-section in the target (Be) and horn (Al)	$\pm 15\%$	$\pm 25\%$
$f_{\sigma^\pi_{INEL}}$	Secondary inelastic pion cross-section in the target (Be) and horn (Al)	$\pm 10\%$	$\pm 20\%$
$f_{\sigma^\pi_{QE}}$	Secondary quasi-elastic pion cross-section in the target (Be) and horn (Al)	$\pm 11.2\%$	$\pm 25.9\%$
$f_{\sigma^\pi_{TOT}}$	Secondary total pion cross-section in the target (Be) and horn (Al)	$\pm 11.9\%$	$\pm 28.7\%$

Table 5.5.: The systematic uncertainties associated with secondary hadron interaction cross-sections in both the horn (Aluminium) and the target (Beryllium) [11].

Hadronic Neutrino Production Flux Uncertainties

The neutrinos in the BNB are due to decaying particles which are a result of protons interacting with the beryllium target. Understanding the neutrino flux, therefore, relies on understanding the production of the particles decaying to neutrinos, which are predominately pions for ν_μ and kaons for ν_e (plus the decay of muons which in turn are produced in the meson decays).

The Sanford-Wang parameterisation is used to estimate the $\pi^\pm$ production. It depends on the meson momentum, p, and angle relative to the incident proton, θ, and also the proton momentum, p_B. The parametrisation is given by

$$\frac{d^2\sigma}{dpd\theta} = c_1 p^{c_2}\left(1 - \frac{p}{p_B - c_9}\right)\exp\left(-c_3\frac{p^{c_4}}{p_B^{c_5}} - c_6\theta(p - p_B c_7 \cos^{c_8}\theta)\right), \qquad (5.1)$$

where parameters $c_{1\to 9}$ are determined from the HARP (8.89 GeV/c), BNL E910 (6.4 GeV/c) and BNL E910 (12.3 GeV/c) experiments. The uncertainties associated with the parametrisation are one of the driving factors in the uncertainty on the meson production [64].

No K^+ production rates exist for proton-beryllium interactions at 8.89 GeV/c which is the primary BNB operating momentum. To estimate the K^+ production rate at the BNB momentum, Feynman scaling is used to extrapolate the rate from production rates at nearby energies [64].

The major contribution that the K^0 makes to the BNB flux is from the decay of the K_L^0. The K^0 that are produced via strong interactions have equal contents of K_L^0 and K_s^0, therefore the production rate of K_L^0 can be inferred from knowing the production rate of K_s^0. The Sanford-Wang parametrisation is again used to estimate the production cross-section by combining data from the BNL E910 experiment at 12.3 GeV/c and 17.5 GeV/c and the KEK experiment at 12.3 GeV/c.

For the K^-, there is minimal production data available, therefore, simulations are used exclusively. The rate and spectrum of the K^- are estimated by simulating 8.89 GeV/c proton-beryllium interactions [64].

Parameter	ν production	Uncertainty			
		ν_μ	$\bar{\nu}_\mu$	ν_e	$\bar{\nu}_e$
f_{π^+}	Mechanism: π^+	$\pm$ 11.7%	$\pm$ 1.0%	$\pm$ 10.7%	$\pm$ 0.03%
f_{π^-}	Mechanism: π^-	$\pm$ 0.0%	$\pm$ 11.6%	$\pm$ 0.0%	$\pm$ 3.0%
f_{K^+}	Mechanism: K^+	$\pm$ 0.2%	$\pm$ 0.1%	$\pm$ 2.0%	$\pm$ 0.1%
f_{K^-}	Mechanism: K^-	$\pm$ 0.0%	$\pm$ 0.4%	$\pm$ 0.0%	$\pm$ 3.0%
f_{K^0}	Mechanism: K^0	$\pm$ 0.0%	$\pm$ 0.3%	$\pm$ 2.3%	$\pm$ 21.4%

Table 5.6.: Hadronic neutrino production systematic flux uncertainties [99].

BNB POT Normalisation

The intensity of the proton beam is monitored by two toroids and it has been found that the two toroids agree with one another to within 2% [64]. An additional 2% normalisation uncertainty is applied in order to account for this POT accounting uncertainty. This uncertainty is set so that it is fully correlated between all analysis bins.

5.5.2. Interaction Systematics

The uncertainties associated with neutrino interactions are provided by GENIE and are implemented using the GENIE ReWeight package. This is the case for all the interaction systematics considered here except for the 2p2h systematic which is described below. The GENIE reweighting scheme works as follows; for each quantity, P, which has an associated uncertainty, a systematic parameter, x_P is introduced. Varying x_P will modify, P such that

$$P \rightarrow P' = P(1 + x_P.\frac{\delta P}{P}), \tag{5.2}$$

where δP represents the standard deviation of P. It follows from Equation 5.2 that for a $x_P = 0$, $P' = P$ and for $x_P = \pm 1$, $P' = P \pm \delta P$.

The two main types of interaction systematics considered in this analysis are cross-section and intranuclear hadron transport model uncertainties, however, within an SBN analysis, the interaction systematics are generally grouped into two categories: the *propsal* and *modern* set of parameters. The proposal systematics are those that were included as part of the analysis done at the time of the SBN proposal, whereas the modern systematics represent the additional systematics which have been deemed relevant for SBN in the period following the proposal [11]. The details of how GENIE handles cross-section and intranuclear hadron transport parameters is detailed below, followed by outlining which parameters are included as part of the proposal and modern set of parameters.

Neutrino Cross-Section uncertainties

The neutrino cross-section gives a measure of the neutrino interaction probability. The event weight, w_σ^{evt}, associated with a given parameter for a neutrino cross-section is calculated via

$$w_\sigma^{evt} = \left(\frac{d^n \sigma'_\nu}{dK^n} \right) \bigg/ \left(\frac{d^n \sigma_\nu}{dK^n} \right), \tag{5.3}$$

where $\frac{d^n \sigma'_\nu}{dK^n}$ is the differential cross-section with varied physics parameters and $\frac{d^n \sigma_\nu}{dK^n}$ is the nominal differential cross-section with K^n being the kinematical phase space in both cases [98].

Intranuclear hadron transport uncertainties

When hadrons are produced in the nucleus they may interact as they propagate out of the nucleus. The reinteraction in the nucleus may significantly alter the observed final state particles. There are two primary uncertainties considered with this effect: the uncertainty in the overall probability of rescattering and the uncertainty corresponding to the probability of each rescattering mode once it has been determined that rescattering will occur for a given hadron [98].

For a hadron propagating in the nucleus, the survival probability, P_{surv}^h, is calculated as

$$P_{surv}^h = \int e^{-r/\lambda^h(\vec{r},h,E_h)} dr, \tag{5.4}$$

where the integral is evaluated along the path the hadron takes in the nucleus and λ^h is the mean free path. The probability of rescattering, P_{rescat}^h, is then defined as

$$P_{rescat}^h = 1 - P_{surv}^h. \tag{5.5}$$

The mean free path is a function of the hadron type, h, the hadron energy, E_h and position, $\vec{r}$ and is given by

$$\lambda^h = \frac{1}{\rho_{nucl}(r) \cdot \sigma^{hN}(E_h)}, \tag{5.6}$$

where $\rho_{nucl}(r)$ is the density profile of the nucleus and $\sigma^{hN}(E_h)$ is the total cross-section of the hadron-nucleon [98].

In terms of reweighting, for a given systematic parameter, x^h_{mfp}, with an uncertainty, $\delta\lambda^h$, the mean free path may be tweaked such that

$$\lambda^h \rightarrow \lambda^{h\prime} = \lambda^h \left(1 + x^h_{mfp}\frac{\delta\lambda^h}{\lambda^h}\right), \tag{5.7}$$

where $\lambda^{h\prime}$ is the tweaked mean free path. The modified survival probability, $P^{h\prime}_{surv}$, is then found by substituting $\lambda^{h\prime}$ into Equation 5.4. The weight, w^h_{mfp}, associated with a given change in the mean free path is calculated as [98]

$$w^h_{mfp} = \begin{cases} \frac{1-P^{h\prime}_{surv}}{1-P^h_{surv}}, & \text{if h reinteracts} \\ \frac{P^{h\prime}_{surv}}{P^h_{surv}}, & \text{if h escapes.} \end{cases} \tag{5.8}$$

Once it has been determined that a hadron will rescatter, the following scattering modes are considered: elastic, inelastic, charge exchange, absorption and pion production. The probability of a given mode, P^h_f, occurring is given by

$$P^h_f = \frac{\sigma^{hA}_f}{\sigma^{hA}_{total}}, \tag{5.9}$$

where σ^{hA}_f is the cross-section for the given hadron-nucleus mode and σ^{hA}_{total} is the total hadron-nucleus cross-section. Similarly to the mean free path, the hadron-nucleus cross-section of a mode may be tweaked such that

$$\sigma^{hA}_f \rightarrow \sigma^{hA\prime}_f = \sigma^{hA}_f \left(1 + x^h_f\frac{\delta\sigma^{hA}_f}{\sigma^{hA}_f}\right), \tag{5.10}$$

where $\sigma_f^{hA\prime}$ is the tweaked cross-section, x_f^h is a systematic parameter and $\delta\sigma_f^{hA}$ is the associated uncertainty. The weight of a mode, w_{mode}^h, is given by

$$w_{mode}^h = \sum_f \delta_{ff'} \cdot x_f^h \cdot \frac{\delta\sigma_f^{hA}}{\sigma_f^{hA}}, \tag{5.11}$$

where the sum is over the possible rescattering modes, f' is the actual mode for the given hadron, and $\delta_{ff'}$ is the Kronecker delta between f and f' [98].

The total weight of a single hadron, w^h, is then given by the product of the two weights such that,

$$w^h = w_{mfp}^h \cdot w_{mode}^h. \tag{5.12}$$

For a single neutrino event, there may be multiple hadrons present, therefore the total weight, w_{HT}^{evt}, for a neutrino event is given by the product of individual hadron weights,

$$w_{HT}^{evt} = \prod_j w_j^h, \tag{5.13}$$

where the index j corresponds to all the primary hadrons [98].

Proposal Interaction Systematics

The proposal systematics only included a set of cross-section parameters which are listed in Table 5.7 along with their uncertainty.

Parameter	Description	$\delta P/P$
$f_{M_A^{CCQE}}$	Axial mass for CC quasi-elastic	-15% +25%
$f_{M_A^{CCRes}}$	Axial mass for CC resonance neutrino production	$\pm$ 20%
$f_{M_A^{NCRes}}$	Axial mass for NC resonance neutrino production	$\pm$ 20%
f_{NC}	Additional error on NC/CC ratio	$\pm$ 25%
$f_{nR_{\nu n}^{CC1\pi}}$	Non-Res bkg normalisation in νn CC1π reactions	$\pm$ 50%
$f_{nR_{\nu p}^{CC1\pi}}$	Non-Res bkg normalisation in νp CC1π reactions	$\pm$ 50%
$f_{nR_{\nu n}^{CC2\pi}}$	Non-Res bkg normalisation in νn CC2π reactions	$\pm$ 50%
$f_{nR_{\nu p}^{CC2\pi}}$	Non-Res bkg normalisation in νp CC2π reactions	$\pm$ 50%
$f_{nR_{\bar{\nu} n}^{CC1\pi}}$	Non-Res bkg normalisation in $\bar{\nu} n$ CC1π reactions	$\pm$ 50%
$f_{nR_{\bar{\nu} p}^{CC1\pi}}$	Non-Res bkg normalisation in $\bar{\nu} p$ CC1π reactions	$\pm$ 50%
$f_{nR_{\bar{\nu} n}^{CC2\pi}}$	Non-Res bkg normalisation in $\bar{\nu} n$ CC2π reactions	$\pm$ 50%
$f_{nR_{\bar{\nu} p}^{CC2\pi}}$	Non-Res bkg normalisation in $\bar{\nu} p$ CC2π reactions	$\pm$ 50%
$f_{nR_{\nu n}^{NC1\pi}}$	Non-Res bkg normalisation in νn NC1π reactions	$\pm$ 50%
$f_{nR_{\nu p}^{NC1\pi}}$	Non-Res bkg normalisation in νp NC1π reactions	$\pm$ 50%
$f_{nR_{\nu n}^{NC2\pi}}$	Non-Res bkg normalisation in νn NC2π reactions	$\pm$ 50%
$f_{nR_{\nu p}^{NC2\pi}}$	Non-Res bkg normalisation in νp NC2π reactions	$\pm$ 50%
$f_{nR_{\bar{\nu} n}^{NC1\pi}}$	Non-Res bkg normalisation in $\bar{\nu} n$ NC1π reactions	$\pm$ 50%
$f_{nR_{\bar{\nu} p}^{NC1\pi}}$	Non-Res bkg normalisation in $\bar{\nu} p$ NC1π reactions	$\pm$ 50%
$f_{nR_{\bar{\nu} n}^{NC2\pi}}$	Non-Res bkg normalisation in $\bar{\nu} n$ NC2π reactions	$\pm$ 50%
$f_{nR_{\bar{\nu} p}^{NC2\pi}}$	Non-Res bkg normalisation in $\bar{\nu} p$ NC2π reactions	$\pm$ 50%

Table 5.7.: GENIE interaction cross-section systematics considered in SBN as part of the proposal set of systematics. [98].

Modern Interaction Systematics

The modern systematics include an additonal set of cross-section parameters which are listed in Table 5.8 in addition to a set of intranuclear hadron transport parameters which are listed in Table 5.9. Again, both tables also show the associated uncertainty of each parameter. The 2p2h uncertainty mentioned is also considered as part of the modern systematic parameters and is detailed below.

Parameter	Description	$\delta P/P$
$f_{M_A^{NCEl}}$	Axial mass for NC elastic	$\pm 25\%$
$f_{\eta^{NCEl}}$	Strange axial form factor for NC elastic	$\pm 30\%$
$f_{M_V^{CCRes}}$	Vector mass for CC resonance neutrino production	$\pm 10\%$
$f_{M_V^{NCRes}}$	Vector mass for NC resonance neutrino production	$\pm 10\%$
$f_{A_{HT}}$	Higher-twist parameter A for NC and CC DIS events	$\pm 25\%$
$f_{B_{HT}}$	Higher-twist parameter B for NC and CC DIS events	$\pm 25\%$
$f_{C_{v1u}}$	Valence p.d.f. correction factor C_{v1u} for DIS events	$\pm 30\%$
$f_{C_{v2u}}$	Valence p.d.f. correction factor C_{v2u} for DIS events	$\pm 40\%$
$f_{M_A^{Coh}}$	Axial mass for NC and CC coherent pion production	$\pm 50\%$
$f_{R_0^{Coh}}$	Nuclear size parameter controlling π absorption	$\pm 20\%$
$f_{\Delta \to N\gamma}$	Branching ratio for Δ radiative decay	$\pm 50\%$

Table 5.8.: GENIE interaction cross-section systematics considered in SBN as part of the modern set of systematics [98].

Parameter	Description	$\delta P/P$
f_{λ_π}	Mean free path for pions	$\pm\,20\%$
$f_{R_\pi^{CEx}}$	Charge exchange rescattering fraction for pions	$\pm\,50\%$
$f_{R_\pi^{Inel}}$	Inelastic rescattering fraction for pions	$\pm\,40\%$
$f_{R_\pi^{\pi}}$	Pion-production rescattering fraction for pions	$\pm\,20\%$
$f_{R_\pi^{Abs}}$	Absorption fraction for pions	$\pm\,20\%$
f_{λ_N}	Mean free path for nucleons	$\pm\,20\%$
$f_{R_N^{CEx}}$	Charge exchange rescattering fraction for nucleons	$\pm\,50\%$
$f_{R_N^{Inel}}$	Inelastic rescattering fraction for nucleons	$\pm\,40\%$
$f_{R_N^{\pi}}$	Pion-production rescattering fraction for nucleons	$\pm\,20\%$
$f_{R_N^{Abs}}$	Absorption fraction for nucleons	$\pm\,20\%$

Table 5.9.: Intranuclear hadron transport systematic parameters considered in SBN as part of the modern set of systematics [98].

2p2h uncertainty

A 2p2h uncertainty parameter which specifically affects 2p2h events is not included from the GENIE event generator since it was decided that the parameter was not sufficiently validated. Instead, a 100% normalisation uncertainty is applied to all 2p2h events. The value of the uncertainty was chosen to be a 100% (maximal) to ensure the effect of the 2p2h parameter would not be an underestimate.

5.5.3. Efficiency Systematics

Efficiency systematics are not implemented in the *standard* analyses because there currently is not a good handle on how to correctly quantify them. A rigorous scheme akin to those described in Section 5.5.1 and Section 5.5.2 does not exist, so instead in-house methods have been developed which are described below.

The current scheme for implementing efficiency (detector) systematics into a fit is by use of a covariance matrix where each element is defined by the systematics outlined in Table 5.10. This allows for the lack of associated event reweighting schemes to be bypassed whilst still being able to capture varying uncertainties being applied to different kinematic ranges, detectors and signal or background processes in each sample. In general, it is assumed that a covariance matrix $\mathcal{M}_{ij}$ is comprised of both correlated and uncorrelated uncertainties such that

$$\mathcal{M}_{ij} = \mathcal{M}_{ij}^{corr} + \mathcal{M}_{ij}^{uncorr}, \tag{5.14}$$

where $\mathcal{M}_{ij}^{corr}$ is the correlated component and $\mathcal{M}_{ij}^{uncorr}$ is the uncorrelated component. For correlated uncertainties,

$$\mathcal{M}_{ij}^{corr} = \begin{cases} \sigma_i^2, & i = j \\ C_{ij}\sigma_i\sigma_j, & i \neq j, \end{cases} \tag{5.15}$$

where C_{ij} represents the correlation between the off-diagonal elements and $\sigma_{i,j}$ is some percentage error associated with each systematic. In the case of fully correlated uncertainties, C_{ij} reduces to one and $\sigma_i = \sigma_j$. For uncorrelated uncertainties,

$$\mathcal{M}_{ij}^{uncorr} = \begin{cases} \sigma_i'^2, & i = j \\ 0, & i \neq j, \end{cases} \tag{5.16}$$

with σ_i' again being a percentage error. If any correlated errors are assumed to by fully correlated, $\mathcal{M}_{ij}$ will then have diagonal elements given by $\sigma_i^2 + \sigma_i'^2$ and off diagonal elements given by σ_i^2.

					Applies to
Systematic	**Beam**	**Detector**	**Sample**	**Mode**	**Reco. energy bin edges**
$f_0 - f_7$	FHC	SBND	ν_μCC-like	signal/ν_μCC	{0, 0.2, 0.4, 0.6, 0.8, 1.0, 1.5, 2.0, ∞}
$f_8 - f_{13}$	FHC	SBND	ν_μCC-like	bkg/NC	{0, 0.2, 0.4, 0.6, 0.8, 1.0, ∞}
f_{14}	FHC	SBND	ν_μCC-like	bkg/Dirt	{0, ∞}
f_{15}	FHC	SBND	ν_μCC-like	bkg/Cosmics	{0, ∞}
$f_{16} - f_{24}$	FHC	SBND	ν_eCC-like	signal/ν_eCC	{0, 0.2, 0.4, 0.6, 0.8, 1.0, 1.5, 2.0, 3.0, ∞}
$f_{25} - f_{33}$	FHC	SBND	ν_eCC-like	bkg/ν_μCC	{0, 0.2, 0.4, 0.6, 0.8, 1.0, 1.5, 2.0, 3.0, ∞}
$f_{34} - f_{42}$	FHC	SBND	ν_eCC-like	bkg/NC1γ	{0, 0.2, 0.4, 0.6, 0.8, 1.0, 1.5, 2.0, 3.0, ∞}
$f_{43} - f_51$	FHC	SBND	ν_eCC-like	bkg/NC1π^0	{0, 0.2, 0.4, 0.6, 0.8, 1.0, 1.5, 2.0, 3.0, ∞}
$f_{52} - f_{60}$	FHC	SBND	ν_eCC-like	bkg/NCother	{0, 0.2, 0.4, 0.6, 0.8, 1.0, 1.5, 2.0, 3.0, ∞}
$f_{61} - f_{66}$	FHC	SBND	ν_eCC-like	bkg/Dirt	{0, 0.2, 0.4, 0.6, 0.8, 1.0, ∞}
$f_{67} - f_{72}$	FHC	SBND	ν_eCC-like	bkg/Cosmics	{0, 0.2, 0.4, 0.6, 0.8, 1.0, ∞}
$f_{73} - f_{145}$	As above, but for μB				
$f_{146} - f_{218}$	As above, but for ICARUS				

Table 5.10.: The binning scheme used to produce the efficiency uncertainty covariance matrices.

All future discussion involving correlated uncertainties should from here on be assumed to be fully correlated even if not explicitly stated. A set of example covariance matrices are shown in Figure 5.2. The top left plot corresponds to a 10% correlated error only. The remaining three plots all have a correlated error of 2%, with some varying amounts of an uncorrelated error associated with each systematic.

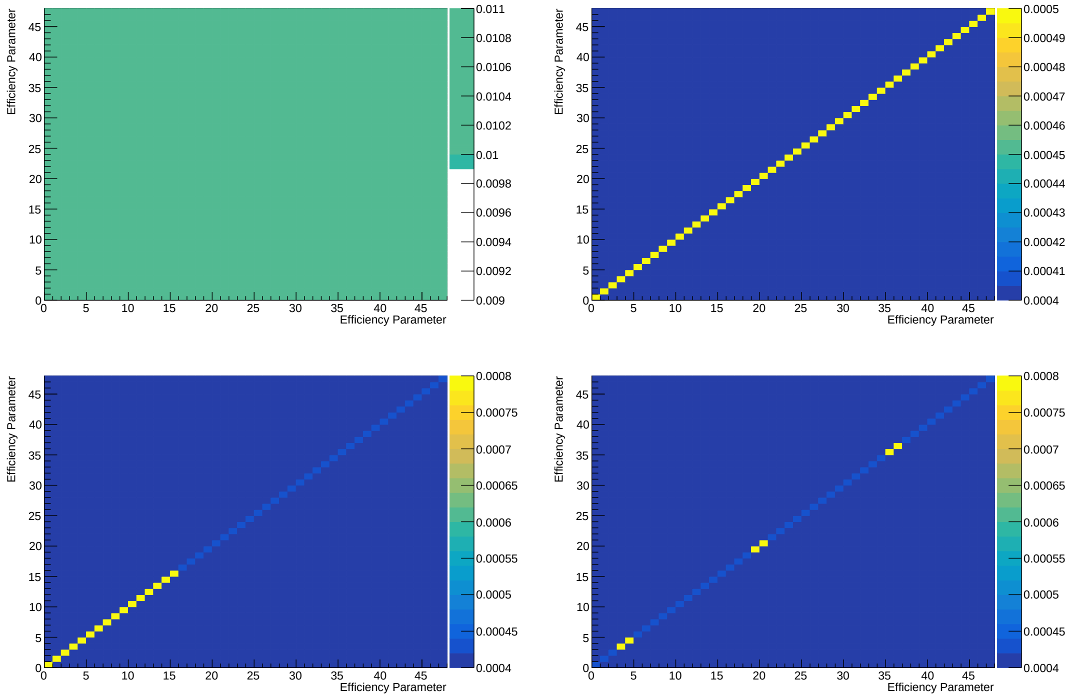

Figure 5.2.: Covariance matrices produced to investigate the effects of efficiency systematics for the ν_μ disappearance channel. Top left: A 10% fully correlated error only. Top right: A 2% fully correlated error with an additional 1% uncorrelated error across all bins. Bottom left: A 2% fully correlated error with an additional 2% uncorrelated error for all SBND bins and a 0.5% uncorrelated error for all MicroBooNE and ICARUS bins. Bottom right: A 2% fully correlated error with and additional 2% uncorrelated error for the peak energy bins (0.6 - 1.0 GeV) in each detector and a 0.5% uncorrelated error for all other bins.

5.6. Other Analysis Choices

Two other key analysis choices are the neutrino baseline parameterisation and the binning scheme used for the kinematic variable. As is shown in Equation 2.38, the baseline is one of the components that drives the oscillation probability and therefore any approximations to the true baseline must be chosen such that the impact to the oscillation probability is negligible. The kinematic variable used in this analysis is the energy of the neutrino for both true and reconstructed quantities.

5.6.1. Baseline

For long baseline experiments, it is not uncommon for fitting frameworks to simply use some average value for the baseline since factors such as the interaction point in the detector or the position at which a particle decays into a neutrino would only change the average baseline for the experiment by a negligible amount. However, for short baseline experiments such as SBN, these factors may change the baseline significantly, up to around 20% in SBND.

In an attempt to minimise computing resources, the true baseline was not initially used, but instead, several approximations to the baseline were tried. To begin with, the average baseline of each SBN detector was used for all neutrino energies. This was calculated from the true baseline distribution of ν_μ events in each detector which are shown in Figure 5.3. Secondly, a 4-knot spline (named spline V1) for each detector was defined in order to try and better approximate the baseline. This method was improved upon by producing a spline for each of the true energy bins (named spline V2) which are defined in Section 5.6.2. In order to establish the impact of any baseline approximations on the oscillation probability, the oscillation probability was plotted as a function of true neutrino energy with the oscillation parameters $\sin^2 2\theta_{\mu\mu} = 0.01$ and $\Delta m^2_{41} = 50$ eV^2. This oscillation point was chosen to ensure that a region where rapid oscillations occur was being investigated, which would highlight the effect of any baseline choices. The oscillation probabilities as a function of energy are shown in Figure 5.7 for the four different baselines described. It was eventually decided that any approximation would be insufficient and that the true baseline should be used.

The studies of the baseline approximations were done in the context of the ν_μ disappearance channel. In principle, within the ν_e sample, different approximations should be applied to the different sub-samples since the baseline distribution is not the same for all the sub-samples. For example, the ν_μ's in the oscillated and ν_μ sub-samples will both mainly be the result of pion decays whereas the ν_e's in the intrinsic sub-sample will have a larger contribution from kaon and secondary muon decays. Pions and kaons have different lifetimes which coupled with the contribution from the decay of secondary particles means that the baseline distribution of the oscillated and ν_μ sub-sample will be different to that of the intrinsic ν_e sub-sample. This was never done since it was decided that the true baseline should be used. The baseline distributions for the intrinsic ν_e, oscillated ν and the overall ν_e sample from combining all the sub-samples together are shown in Figure 5.4, Figure 5.5 and Figure 5.6 respectively for each of the SBN detectors. It should be noted that the baseline distributions for oscillated ν_e sample from Figure 5.5 and the ν_μ sample from Figure 5.3 are comparable. This is due to the initial parameters describing the oscillated sample being the same as for the ν_μ sample. The only difference being the neutrino oscillations from ν_μ to ν_e which is not something that affects the baseline.

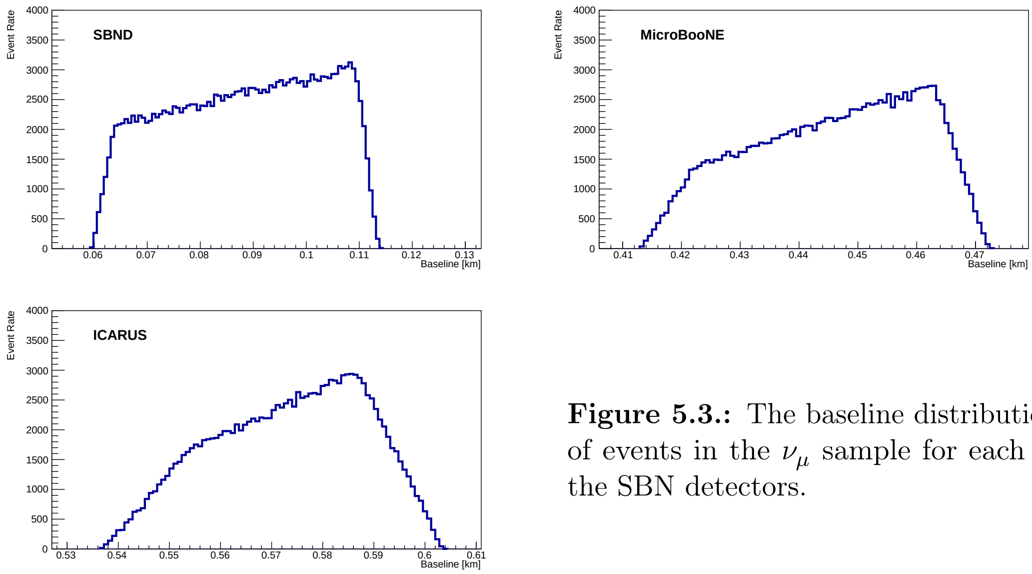

Figure 5.3.: The baseline distribution of events in the ν_μ sample for each of the SBN detectors.

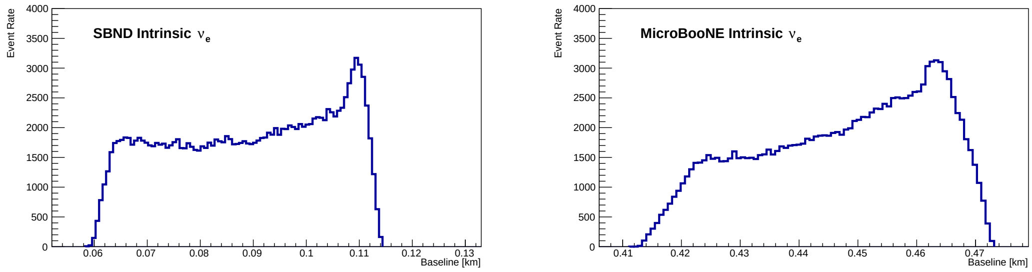

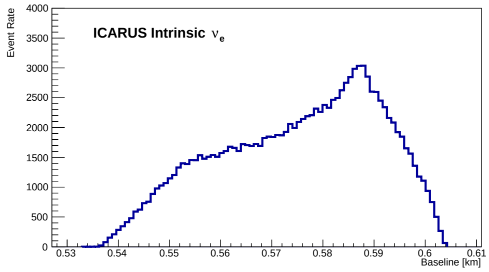

Figure 5.4.: The baseline distribution of events in the intrinsic ν_e sample for each of the SBN detectors.

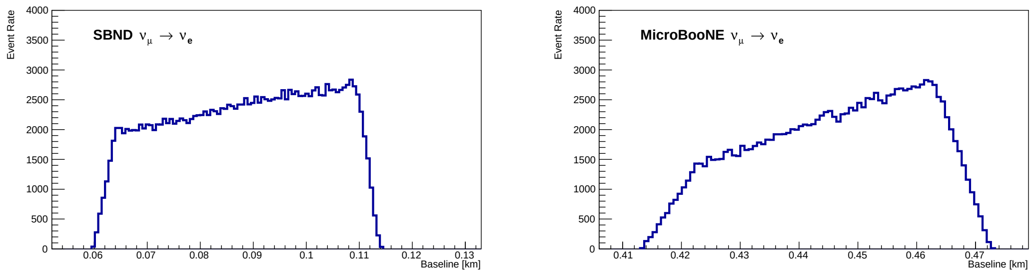

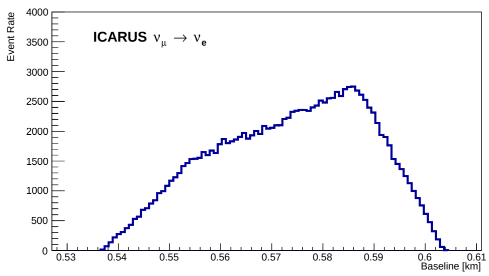

Figure 5.5.: The baseline distribution of events in the oscillated $\nu_\mu \to \nu_e$ sample for each of the SBN detectors.

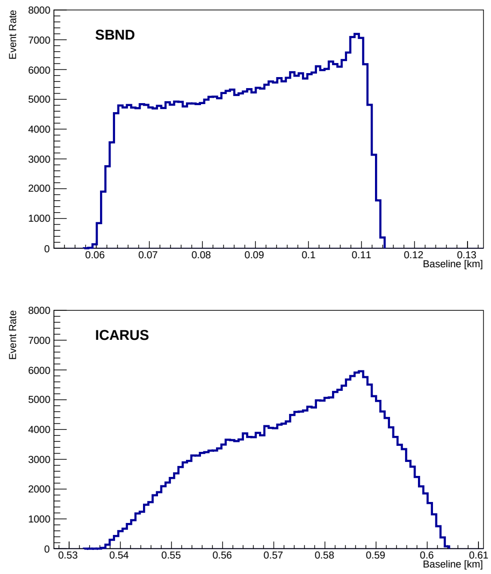

Figure 5.6.: The baseline distribution of events in the overall ν_e sample which is comprised of events from the intrinsic ν_e, oscillated ν, the ν_μ events from passing the ν_e selection and the dirt and cosmic samples (which are not explicitly shown) for each of the SBN detectors.

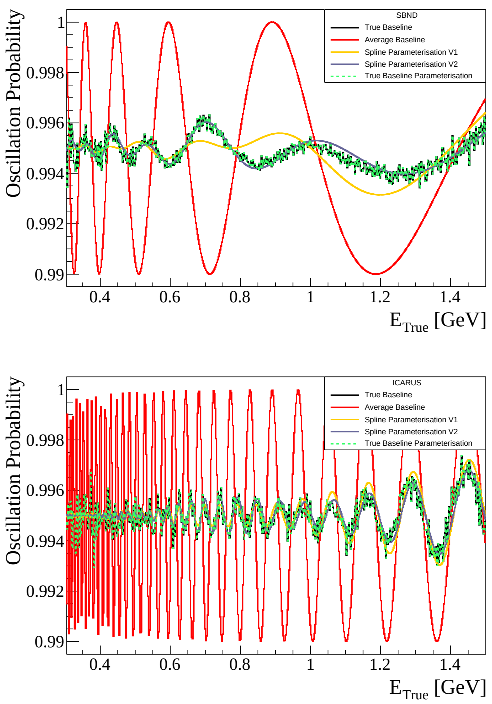

Figure 5.7.: The oscillation probability as a function of true neutrino energy for the ν_μ disappearance sample with oscillation parameters $\sin^2 2\theta_{\mu\mu} = 0.01$ and $\Delta m^2_{41} = 50\ \mathrm{eV}^2$ in each SBN detector. The results from using each baseline parametrisation are shown.

5.6.2. Binning

The energy binning schemes used are the same across each of the three detectors, however, the scheme used is different for the ν_μ and ν_e analyses. Furthermore, there are separate schemes for both the true and reconstructed energies. Each of the binning schemes is outlined below.

The ν_μ edge-to-edge binning has 21 bins in reconstructed neutrino energy which are bounded as follows:

- 1 bin from 0.00-0.20 GeV,
- 2 0.10-GeV bins from 0.20-0.40 GeV,
- 12 0.05-GeV bins from 0.40-1.00 GeV,
- 2 0.25-GeV bins from 1.00-1.50 GeV,
- 3 0.50-GeV bins from 1.50-3.00 GeV and
- 1 bin from 3.00-10.00 GeV.

The ν_μ edge-to-edge binning has 22 bins in true neutrino energy which are bounded as follows:

- 1 bin from 0.00-0.30 GeV,
- 3 0.10-GeV bins from 0.30-0.60 GeV,
- 12 0.05-GeV bins from 0.60-1.20 GeV,
- 1 bin from 1.20-1.50 GeV,
- 3 0.50-GeV bins from 1.50-3.00 GeV,
- 1 bin from 3.00-5.00 GeV and
- 1 bin from 5.00-10.00 GeV.

The ν_e edge-to-edge binning has 12 bins in reconstructed neutrino energy which are bounded as follows:

- 1 0.35-GeV bin from 0.00-0.35 GeV,

- 5 0.15-GeV bins from 0.35-1.10 GeV,
- 2 0.20-GeV bins from 1.10-1.50 GeV,
- 2 0.25-GeV bins from 1.50-2.00 GeV,
- 1 bin from 2.00-3.00 GeV and
- 1 bin from 3.00-10.00 GeV.

The ν_e edge-to-edge binning has 33 bins in true neutrino energy which are bounded as follows:

- 2 0.25-GeV bin from 0.00-0.50 GeV,
- 15 0.05-GeV bins from 0.50-1.25 GeV,
- 15 0.25-GeV bins from 1.25-5.00 GeV and
- 1 bin from 5.00-10.00 GeV.

Chapter 6.

VALOR Oscillation Analysis Framework

The VALOR framework is a neutrino fitting framework that was first developed for the Tokai to Kamioka (T2K) experiment, but has since been adapted to also cover, Hyper-Kamiokande, DUNE and the SBN program [100].

Performing an analysis within VALOR involves a number of physics parameters that define a physics hypothesis (e.g. neutrino oscillations) and the relevant systematic uncertainties. Event rate predictions are constructed for the associated detector, beam and event sample. These predictions are constructed as a function of a kinematical variable for either a nominal scenario or with variations due to a physics hypothesis and/or systematic uncertainties. This approach allows for joint oscillation and systematic fits to be constructed from a binned likelihood fitting approach for a given event topology. Fits may be performed for individual detectors or for a combination of multiple detectors and may include any number of systematic uncertainties.

6.1. The VALOR Framework

The data inputs used for an oscillation analysis are mainly provided in the form of Monte Carlo Templates (MCTs), which provide a mapping between true and reconstructed variables. They are constructed following the full event processing chain which includes event simulation, reconstruction and selection. Since the MCTs include the effects from reconstruction and selection, it is not feasible to directly recreate them using only information on the flux, cross-section and efficiency. These MCTs, T, encapsulate a number of quantities describing a given event and are listed below,

b – Beam configuration e.g. neutrino or anti-neutrino mode,

d – Detector e.g. SBND, MicroBooNE or ICARUS,

s – Topological event selection e.g. ν_e CC-inclusive, ν_μ CC-inclusive,

m – True Reaction Mode e.g. ν_μ CC QE, ν_e CC $1\pi^\pm$,

r – A bin in multi-dimensional reconstructed kinematic space e.g. $E_{\nu,reco}$,

t – A bin in multi-dimensional true kinematic space e.g. $E_{\nu,true}$,

with $T = T_{d;b;s;m}(r,t)$. By combining T with the necessary physics parameters, $\vec{\theta}$, and systematic parameters, $\vec{f}$, the predicted event rate, $n^{pred}_{d;b;s}$, may be expressed as

$$n^{pred}_{d;b;s}(r;\vec{\theta};\vec{f}) = \sum_m \sum_t P_{d;b;m}(t;\vec{\theta}) \cdot R_{d;b;s;m}(r,t;\vec{f}) \cdot T_{d;b;s;m}(r,t) \cdot N^{MC}, \qquad (6.1)$$

where $P_{d;b;m}(t;\vec{\theta})$ represents the effect due to a physics hypothesis, $R_{d;b;s;m}(r,t;\vec{f})$ represents the response of a MCT bin to the systematic variations and $N^{MC} = \mathrm{POT}^{data}_{b;d}/\mathrm{POT}^{MC}_{b;d}$, which is the normalisation by which to scale the event rate to account for the POT which was used to construct the sample of neutrino events with respect to the nominal POT in the analysis. The variation due to systematic parameters is applied separately to each combination of beam, detector, topological selection and reaction mode in true-reconstructed space and is therefore dependant on, b, d, s and m. The dependence of $P_{d;b;m}(t;\vec{\theta})$ on d and b is due to d and b encapsulating the baseline information which is a component of the oscillation probability. The unoscillated CC MCTs are weighted by the appropriate oscillation probability, $P_{\nu_\alpha \to \nu_\beta}$, to reflect the change in event rate due to neutrino oscillations. The NC MCTs are left unweighted since they remain unchanged due to flavour oscillations. This distinction between CC and NC is encapsulated by m, hence, $P_{d;b;m}(t;\vec{\theta})$ is required to also be dependent on m.

For $n^{obs}_{d;b;s}(r)$ observed events, the log likelihood, $\ln\lambda_{d;b;s}(\vec{\theta},\vec{f})$, is given by

$$\ln\lambda_{d;b;s}(\vec{\theta},\vec{f}) = -\sum_{b,d,s,r}\left\{\left(n^{pred}_{d;b;s}(r,\vec{\theta},\vec{f}) - n^{obs}_{d;b;s}(r)\right) + n^{obs}_{d;b;s}(r)\cdot\ln\frac{n^{obs}_{d;b;s}(r)}{n^{pred}_{d;b;s}(r,\vec{\theta},\vec{f})}\right\}. \tag{6.2}$$

An additional term is applied to penalise deviations from the nominal values of systematic parameters which is defined as,

$$\ln\lambda_{syst}(\vec{f}) = -\frac{1}{2}(\vec{f}-\vec{f_0})^T\mathbf{V^{-1}}(\vec{f}-\vec{f_0}), \tag{6.3}$$

where $\vec{f_0}$ is a vector containing the nominal value of all the systematic parameters and $\mathbf{V}$ is a covariance matrix containing the uncertainties of the systematic parameters [101].

In the limit of large statistics, quantities of the form $-2\ln\lambda$ have a χ^2 distribution, hence calculating the log likelihood allows a goodness-of-fit test to be performed [102]. The total goodness-of-fit value is therefore given by,

$$\chi^2_{tot} = -2(\ln\lambda_{d;b;s}(\vec{\theta},\vec{f}) + \ln\lambda_{syst}(\vec{f})). \tag{6.4}$$

In order to create confidence regions, fits are performed between a certain *Asimov* dataset and $n^{pred}_{d;b;s}$. The Asimov dataset is a dataset where all systematic parameters are set to their nominal values and serves as a proxy for data in cases where only simulations are considered. It has been shown that in the same limit as the χ^2 approximation (in the limit of large statistics), the median of many toy MC experiments is equivalent to the Asimov dataset. This allows the significance of a given hypothesis to be compared to the median one whilst only requiring one *toy* experiment instead of needing to compute many toy MC experiments [103]. Two types of confidence regions may be constructed; an *exclusion* region and an *allowed* region. Both regions show the area where the chosen model is either compatible or incompatible with the data. The difference is due to the input data which has either no oscillation signal (an exclusion region) or there is an injected signal (an allowed region). In the case of exclusion regions, the Asimov dataset corresponds to the case where no oscillation are observed which is the null-hypothesis and for allowed regions, the oscillation parameters are set to that of the injected signal.

6.2. Oscillation Channels Within SBN

As was discussed in Section 3.7, the BNB is ν_μ dominated with a small portion of ν_e's present. In the presence of mixing with a light sterile neutrino this would result in the disappearance of some percentage of the ν_μ's due to oscillations. Additionally, ν_μ to ν_e oscillations would result in the increase of the number of ν_e's present. Finally, the number of intrinsic ν_e's present in the BNB coupled with the large event rate SBN will detect means there are sufficient statistics to observe the disappearance of some ν_e's due to oscillations. This results in three possible oscillation channels, ν_μ disappearance, ν_e appearance and ν_e disappearance. The mixing angles which determine their respective oscillation probabilities are shown in Equations (2.39 – 2.41) which also imply that the oscillation channels are coupled (that is the presence of non-zero ν_e appearance also requires non-zero ν_μ disappearance and ν_e disappearance). Despite this, currently the oscillation channels are treated completely independently. In principle oscillations involving ν_τ are also possible, but due to the high energy threshold required these are usually not expected to be observed with any significant statistics. The energy range of the BNB above the ν_τ threshold is of the order 1%, but since the statistics in SBND are large, this may be sufficient to observe ν_μ to ν_τ appearance. Currently this channels is not considered in the analysis, but may be explored in future work [104].

The ν_μ disappearance as well as both the ν_e channels have already been explored by a number of different experiments. This has lead to tension due to the conflict between null-results from some experiments and the hints of possible mixing with light sterile neutrinos seen by others.

The ν_μ disappearance channel has for example been investigated by MINOS/MINOS+, MiniBooNE/SciBar Booster Neutrino Experiment (SciBooNE) and the IceCube experiment. The combined results from the MiniBooNE and SciBooNE collaborations and a MiniBooNE only analysis (along with other experimental results) are shown on the left of Figure 6.1. The exclusion contours from MINOS and MINOS+ are shown on the right of Figure 6.1, with the black line representing the data and the dashed blue line being the expected sensitivity [105] [106]. It should be noted that the results from MINOS are shown as a function of $\sin^2\theta$ instead of $\sin^2 2\theta$ which is used for most other results. The results from 8 years of IceCube data are shown in Figure 6.2 along with other experimental results. The left plot is the 90% C.L. allowed region, whereas the right plot is the 99% C.L. exclusion contour. The star in each plot represents the best fit point. The results depend on both θ_{24} and θ_{34}, but the contours have been produced under the assumption that $\theta_{34} = 0$ [107].

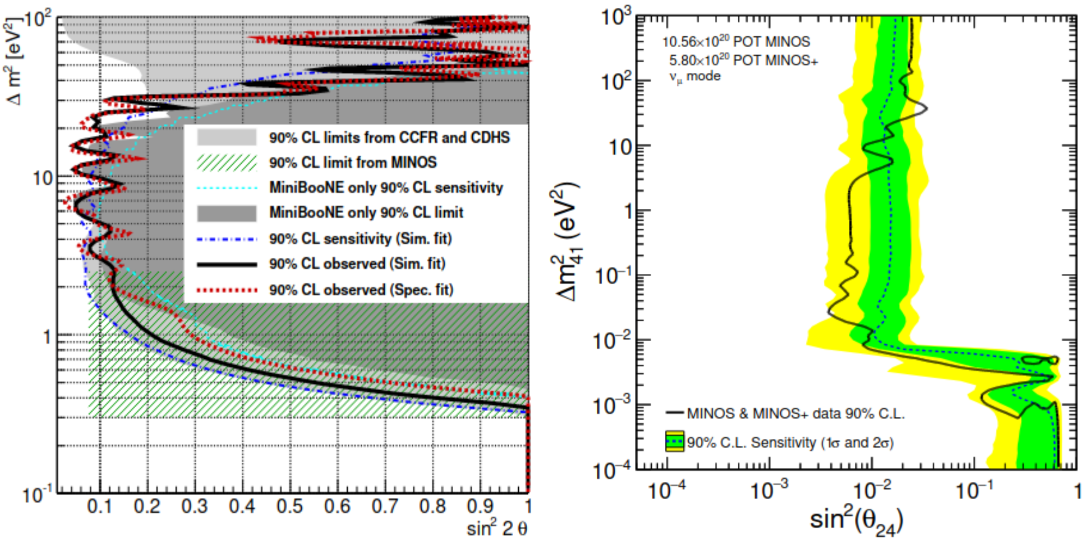

Figure 6.1.: Left: ν_μ disappearance exclusion contours obtained from the MiniBooNE and SciBooNE experiments along with other experimental results [105]. Right: ν_μ disappearance exclusion contour from the MINOS/MINOS+ experiment [106].

For the ν_e appearance channel, the allowed regions from the LSND and MiniBooNE experiments are shown in Figure 6.3, along with exclusion contours from experiments including, ICARUS, KARMEN, NOMAD, OPERA and E776 (which is combined with solar neutrino data) [17] [108] [109] [110] [111] [112] [113]. The

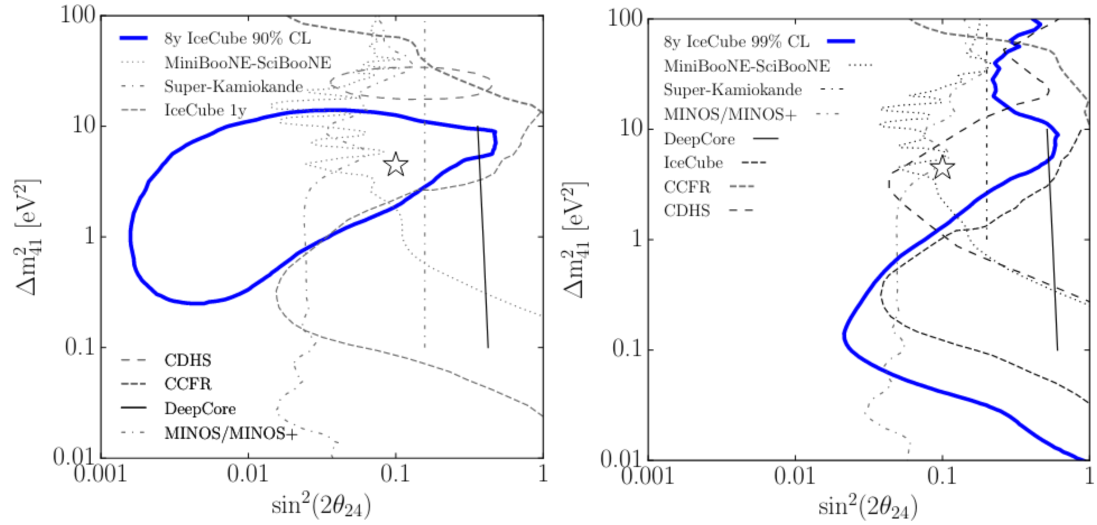

Figure 6.2.: ν_μ disappearance results from the 8 years of IceCube data. The 90% allowed region (Left) and the 99% exclusion region are shown under the assumption that $\theta_{34} = 0$ [107].

LSND result are produced from a combination of neutrinos from decay at rest (DaR) π^+ as well as decay in flight (DiF) pions meaning appearance of both ν_e and $\bar{\nu}_e$ are considered. MiniBooNE also observed both neutrino and anti-neutrinos from the BNB, whereas the KARMEN experiment considered the oscillations of $\bar{\nu}_\mu$ exclusively and the remaining experiments mentioned considered the oscillations of ν_μ exclusively [114].

Finally, the ν_e disappearance channel has been investigated with allowed regions being obtained from gallium and reactor experiments and exclusion regions being obtained from ν_e-carbon interaction data and solar neutrino data. Additionally, the near detector of the T2K experiment has provided both allowed and excluded regions which are shown in the left plot of Figure 6.4. An overlay of the T2K exclusion region along with the other experimental results are shown in the right plot of Figure 6.4, all of which are shown at the 95% CL. In both cases, the coloured star and circles correspond to the best fit point of a given result [115].

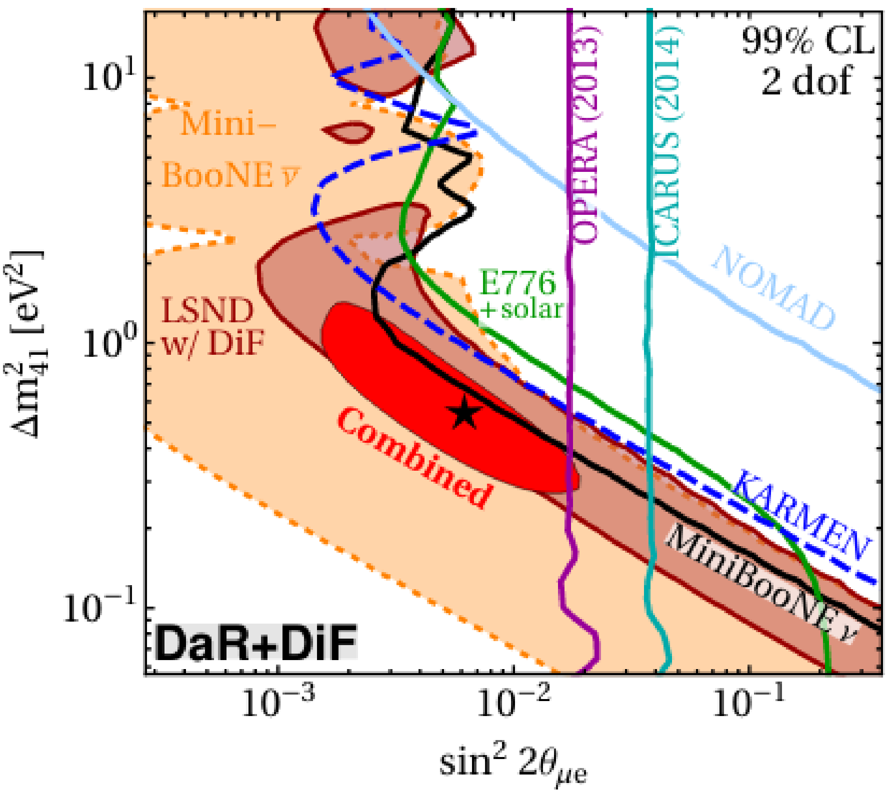

Figure 6.3.: ν_e appearance allowed regions from the LSND and MiniBooNE experiments and exclusion contours from the ICARUS, KARMEN, NOMAD, OPERA and E776 experiments [114].

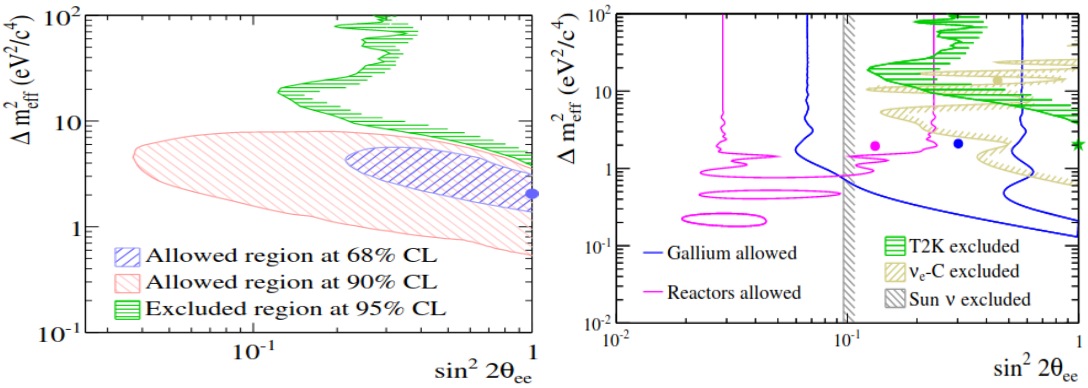

Figure 6.4.: Left: ν_e disappearance exclusion and allowed regions from the near detector of the T2K experiment. Right: ν_e disappearance allowed regions from gallium and reactor experiments and exclusion regions from T2K, ν_e-carbon interaction data and solar neutrino data.

The remainder of this chapter will focus on the ν_e channels. Some of the key results for the ν_μ channel are shown in Appendix D and a detailed discussion can be found in [116].

6.3. Systematic Uncertainties within SBN

The systematics that are considered as part of the current SBN analysis have been detailed in Section 5.5. Unless explicitly stated, efficiency uncertainties are not considered due to their currently not being a general consensus on their magnitude.

The systematics from the GENIE and MicroBooNE reweight packages are initially in the form of weights which correspond to variations of the parameter. Systematic uncertainties in this form can not be directly used in an oscillation analysis, but must instead first be processed internally, the details of which are described below.

6.3.1. Processing Systematic Uncertainties

Many *universes* are simulated, each with different weights associated to each of the systematic parameters. This allows the impact of varying systematic parameters on the event rate of neutrino interactions to be observed. If the systematic parameters are uncorrelated, the weights are simply an $n\sigma$ variation which is the value used in a given universe. For correlated parameters, the weights are due to a unique variation of all the correlated parameters of a given universe. Of the systematic uncertainties associated with either the GENIE or MicroBooNE reweight packages, only the neutrino production flux uncertainties which are listed in Table 5.6 are correlated. All other parameters are uncorrelated.

Depending on whether a given systematic parameter is correlated or not, the way that it is processed within VALOR is done in two different ways. For the uncorrelated parameters, a set of associated response functions which represent the impact on the event rate that tweaking a given systematic parameter will have are constructed. For each parameter, individual response functions are constructed for each combination of *d, b, s, m, r* and *t*. Each response function is a 13 knot spline which nominally represents the change in event rate from parameter variations ranging from [-3, +3]σ in 0.5σ intervals. The response functions are constructed by first identifying the 12 universes which have a variation closest to each of the non-zero σ intervals and then taking the ratio of the event rate from the selected universe in a 2D (r, t) bin to the nominal event rate in that bin. By definition there will be a knot at 0σ with a response of 1, however, in most cases the remaining 12 knots will not be exactly at 0.5σ intervals.

For the case of correlated parameters, it is not straightforward to construct response functions as was done for the uncorrelated parameters because any variations will be due to multiple parameters. These parameters are instead represented by a covariance matrix. Matrices of this type, $\mathbf{C_{ij}}$, are constructed such that,

$$\mathbf{C_{ij}} = \frac{1}{U}\sum_{u=1}^{U}(N_i^u - N_i^{cv})(N_j^u - N_j^{cv}), \tag{6.5}$$

where U is the number of universes, $N_{i,j}^u$ is the event rate in universe u in bin i or j and $N_{i,j}^{cv}$ nominal event rate in bin i or j.

6.3.2. Validating Systematic Uncertainties

In order to establish that the systematic parameters are being correctly handled within VALOR, a comparison between the event rate variations as seen by VALOR and those obtained directly from the universes is performed. This is done in two different ways;

1. Tweak the nominal spectra using the response functions within VALOR for a single systematic parameter and then compare with the spectra that were obtained directly from the universe files.
2. Generate N toy samples (typically 500 in order to match the total number of universes) with some set of systematic parameters randomly tweaked. The one sigma spread from all the toys is found. This is done for both VALOR and for the universe files and the results are compared.

As an example, the $+1\sigma$ variation for the $f_{HornCurrent}$, $f_{M_A^{CCRes}}$ and $f_{\Delta\rightarrow N\gamma}$ parameters from the ν_e sample in SBND between the VALOR response functions and the universes are shown in Figure 6.5[1]. A complete list of the $+3\sigma$ variation

[1]The terms *spline* and *response function* are used interchangeably.

comparisons for all the uncorrelated systematic parameters in SBND are shown for the ν_e channel in Appendix A. In all cases there is either perfect agreement or differences of only up to a few tens of events. It should be noted that the event rate shown in the spectra used for validating the systematic parameters for the ν_e channel is several orders of magnitude greater than the nominal event rates as seen in for example Figure 6.7. This is due to manually setting the oscillation parameters to $\sin^2 2\theta_{\mu e} = 1$ and $\Delta m^2_{41} = 100$ eV^2 which ensures that many of the events from the oscillated $\nu_\mu \rightarrow \nu_e$ sub-sample are processed which is required because the response functions are indexed by mode and therefore contributions from all the sub-samples are needed. Since oscillation and systematic effects commute, this approach is sufficient to correctly produce a complete set of response functions. In the nominal event rate spectra, the assumption is that no oscillations occur, so no events from the oscillated sample are included hence the much lower event rate.

Figure 6.6 shows a double ratio comparison from VALOR and the universes for the flux, proposal interaction and modern interaction systematic parameters. These plots are constructed by first finding the ratio between the 1σ variation and the nominal using VALOR and the analogous ratio using the universe files. The double ratio is then constructed by taking the ratio of both the previous 1σ ratios. There are some minor differences between the variations in VALOR and the universes, however, event perfect agreement is not expected since the 1σ variations are found by taking the average from many toy samples. Nevertheless, the disagreement is for the most part $< 1\%$ with a maximum of just over 2%.

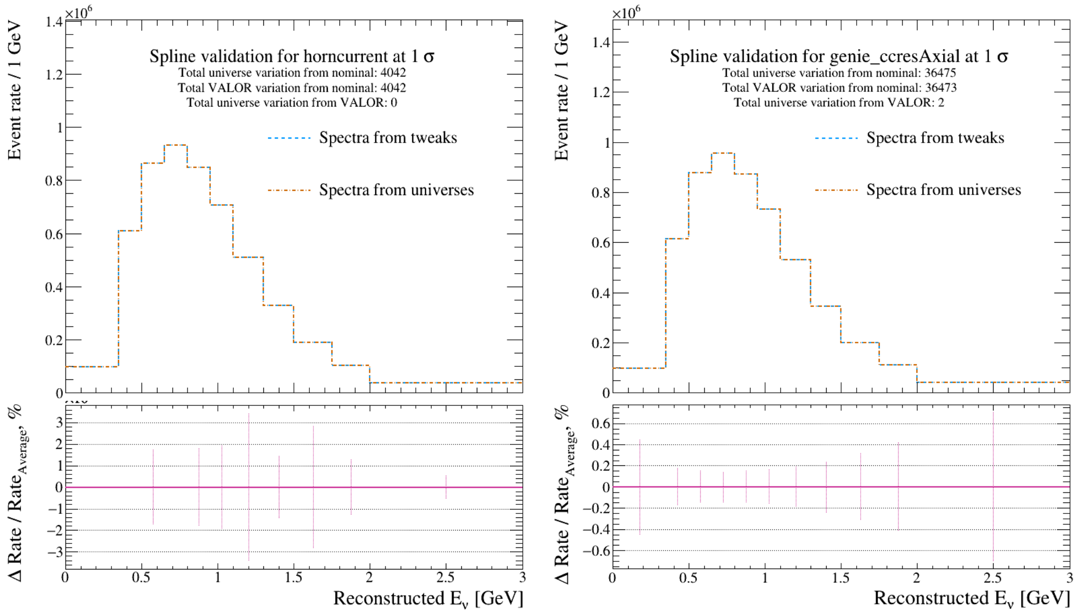

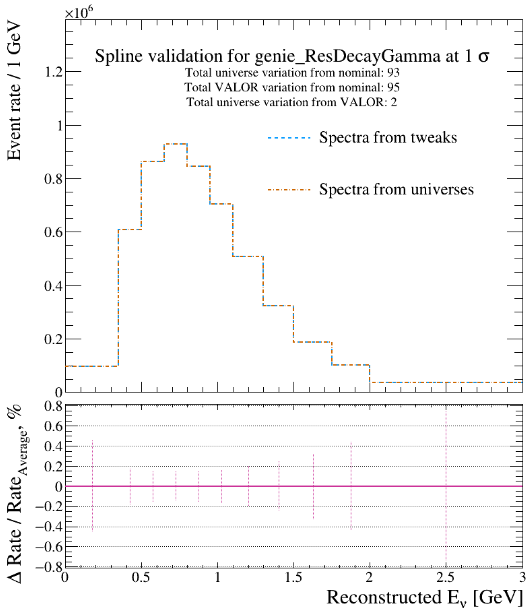

Figure 6.5.: A comparison of the $+1\sigma$ variation from the response functions in VALOR and the universes for the $f_{HornCurrent}$, $f_{M_A^{CCRes}}$ and $f_{\Delta\rightarrow N\gamma}$ parameters. The $f_{HornCurrent}$ parameter shows perfect agreement between VALOR and the universes whereas both the $f_{M_A^{CCRes}}$ and $f_{\Delta\rightarrow N\gamma}$ parameters only have an event rate difference of 2.

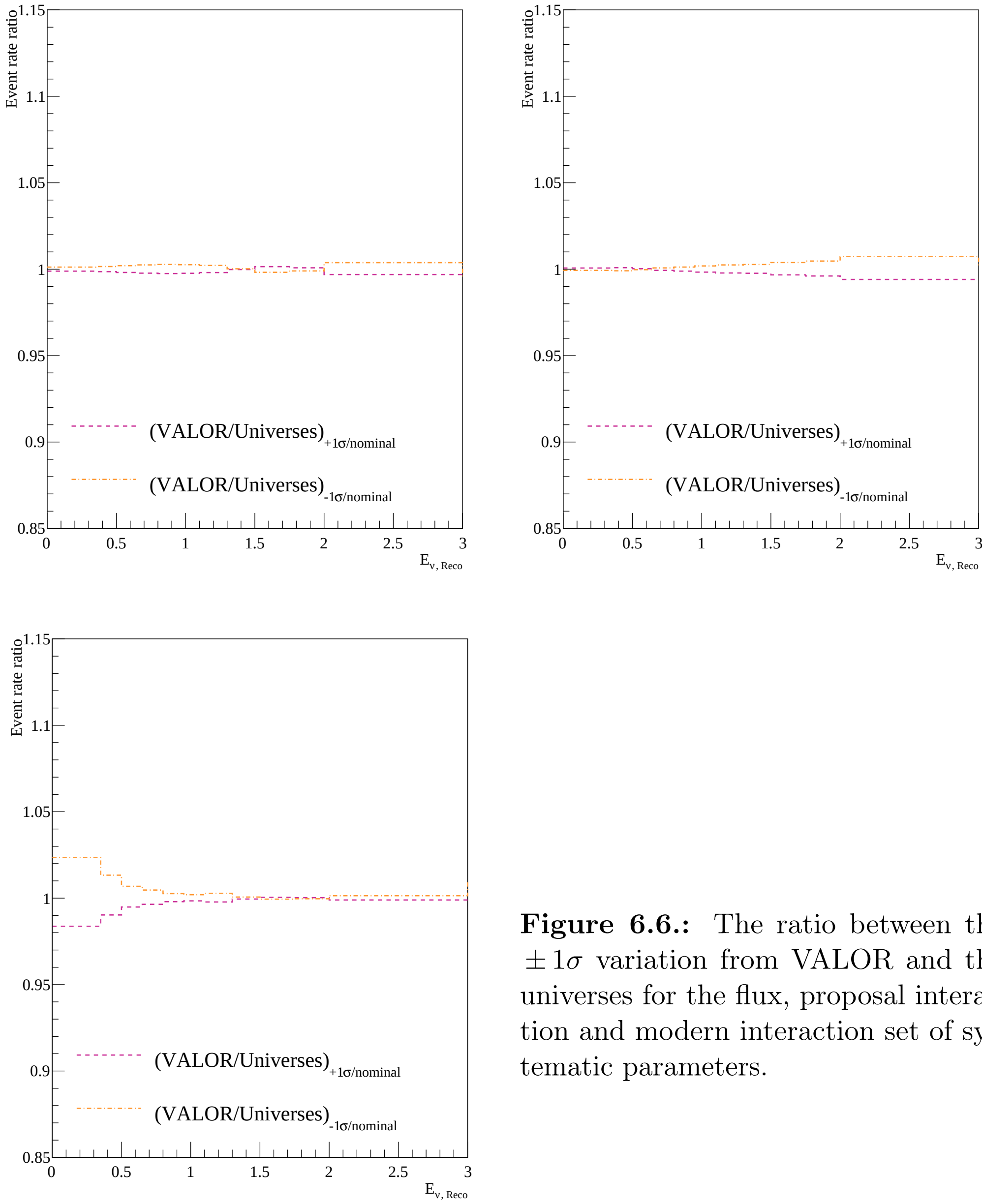

Figure 6.6.: The ratio between the $\pm 1\sigma$ variation from VALOR and the universes for the flux, proposal interaction and modern interaction set of systematic parameters.

6.4. Event Rate Predictions and the Expected Signal

In order to perform sensitivity calculations, the events are required to be binned in terms of a kinematical variable, which is chosen to be the neutrino energy.

The nominal event rates, event rates with an uncertainty envelope due to systematic uncertainties and the event rates due to an oscillation signal are discussed below for each SBN detector. Additionally, the impact of the uncorrelated systematic parameters are quantified in terms of their effect on the oscillation parameters.

6.4.1. Nominal Event Rate Predictions

It has been established that there are two oscillations channels associated with ν_e: ν_e appearance and ν_e disappearance. Since the only difference between these channels is due to oscillations, the nominal event rates are common between the two.

The breakdown of the nominal number of events by interaction mode and channel are shown numerically in Table 6.1, Table 6.2 and Table 6.3 for SBND, MicroBooNE and ICARUS respectively. The same events rates are also shown in Figure 6.7 in the form of spectra. The spectra show the modal breakdown in terms of the coarse reaction modes where the events have been binned in reconstructed neutrino energy.

Similar to Figure 6.7, Figure 6.8 again shows the nominal event rate in each SBN detector, but in an integrated form. Additionally, 1σ prefit uncertainty envelopes are shown which are due to the flux and interaction systematics. The accuracy of say the ICARUS prediction can be improved by constraining the systematics from an SBND fit. This is shown in Figure 6.9 which shows the nominal integrated ICARUS spectrum along with the prefit uncertainty envelope as in Figure 6.8, but also a postfit uncertainty envelope based on an SBND fit is shown. The reduction in size from the prefit to postfit envelope highlights the impact of SBND on the ICARUS prediction.

	$\nu_\mu \to \nu_\mu$	$\bar{\nu}_\mu \to \bar{\nu}_\mu$	$\nu_e \to \nu_e$	$\bar{\nu}_e \to \bar{\nu}_e$	$\nu_\mu \to \nu_e$	$\bar{\nu}_\mu \to \bar{\nu}_e$	Non-neutrino	Total
CCQE	17.0	0.0	5957.8	166.6	0.0	0.0	N/A	6141.5
CCMEC	1.1	0.0	1433.0	59.7	0.0	0.0	N/A	1493.8
CC1$\pi^\pm$	234.6	0.0	2859.9	112.4	0.0	0.0	N/A	3206.8
CC1π^0	230.7	0.0	513.8	14.6	0.0	0.0	N/A	759.2
CC2$\pi^\pm$	19.3	0.0	293.3	7.9	0.0	0.0	N/A	320.6
CC2π^0	5.2	0.0	24.1	0.6	0.0	0.0	N/A	29.9
CC1$\pi^0$1$\pi^\pm$	37.1	0.0	187.0	7.0	0.0	0.0	N/A	231.1
CCcoherent	0.0	0.0	38.1	3.8	0.0	0.0	N/A	41.9
CCν_e El	0.0	0.0	N/A	N/A	N/A	N/A	N/A	0.0
CCother	20.7	0.0	270.9	8.3	0.0	0.0	N/A	299.9
NCEL	3.4	0.0	0.0	0.0	N/A	N/A	N/A	3.5
NCMEC	0.6	0.0	0.0	0.0	N/A	N/A	N/A	0.6
NC1$\pi^\pm$	135.6	0.0	0.8	0.0	N/A	N/A	N/A	136.4
NC1π^0	772.6	0.0	5.5	0.2	N/A	N/A	N/A	778.4
NC2$\pi^\pm$	2.3	0.0	0.1	0.0	N/A	N/A	N/A	2.4
NC2π^0	6.9	0.0	0.1	0.0	N/A	N/A	N/A	7.0
NC1$\pi^0$1$\pi^\pm$	16.1	0.0	0.4	0.0	N/A	N/A	N/A	16.5
NCcoherent	76.8	0.0	0.4	0.1	N/A	N/A	N/A	77.2
NC1γ	0.0	0.0	0.0	0.0	N/A	N/A	N/A	0.0
NCν_e El	181.9	0.0	N/A	N/A	N/A	N/A	N/A	181.9
NCother	50.0	0.0	0.5	0.0	N/A	N/A	N/A	50.5
ν_e El	N/A	N/A	0.0	0.0	0.0	0.0	N/A	0.0
cosmic	N/A	N/A	N/A	N/A	N/A	N/A	0.3	0.3
dirt	N/A	N/A	N/A	N/A	N/A	N/A	33.9	33.9
Total	1812.0	0.0	11585.9	381.3	0.0	0.0	34.2	13813.5

Table 6.1.: Nominal ν_e event rate breakdown in SBND.

	$\nu_\mu \to \nu_\mu$	$\bar{\nu}_\mu \to \bar{\nu}_\mu$	$\nu_e \to \nu_e$	$\bar{\nu}_e \to \bar{\nu}_e$	$\nu_\mu \to \nu_e$	$\bar{\nu}_\mu \to \bar{\nu}_e$	Non-neutrino	Total
CCQE	4.2	0.0	384.9	10.4	0.0	0.0	N/A	399.5
CCMEC	0.1	0.0	93.9	3.7	0.0	0.0	N/A	97.6
CC1$\pi^\pm$	18.9	0.0	196.8	7.5	0.0	0.0	N/A	223.2
CC1π^0	19.1	1.0	35.5	1.1	0.0	0.0	N/A	56.7
CC2$\pi^\pm$	1.0	0.0	21.9	0.6	0.0	0.0	N/A	23.5
CC2π^0	3.3	0.0	1.9	0.1	0.0	0.0	N/A	5.2
CC1$\pi^0$1$\pi^\pm$	7.2	0.0	13.6	0.6	0.0	0.0	N/A	21.4
CCcoherent	0.0	0.0	2.6	0.4	0.0	0.0	N/A	3.0
CCν_e El	0.0	0.0	N/A	N/A	N/A	N/A	N/A	0.0
CCother	3.3	0.0	19.1	0.4	0.0	0.0	N/A	22.9
NCEL	0.3	0.0	0.0	0.0	N/A	N/A	N/A	0.3
NCMEC	0.0	0.0	0.0	0.0	N/A	N/A	N/A	0.0
NC1$\pi^\pm$	13.9	0.0	0.1	0.0	N/A	N/A	N/A	14.0
NC1π^0	59.3	1.0	0.4	0.0	N/A	N/A	N/A	60.7
NC2$\pi^\pm$	0.7	0.0	0.0	0.0	N/A	N/A	N/A	0.7
NC2π^0	0.7	0.1	0.0	0.0	N/A	N/A	N/A	0.7
NC1$\pi^0$1$\pi^\pm$	2.3	0.0	0.0	0.0	N/A	N/A	N/A	2.3
NCcoherent	5.5	0.2	0.0	0.0	N/A	N/A	N/A	5.8
NC1γ	0.0	0.0	0.0	0.0	N/A	N/A	N/A	0.0
NCν_e El	14.9	0.0	N/A	N/A	N/A	N/A	N/A	14.9
NCother	3.3	0.0	0.0	0.0	N/A	N/A	N/A	3.3
ν_e El	N/A	N/A	0.0	0.0	0.0	0.0	N/A	0.0
cosmic	N/A	N/A	N/A	N/A	N/A	N/A	0.0	0.0
dirt	N/A	N/A	N/A	N/A	N/A	N/A	14.8	14.8
Total	157.8	2.3	770.9	24.8	0.0	0.0	14.8	970.6

Table 6.2.: Nominal ν_e event rate breakdown in MicroBooNE.

	$\nu_\mu \to \nu_\mu$	$\bar{\nu}_\mu \to \bar{\nu}_\mu$	$\nu_e \to \nu_e$	$\bar{\nu}_e \to \bar{\nu}_e$	$\nu_\mu \to \nu_e$	$\bar{\nu}_\mu \to \bar{\nu}_e$	Non-neutrino	Total
CCQE	4.6	0.0	727.9	19.3	0.0	0.0	N/A	751.9
CCMEC	0.2	0.0	176.5	7.1	0.0	0.0	N/A	183.8
CC1$\pi^\pm$	37.4	0.2	372.3	12.9	0.0	0.0	N/A	422.8
CC1π^0	25.8	0.1	64.8	2.2	0.0	0.0	N/A	92.9
CC2$\pi^\pm$	4.9	0.1	39.4	1.0	0.0	0.0	N/A	45.4
CC2π^0	2.9	0.1	3.6	0.1	0.0	0.0	N/A	6.6
CC1$\pi^0$1$\pi^\pm$	7.5	0.0	25.8	1.1	0.0	0.0	N/A	34.5
CCcoherent	0.0	0.0	5.0	0.5	0.0	0.0	N/A	5.4
CCν_e El	0.0	0.0	N/A	N/A	N/A	N/A	N/A	0.0
CCother	2.8	0.0	36.9	0.8	0.0	0.0	N/A	40.5
NCEL	0.5	0.0	0.0	0.0	N/A	N/A	N/A	0.5
NCMEC	0.0	0.0	0.0	0.0	N/A	N/A	N/A	0.0
NC1$\pi^\pm$	17.7	0.2	0.1	0.0	N/A	N/A	N/A	18.1
NC1π^0	108.5	0.7	0.7	0.0	N/A	N/A	N/A	110.0
NC2$\pi^\pm$	0.7	0.0	0.0	0.0	N/A	N/A	N/A	0.8
NC2π^0	0.9	0.0	0.0	0.0	N/A	N/A	N/A	0.9
NC1$\pi^0$1$\pi^\pm$	3.4	0.1	0.1	0.0	N/A	N/A	N/A	3.6
NCcoherent	11.3	0.4	0.1	0.0	N/A	N/A	N/A	11.8
NC1γ	0.0	0.0	0.0	0.0	N/A	N/A	N/A	0.0
NCν_e El	17.9	0.0	N/A	N/A	N/A	N/A	N/A	17.9
NCother	8.0	0.0	0.1	0.0	N/A	N/A	N/A	8.1
ν_e El	N/A	N/A	0.0	0.0	0.0	0.0	N/A	0.0
cosmic	N/A	N/A	N/A	N/A	N/A	N/A	2.3	2.3
dirt	N/A	N/A	N/A	N/A	N/A	N/A	24.1	24.1
Total	255.0	2.0	1453.3	44.9	0.0	0.0	26.4	1781.6

Table 6.3.: Nominal ν_e event rate breakdown in ICARUS.

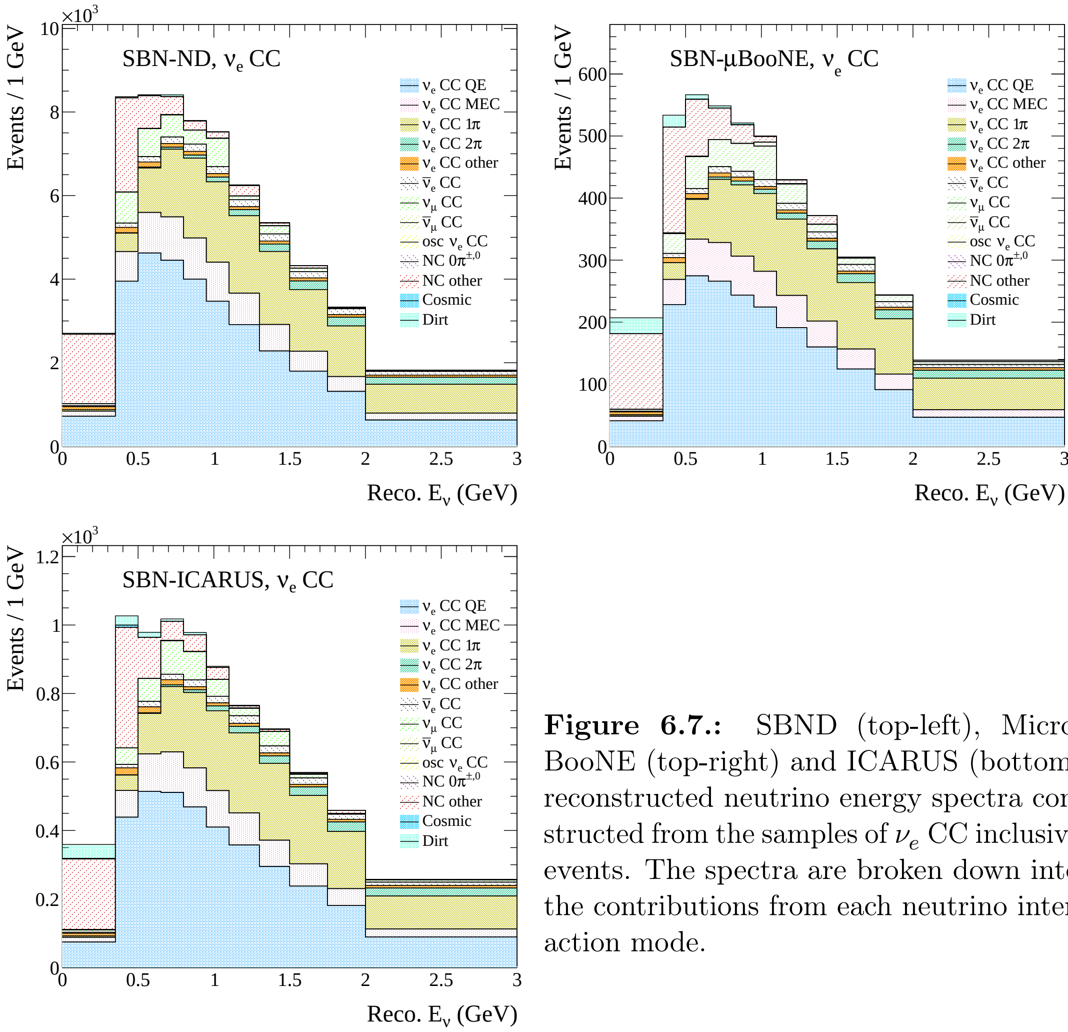

Figure 6.7.: SBND (top-left), MicroBooNE (top-right) and ICARUS (bottom) reconstructed neutrino energy spectra constructed from the samples of ν_e CC inclusive events. The spectra are broken down into the contributions from each neutrino interaction mode.

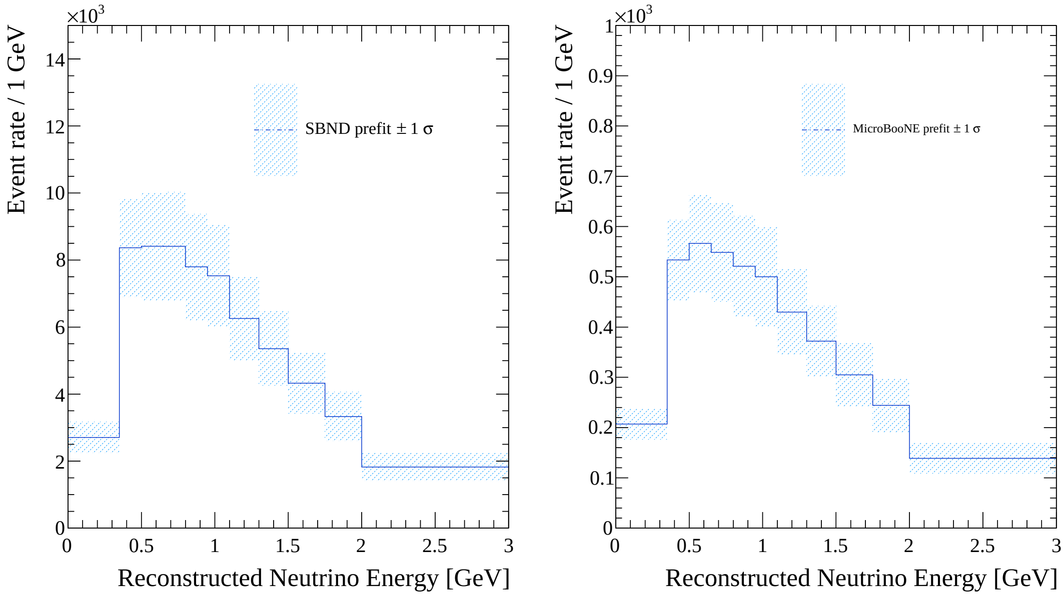

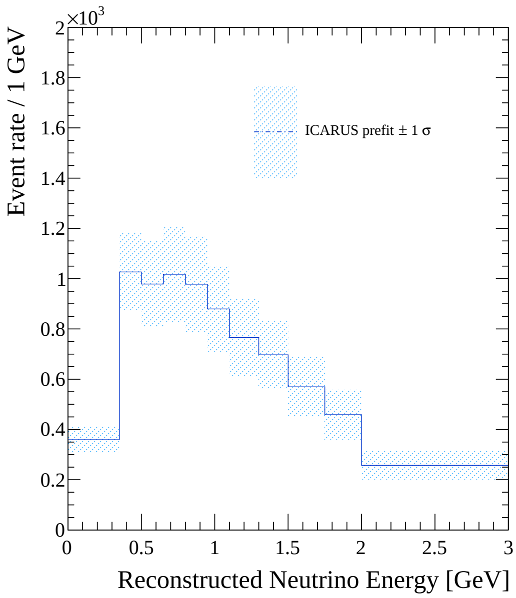

Figure 6.8.: SBND (top-left), MicroBooNE (top-right) and ICARUS (bottom) integrated reconstructed neutrino energy spectra constructed from the samples of ν_e CC inclusive events. A 1σ prefit uncertainty envelope from the flux and interaction systematics is also shown.

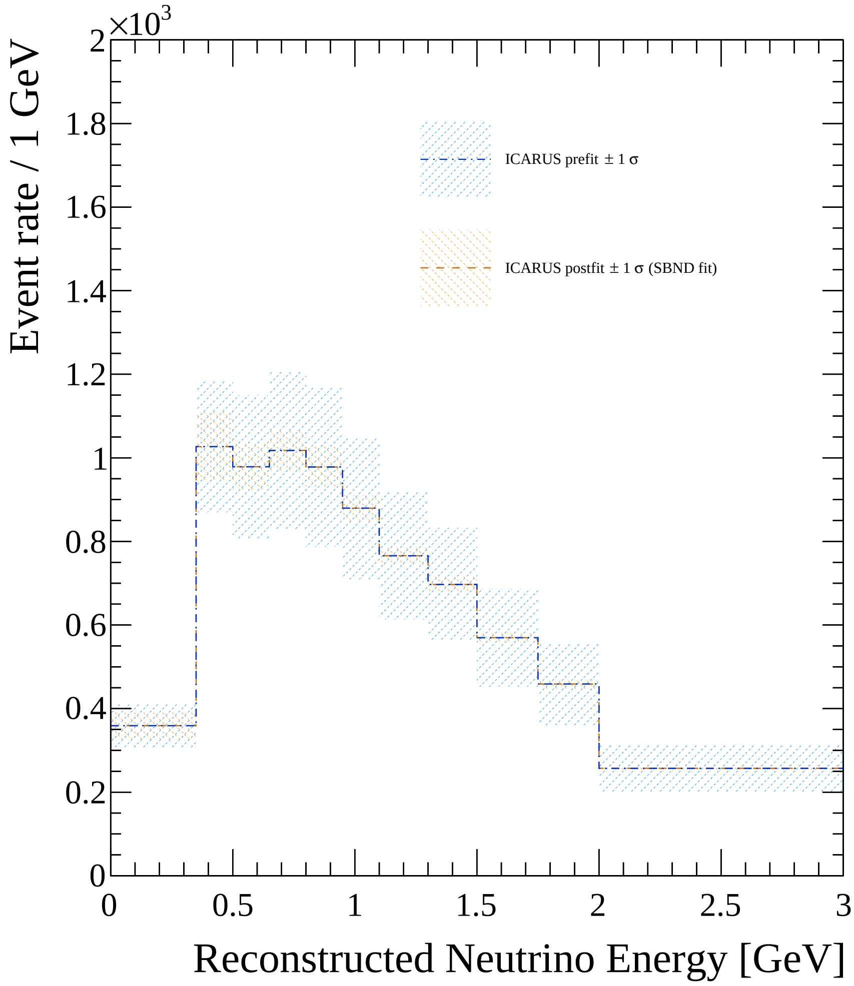

Figure 6.9.: ICARUS integrated reconstructed neutrino energy spectrum constructed from the samples of ν_e CC inclusive events. The 1σ prefit envelope is shown as well as a 1σ postfit envelope based on a SBND fit. The reduction in size of the error envelope when going from prefit to postfit shows the impact of SBND on improving the accuracy of the ICARUS prediction.

6.4.2. Impact of Systematic Uncertainties

To assess the impact of the different systematic parameters on the oscillation parameters the following study is performed;

1. Generate a toy experiment with a given oscillation signal with a single systematic parameter, f_i, set to $\pm 1\sigma$ from its nominal value and all other systematic parameters are set to their nominal value.

2. Perform a fit on the toy experiment with f_i fixed to its nominal value. Both the oscillation parameters and all the systematic parameters are initially set to their nominal value and are allowed to float with the exception of f_i. The other systematic parameters are allowed to float in order to obtain the best possible agreement between the fit and the toy experiment.

3. Steps 1. and 2. are then repeated for all i systematic parameters of interest. Both the $+1\sigma$ and -1σ variations should be performed for each systematic parameter since the effect on the oscillation parameters is typically not symmetric.

If f_i were allowed to float it would be expected that the fit would be able to recover the same oscillation parameters used in the toy experiment since the same MC was used for the toy experiment and the fit. By fixing f_i to its nominal value in the fit, the fit is forced to make a mistake. This results in the fit remapping the changes in f_i to the oscillation parameters (and the other systematic parameters).

This study was performed for the ν_e appearance and disappearance channels using oscillation parameters $\sin^2 2\theta_{\mu e} = 0.003$, $\Delta m^2_{41} = 1.32$ eV^2 and $\sin^2 2\theta_{ee} = 0.4$, $\Delta m^2_{41} = 3$ eV^2 respectively and includes the results from all uncorrelated systematic parameters. The results are shown in Figure 6.10 and Figure 6.11. For both oscillation parameters, the ratio of their value after performing the fit to their nominal value, $\mathcal{R}$, are shown after having varied f_i by $\pm 1\sigma$. The ratios shown in Figure 6.10 and Figure 6.11 are always ≥ 1 by construction since $\mathcal{R}$ is defined as,

$$\mathcal{R} = \begin{cases} \frac{\zeta_{fit}}{\zeta_{nom}}, & \text{if } \zeta_{fit} > \zeta_{nom} \\ \frac{\zeta_{nom}}{\zeta_{fit}}, & \text{if } \zeta_{nom} > \zeta_{fit}, \end{cases} \tag{6.6}$$

where $\zeta \in \{\sin^2 2\theta, \Delta m^2_{41}\}$ and the subscript *nom* and *fit* refer to the nominal value of the oscillation parameters and the values after performing the fit respectively. The arrows are colour coded such that black corresponds to the case where $\zeta_{fit} > \zeta_{nom}$ and red corresponds to the case where $\zeta_{nom} > \zeta_{fit}$.

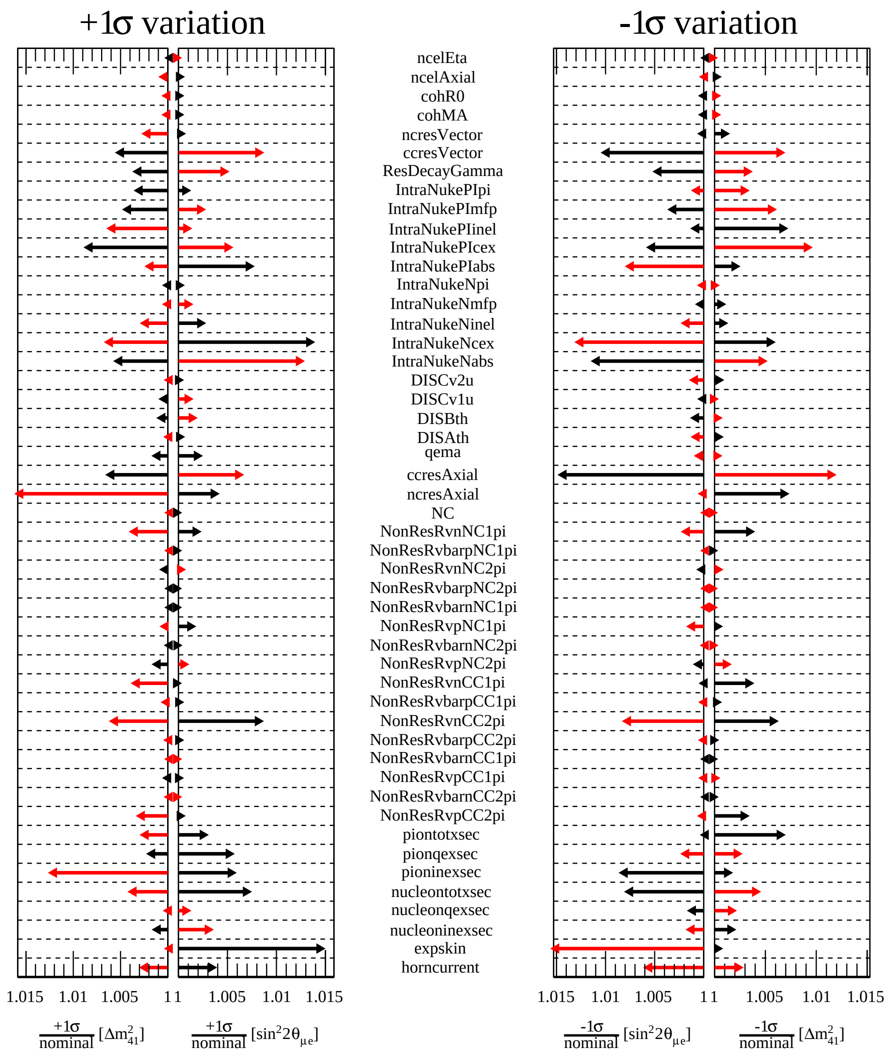

Figure 6.10.: The variation in the ν_e appearance oscillation parameters due to varying a single systematic parameter at a time by $\pm 1\sigma$.

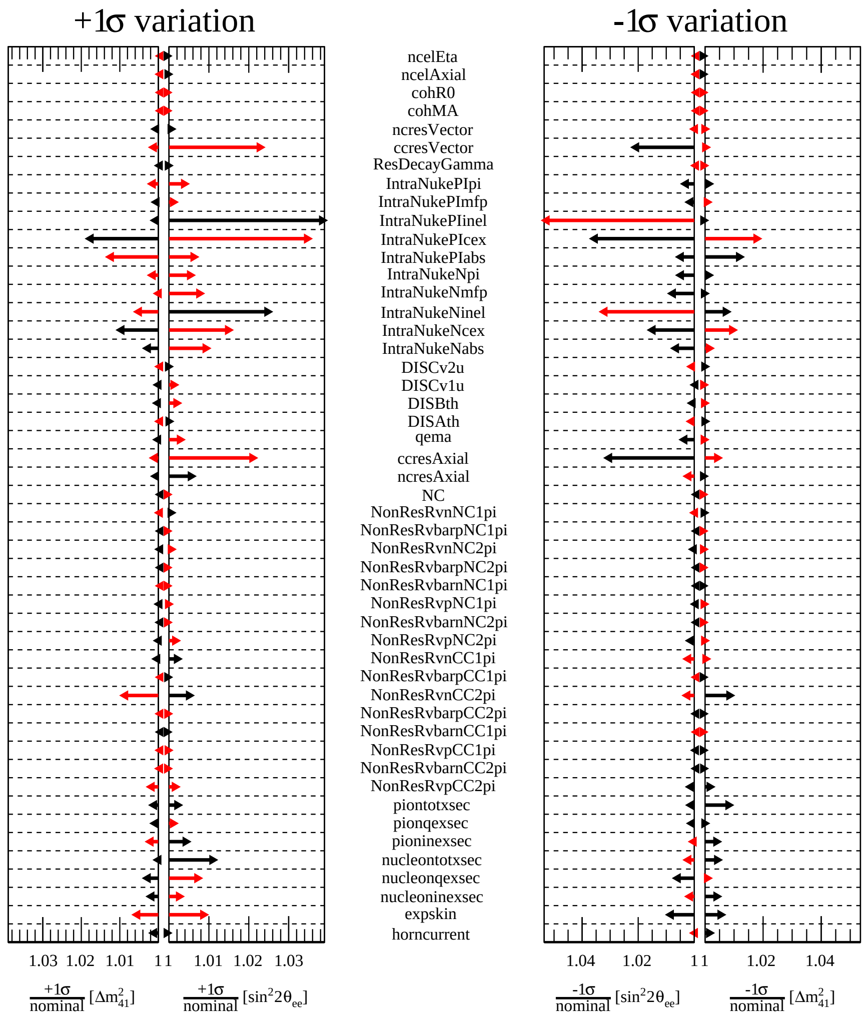

Figure 6.11.: The variation in the ν_e disappearance oscillation parameters due to varying a single systematic parameter at a time by $\pm 1\sigma$.

6.4.3. Expected Oscillation Signal

Assuming that mixing with a light sterile neutrino occurs, a change to the nominal event rate will be observed. Since the oscillation channels are currently considered as stand alone analyses, this will either result in an increase or decrease in the event rate depending on whether an appearance or disappearance channel is considered.

ν_e Appearance Analysis

The ν_e appearance channel is concerned with oscillations from ν_μ to ν_e meaning an increase in the event rate is expected. This is shown in Figure 6.12 where the nominal event rate breakdown is shown as in Figure 6.7, but overlayed with and integrated spectrum that was produced with oscillation parameters $\sin^2 2\theta_{\mu e} = 0.003$ and $\Delta m^2_{41} = 1.32$ eV^2. The oscillation signal seen for these parameters in SBND is small whereas for MicroBooNE and ICARUS it is substantial which is consistent with what is seen in Figure 3.14. This highlights the fact that SBND will largely be used to constrain systematic parameters due to observing no or very few oscillated events with the oscillation signal being largely left to MicroBooNE and ICARUS.

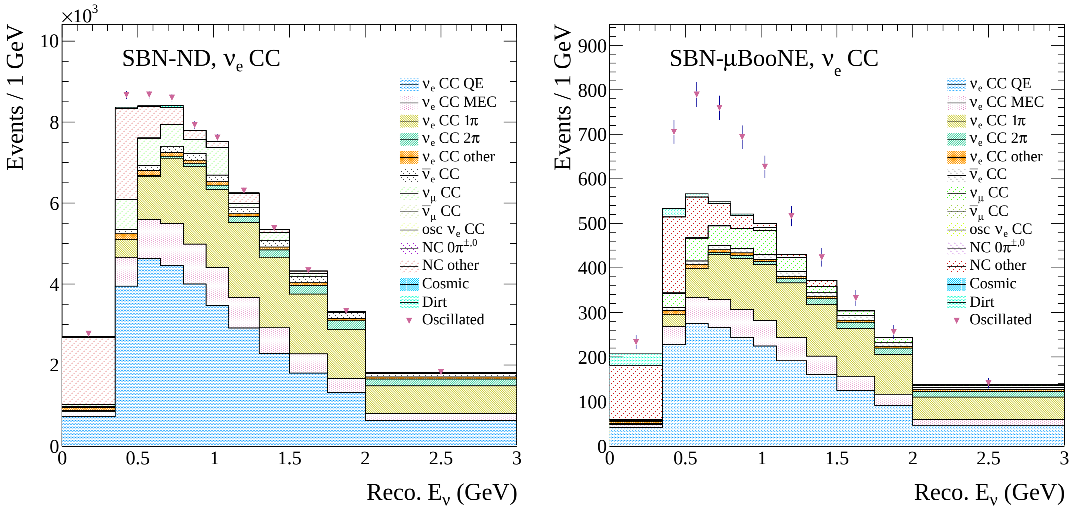

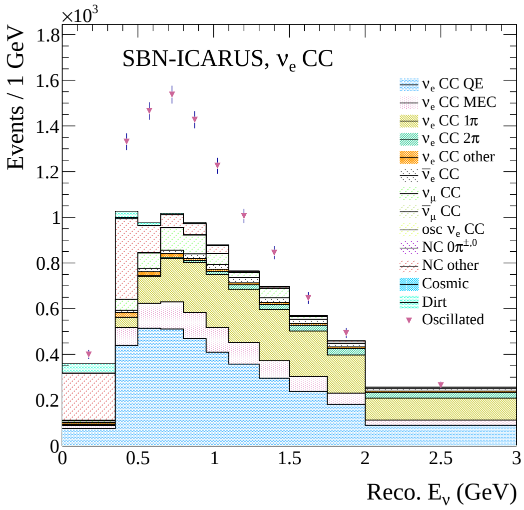

Figure 6.12.: The nominal spectra as in Figure 6.7 but an additional integrated oscillated spectrum with oscillation parameters, $\sin^2 2\theta_{\mu e} = 0.003$ and $\Delta m^2_{41} = 1.32$ eV^2 has been overlayed showing the increase in event rate.

The top left plot of Figure 6.13 shows the ν_e appearance statistical only exclusion contour and allowed region from fits combining all three SBN detectors. The details of constructing sensitivity contours within SBN are detailed in Section 6.5. The injected point $\Delta m^2_{41} = 1.32$ eV^2, $\sin^2 2\theta_{\mu e} = 0.003$, used when producing the allowed region is shown along with two further points on the exclusion contour at $\Delta m^2_{41} = 1$ eV^2, $\sin^2 2\theta_{\mu e} = 0.0014$ and $\Delta m^2_{41} = 100$ eV^2, $\sin^2 2\theta_{\mu e} = 0.0005$. ν_e appearance spectra are produced using oscillation parameters corresponding to each of these three points for each of the three SBN detectors. The ratio of each of these oscillated spectra to the nominal for each detector are shown in the the remaining plots in Figure 6.13 and highlight the expected oscillation signal.

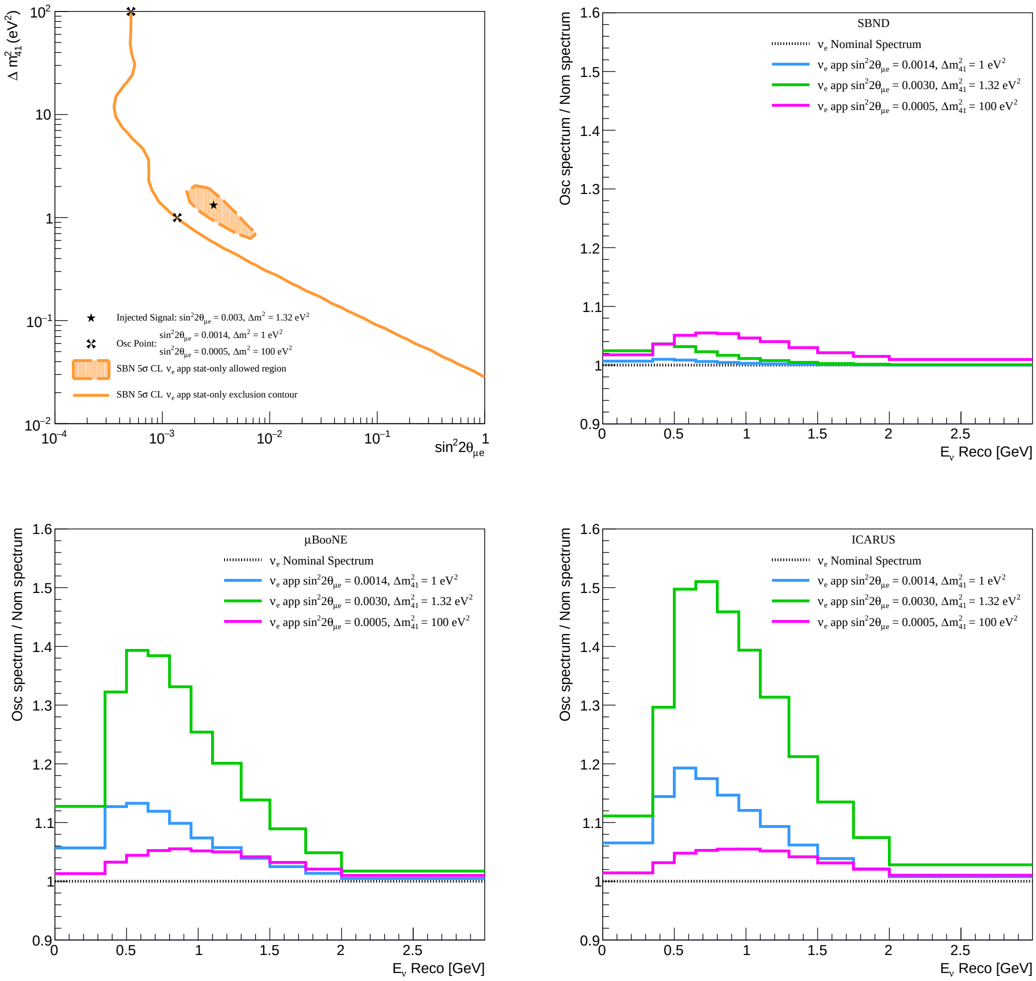

Figure 6.13.: ν_e appearance stat-only exclusion contour and allowed region. The injected point at $\sin^2 2\theta_{\mu e} = 0.003$, $\Delta m^2_{41} = 1.32$ eV^2 used for the allowed region is shown along with two further points at $\sin^2 2\theta_{\mu e} = 0.0014$, $\Delta m^2_{41} = 1$ eV^2 and $\sin^2 2\theta_{\mu e} = 0.0005$, $\Delta m^2_{41} = 100$ eV^2 (top left). The ratio of spectra with oscillation parameters corresponding to the three points mentioned versus nominal are shown for sbnd (top right), MicroBooNE (bottom left) and ICARUS (bottom right).

ν_e Disappearance Analysis

Mirroring the ν_e appearance channel, the ν_e disappearance channel observes a reduction in the nominal ν_e event rate. This is shown in Figure 6.14 where the integrated spectrum produced with oscillation parameters $\sin^2 2\theta_{ee} = 0.4$ and

$\Delta m^2_{41} = 3\ \mathrm{eV}^2$ has been overlayed onto the breakdown of the nominal spectrum for each of the three detectors. As is the case for ν_e appearance, the oscillation signal is relatively small in SBND whereas both MicroBooNE and ICARUS observe a much more significant signal.

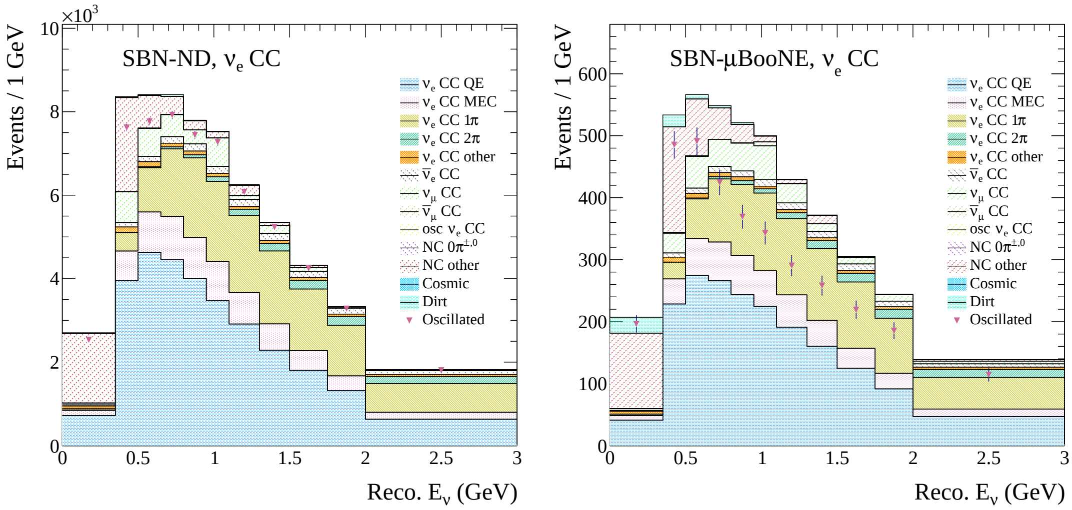

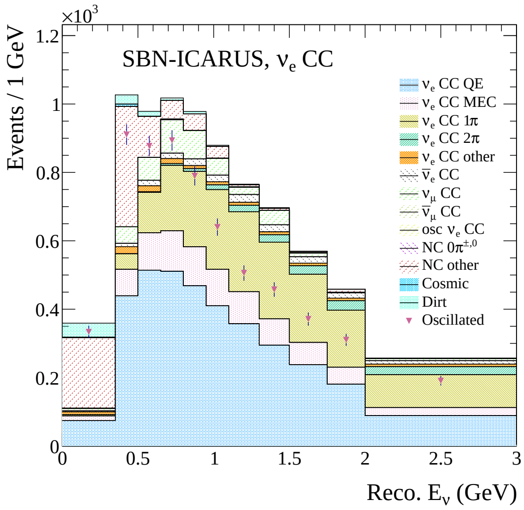

Figure 6.14.: The nominal spectra as in Figure 6.7 but an additional integrated oscillated spectrum with oscillation parameters, $\sin^2 2\theta_{ee} = 0.4$ and $\Delta m^2_{41} = 3\ \mathrm{eV}^2$ has been overlayed which shows the decrease in event rate.

The top left plot of Figure 6.15 shows the ν_e disappearance statistical only exclusion contour and allowed region from fits combining all three SBN detectors. The injected point $\Delta m^2_{41} = 3\ \mathrm{eV}^2$, $\sin^2 2\theta_{\mu e} = 0.4$, used when producing the allowed region is shown along with two further points on the exclusion contour at $\Delta m^2_{41} = 1\ \mathrm{eV}^2$, $\sin^2 2\theta_{\mu e} = 0.29$ and $\Delta m^2_{41} = 100\ \mathrm{eV}^2$, $\sin^2 2\theta_{\mu e} = 0.085$. ν_e disappearance spectra are produced using oscillation parameters corresponding to each of these three points for each of the three SBN detectors. The ratio of each of these oscillated spectra to the nominal for each detector are shown in the the remaining plots in Figure 6.15 and highlight the expected oscillation signal.

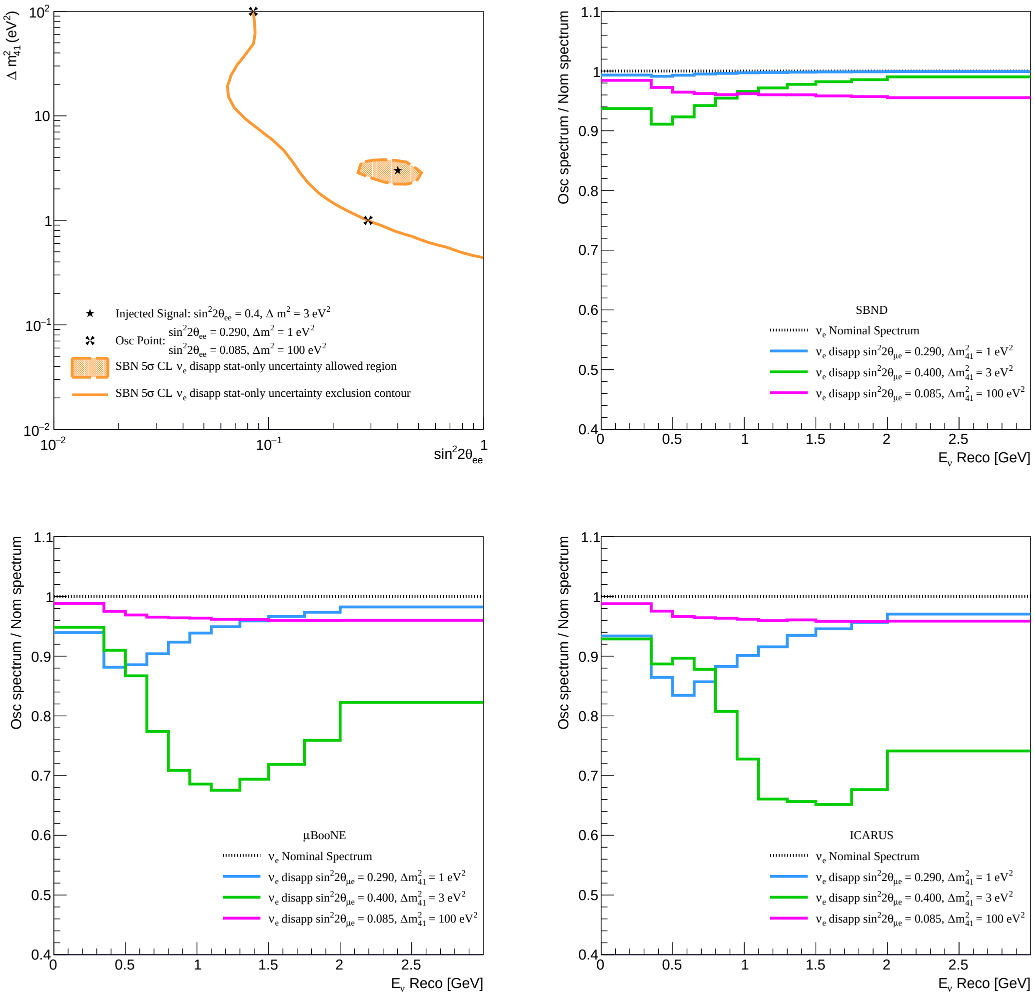

Figure 6.15.: ν_e disappearance stat-only exclusion contour and allowed region. The injected point at $\sin^2 2\theta_{ee} = 0.4$, $\Delta m^2_{41} = 3$ eV^2 used for the allowed region is shown along with two further points at $\sin^2 2\theta_{ee} = 0.29$, $\Delta m^2_{41} = 1$ eV^2 and $\sin^2 2\theta_{ee} = 0.085$, $\Delta m^2_{41} = 100$ eV^2 (top left). The ratio of spectra with oscillation parameters corresponding to the three points mentioned versus nominal are shown for SBND (top right), MicroBooNE (bottom left) and ICARUS (bottom right).

6.5. SBN Sensitivity Contour Construction

The relevant phase space for each of the three analysis channels considered is split into a 40×40 grid. This number was chosen in order to find a balance between having a sufficient granularity when constructing contours without having excessive computing times. The dimensions of the phase space considered are different for each analysis channel and are listed in Table 6.4. Fits are performed for each of the 40×40 points where the oscillation parameters are fixed and the systematic parameters, if any, are allowed to float up to $\pm 5\sigma$ from their nominal value. Once the fits have been produced, a contour of constant χ^2 is constructed. The χ^2 value is chosen such that it corresponds to a certain confidence level, CL, which for SBN analyses is typically 5σ. The critical value of χ^2, $\chi^2_{critical}$, corresponding to a 5σ confidence level along with a number of other $\chi^2_{critical}$ values with their associated confidence levels which are commonly seen in literature are outlined in Table 6.5. An example of a 2D χ^2 surface with exclusion contours at 90%, 3σ and 5σ confidence levels for the ν_e appearance channel is shown in Figure 6.16. The contours have been produced for the entire SBN program with the inclusion of flux and interaction systematics.

Analysis Channel	Phase Space Considered	
	$\sin^2 2\theta$	Δm^2_{41}
ν_μ Disappearance	$\theta_{\mu\mu}$: $[10^{-3} - 1]$	$[10^{-2} - 10^2]$ eV^2
ν_e Appearance	$\theta_{\mu e}$: $[10^{-5} - 1]$	$[10^{-2} - 10^2]$ eV^2
ν_e Disappearance	θ_{ee}: $[10^{-2} - 1]$	$[10^{-2} - 10^2]$ eV^2

Table 6.4.: The phase space considered when constructing contours for each of the three oscillation channels within SBN.

The complete ν_e appearance exclusion sensitivities and allowed regions for both the statistical only case and with the inclusion of flux and interaction systematics are shown in Figure 6.17 for the entire SBN program alongside external limits from the LSND and KARMEN experiments [114]. For comparison purposes, it should be noted that the contours produced for the SBN program are at the

Confidence level	68%	90%	95%	99%	3σ	5σ
$\chi^2_{critical}$	0.23	1.64	2.71	5.41	7.74	23.66

Table 6.5.: The $\chi^2_{critical}$ values corresponding to various confidence levels which are commonly used when performing sensitivity studies. The confidence levels and $\chi^2_{critical}$ are related via $CL = \int_0^{\chi^2_{critical}} \frac{e^{-x/2} x^{u/2-1}}{2^{u/2}\Gamma(u/2)} dx$, where u is the degrees of freedom (in this case 1) and Γ is the Gamma function [117].

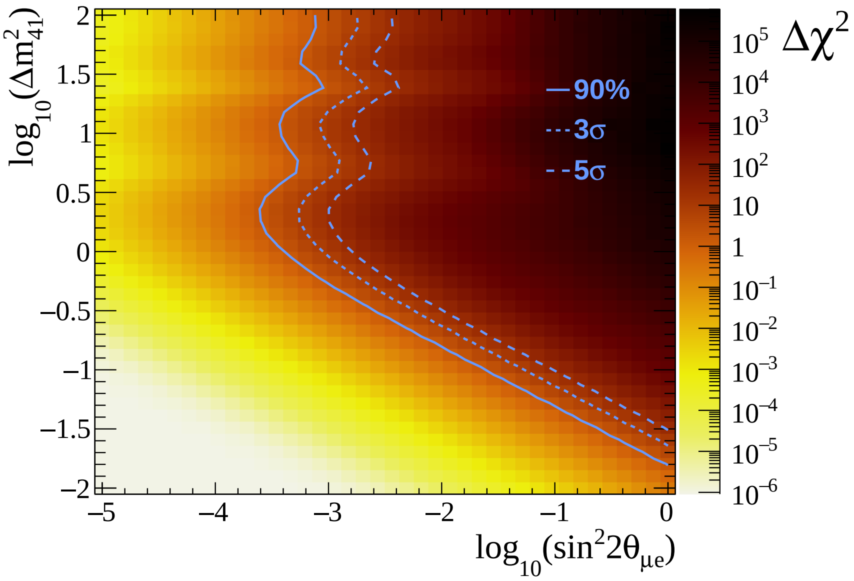

Figure 6.16.: The ν_e appearance χ^2 surface from fits including flux and interaction systematics. Contours of constant χ^2 values which correspond to 90%, 3σ and 5σ confidence levels have been overlayed onto the surface.

5σ confidence level whereas the results from both LSND and KARMEN are at the 99% confidence level. The results from SBN shows an improvement over the KARMEN results for essentially all Δm^2_{41} values and the allowed region is largely consistent with the LSND result.

The complete ν_e disappearance exclusion sensitivities and allowed regions for both the statistical only case and with the inclusion of flux and interaction systematics are shown in Figure 6.18 for the entire SBN program alongside external limits from the ND280 detector which serves as one of the near detectors as part of the T2K experiment [118]. The results for the SBN program are shown at a 5σ

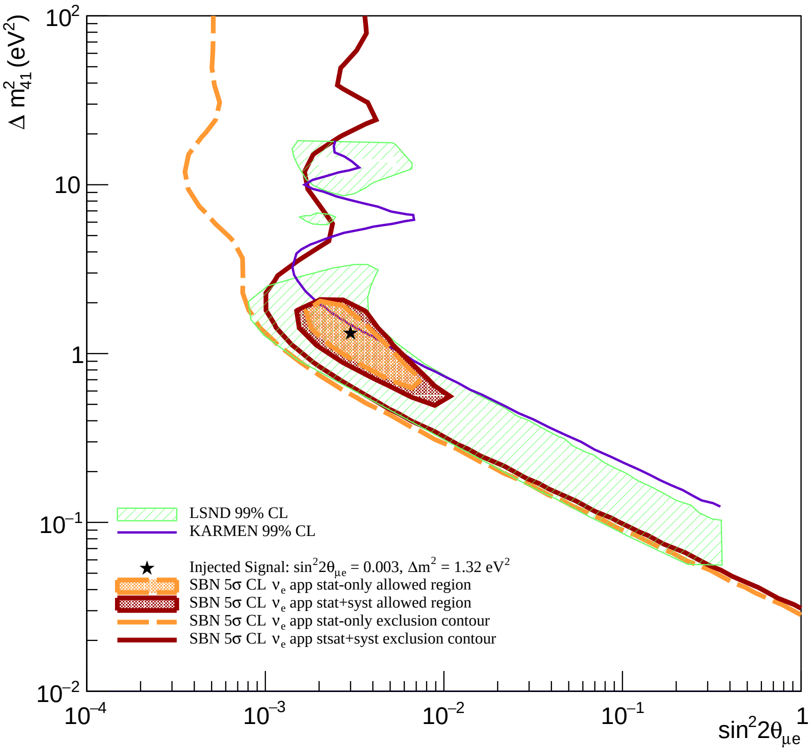

Figure 6.17.: ν_e appearance exclusion contours and allowed regions for the stat only case and with flux and interaction systematic uncertainties included. External limits from the LSND and KARMEN experiments have been overlayed [114]. (The confidence intervals for each contour are shown in the legend and it should be noted that those from external limits are not the same as those from the contours produced for the SBN program.)

confidence level whereas the allowed region from the T2K experiment is shown at both 68% and 90% confidence level and the exclusion contour is at a 95% confidence level [115]. The results from SBN exclude a substantial portion of the T2K allowed region with the exclusion limits at high Δm^2_{41} not being as strong for the current comparison.

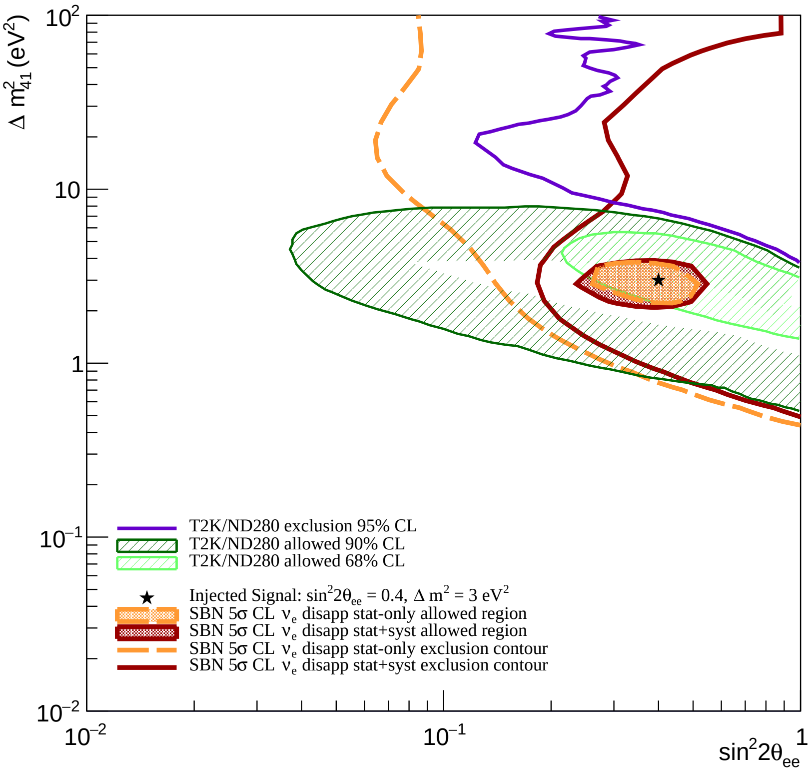

Figure 6.18.: ν_e disappearance exclusion contours and allowed regions for the stat only case and with flux and interaction systematic uncertainties included. External limits from the T2K experiments have been overlayed [115]. (The confidence intervals for each contour are shown in the legend and it should be noted that those from external limits are not the same as those from the contours produced for the SBN program.)

6.6. Further Study on Sensitivities

The sensitivity contours shown in Figure 6.17 and Figure 6.18 are produced from combined fits from all the three SBN detectors with the inclusion of all the flux and interaction systematic uncertainties outlined in Section 5.5.

Fits may, however, also be produced for an individual detector or any combination of multiple detectors. Additionally, there is complete freedom to choose which systematic parameters are included in the fits. This allows for the option to only include a single systematic parameter, or an entire sub-group of parameters.

This section will discuss the impact on the sensitivity contours due to;

- Different combinations of individual and multiple detectors.
- The inclusion of a select number of individual systematic parameters.
- The inclusion of each set of flux and systematic parameters.
- The inclusion of additional efficiency uncertainties.
- Tweaking the energy smearing used in the event selection based on results from Chapter 4.

6.6.1. Impact of Detector Combinations

To see the impact that each detector has on the sensitivity contour, the left plot of Figure 6.19 shows the ν_e appearance statistical-only sensitivity contours from each individual detector as well as all possible combinations (the black curve labelled "SBN" refers to a contour from combining all three detectors). It can be seen that for large Δm^2_{41} (greater than ~ 5 eV^2), that the SBND detector dominates the sensitivity whereas for small Δm^2_{41} (less than ~ 0.7 eV^2) the ICARUS detector dominates. It should also be noted that only by combining the fits from all three detectors can the best sensitivities be obtained. Having this multi-detector design is one of the key advantages of the SBN program. The right plot of Figure 6.19 is akin to the left one, but with the inclusion of flux and interaction systematics in the fits. Again, the improvements to the sensitivity are highlighted by combining multiple detectors.

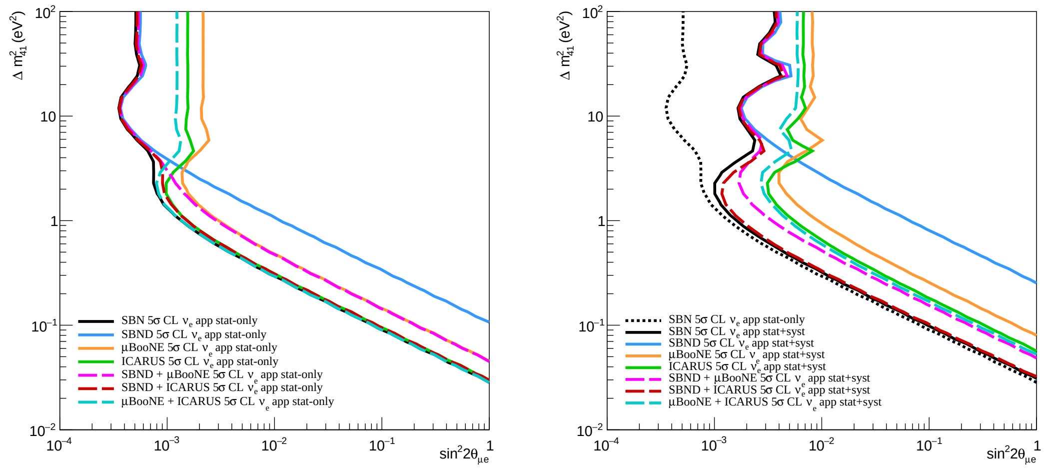

Figure 6.19.: Contributions to the SBN ν_e appearance sterile oscillation sensitivity from each detector and combinations of detectors in the SBN program. The statistical-only plots in the left-hand figure show that SBND is most sensitive to the region $\Delta m^2_{41} > \sim 3$ eV^{2}and ICARUS is most sensitive to $\Delta m^2_{41} < \sim 3$ eV^2. The right-hand figure includes flux and interaction systematic parameters and highlights the considerable improvement in the oscillation sensitivity when including multiple detectors in the fits.

Similar to Figure 6.19, Figure 6.20 shows the ν_e disappearance sensitivity from individual detectors and combinations of multiple detectors for both the statistical-only case (Left) and the case with flux and interaction systematics (Right). Again, SBND dominates the sensitivity at high mass splitting whereas ICARUS is dominant for low mass splitting with the emphasis being on the improvement to the overall sensitivity when fits from all three SBN detectors are combined.

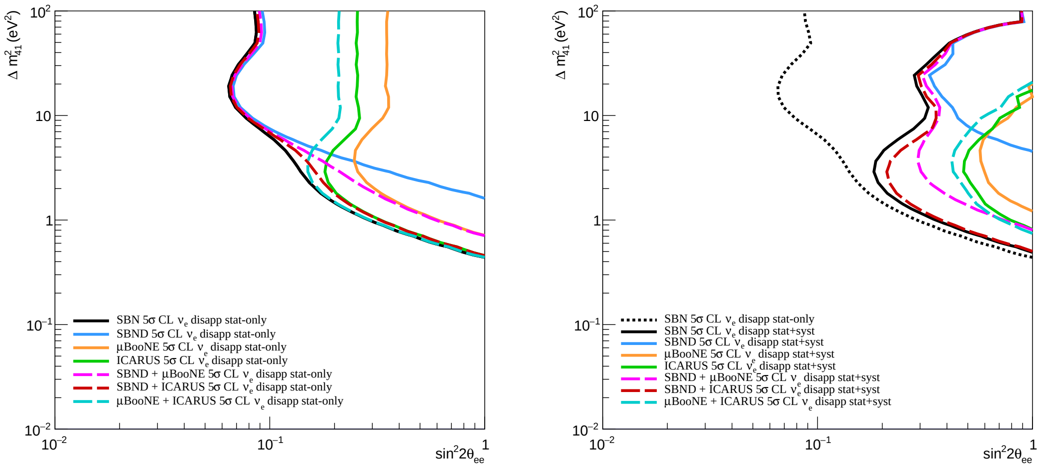

Figure 6.20.: Contributions to the SBN ν_e disappearance sterile oscillation sensitivity from each detector and combinations of detectors in the SBN program produced. The statistical-only plots in the left-hand figure show that SBND is most sensitive to the region $\Delta m^2_{41} > 3$ eV^2 and ICARUS is most sensitive below $\Delta m^2_{41} < 3$ eV^2. The right-hand figure includes flux and interaction systematic parameters and highlights the considerable improvement in the oscillation sensitivity when including multiple detectors in the fits.

6.6.2. Impact of Systematic Parameters

The impact of the $f_{M_V^{CCRes}}$, $f_{M_A^{CCRes}}$, $f_{R_N^{CEx}}$ and $f_{\sigma^{\pi}_{INEL}}$ parameters on the ν_e appearance exclusion sensitivities are shown in Figure 6.21. The parameters were applied one at a time and chosen as some that showed the largest variations in Figure 6.10, ensuring at least on parameter from each systematic subgroup. Similarly, the $f_{M_V^{CCRes}}$, $f_{M_A^{CCRes}}$, $f_{R_\pi^{CEx}}$ and $f_{expskin}$ parameters were used for the ν_e disappearance channel and the results are shown in Figure 6.22.

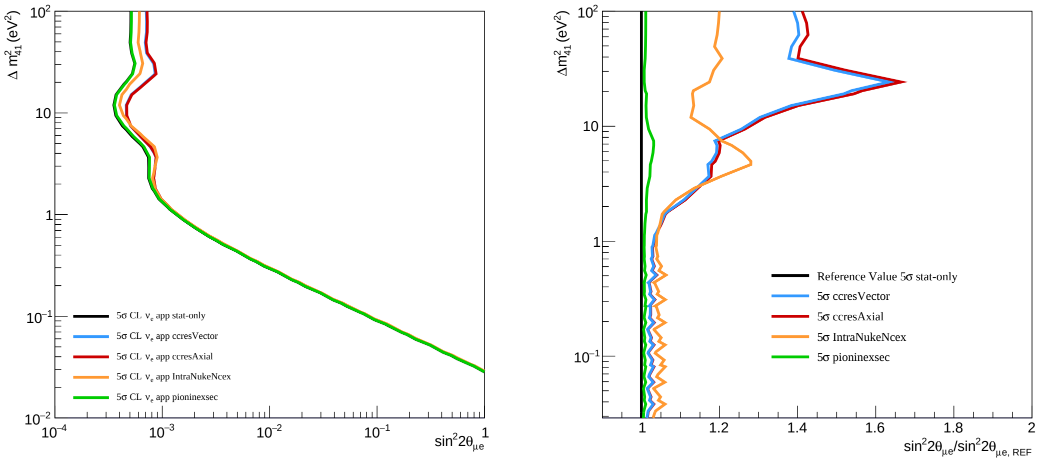

Figure 6.21.: Left: ν_e appearance exclusion contours with inclusion of a single systematic parameter at a time. The systematic parameters considered are $f_{M_V^{CCRes}}$, $f_{M_A^{CCRes}}$, $f_{R_N^{CEx}}$ and $f_{\sigma^{\pi}_{INEL}}$. Right: The ratio of the exclusion contours with the inclusion of a systematic parameter the statistical only contour.

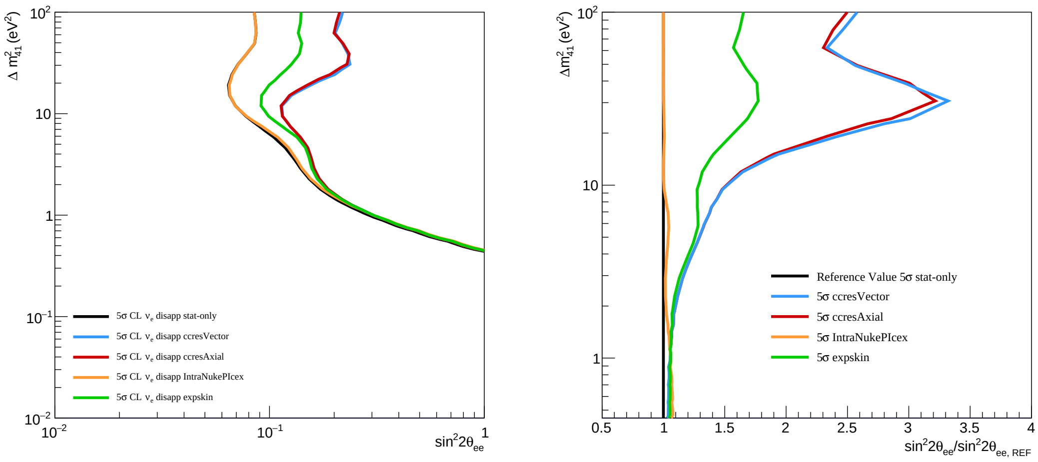

Figure 6.22.: Left: ν_e disappearance exclusion contours with inclusion of a single systematic parameter at a time. The systematic parameters considered are $f_{M_V^{CCRes}}$, $f_{M_A^{CCRes}}$, $f_{R_\pi^{CEx}}$ and $f_{expskin}$. Right: The ratio of the exclusion contours with the inclusion of a systematic parameter the statistical only contour.

The results from applying the flux, proposal interaction, modern interaction and proposal + modern interaction systematic subgroups for the ν_e appearance channel is shown in the left plot of Figure 6.23. This highlights the reduction in sensitivity when individually applying each systematic subgroup when compared to the statistical only case. The right hand plot of Figure 6.23 shows the ratio of the exclusion contours to the statistical only case. This gives a clearer measure of the impact on the sensitivity in $\sin^2 2\theta_{\mu e}$ space. It follows that the interaction systematics have the biggest impact on the sensitivity which in turn are dominated by the modern set of interaction parameters. The proposal set of interaction parameters have the smallest impact with the magnitude of the impact from the flux parameters being somewhere in between the two sets of interaction parameters.

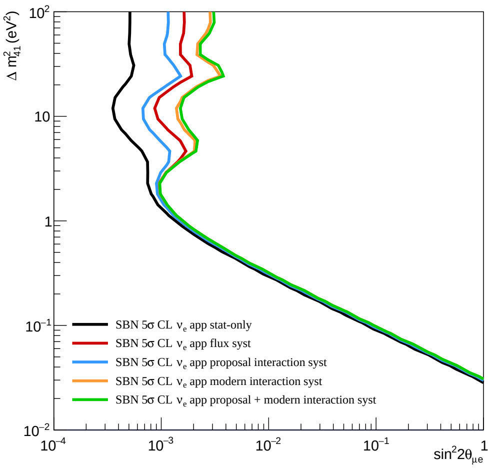

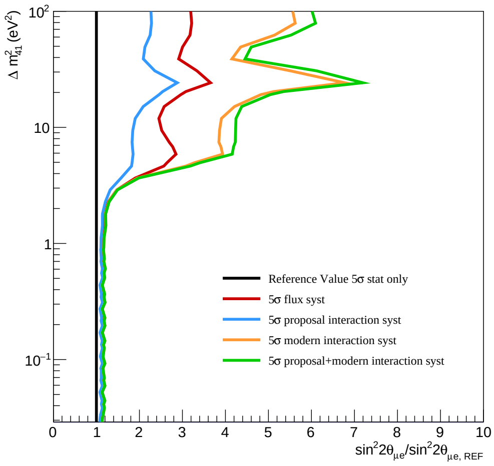

Figure 6.23.: The left plot shows the reduction in sensitivity from the stat-only contour when including each set of systematic parameters in the fits. The right plot shows the relative location of each systematic contour in $\sin^2 2\theta_{\mu e}$ space, with respect to the statistical-only case for the active region of Δm^2_{41} phase space.

The relative contribution of the different systematic groups to the overall exclusion contour for ν_e disappearance is shown in Figure 6.24 and is comparable to the ν_e appearance case. The interaction systematics again have the largest impact the majority of which is due to the modern set of parameters. The proposal set of parameters have the smallest impact with the magnitude of the impact from the flux parameters being somewhere in between the two sets of interaction parameters.

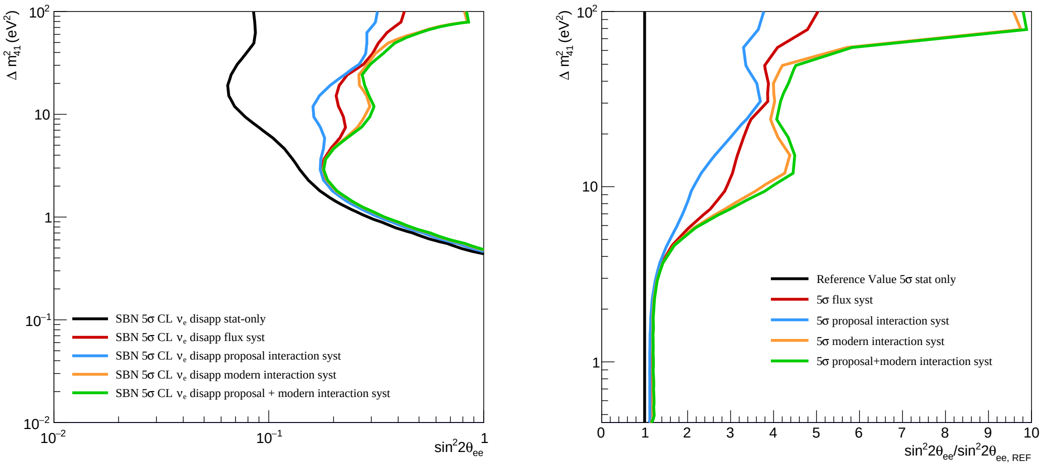

Figure 6.24.: The left plot shows the reduction in sensitivity from the stat-only contour when including each set of systematic parameters in the fits. The right plot shows the relative location of each systematic contour in $\sin^2 2\theta_{ee}$ space, with respect to the statistical-only case for the active region of Δm^2_{41} phase space.

Figure 6.25 shows the change in allowed regions from applying the same set of single systematic parameters for both the ν_e appearance and disappearance channels. Additionally, the allowed region with the inclusion of a single parameter are shown along with the corresponding contour from the entire associated set of systematic paramaters for the ν_e appearance and ν_e disappearance channels in Figure 6.26 and Figure 6.27 respectively.

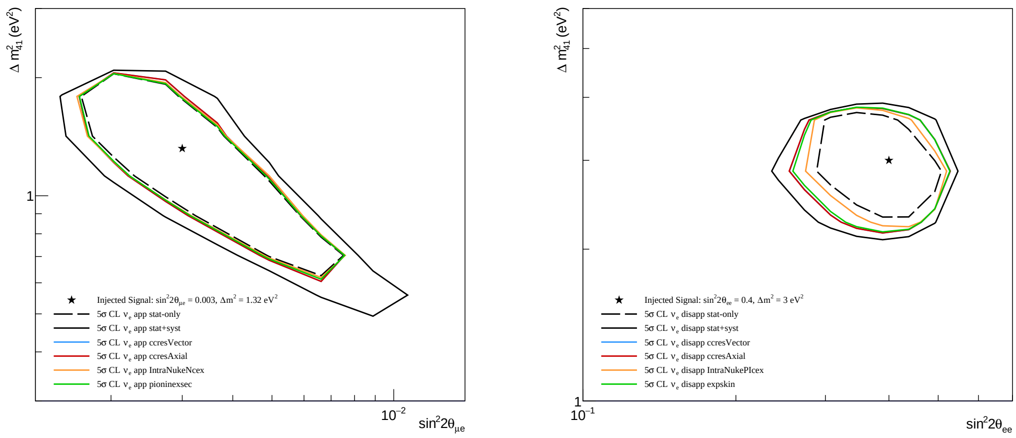

Figure 6.25.: ν_e appearance and disappearance allowed regions with the inclusion of a single systematic parameter at a time. The systematic parameters considered for the ν_e appearance channel are $f_{M_V^{CCRes}}$, $f_{M_A^{CCRes}}$, $f_{R_N^{CEx}}$ and $f_{\sigma^{\pi}_{INEL}}$ (Left) and the systematic parameters considered for the ν_e disappearance channel are $f_{M_V^{CCRes}}$, $f_{M_A^{CCRes}}$, $f_{R_\pi^{CEx}}$ and $f_{expskin}$ (Right).

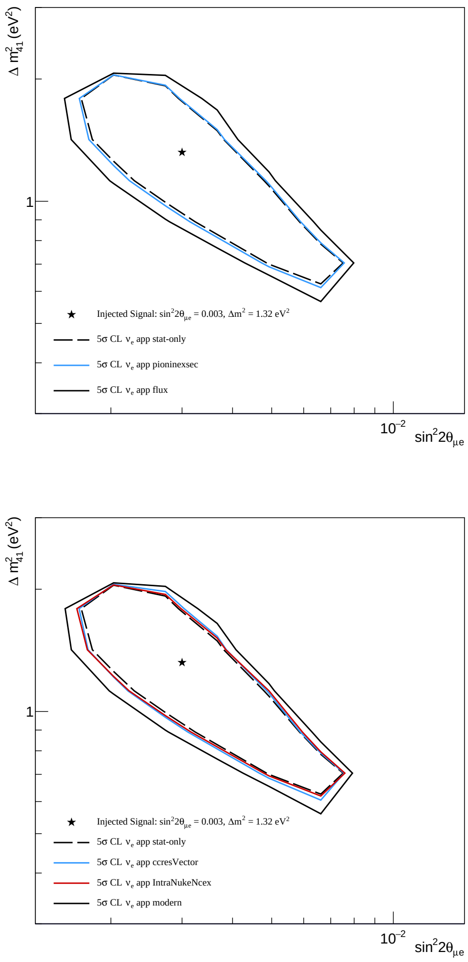

Figure 6.26.: The ν_e appearance allowed region from an injected signal at $\sin^2 2\theta_{\mu e} = 0.003$, $\Delta m^2_{41} = 1.32$ eV^2 showing the impact of the $f_{\sigma^{\pi}_{INEL}}$ compared to the total flux systematics (Top Left), the impact of $f_{M_A^{CCRes}}$ compared to the total proposal systematics (Top Right) and the impact of both $f_{M_V^{CCRes}}$ and $f_{R_\pi^{CEx}}$ on the total modern systematics (Bottom Left). The stat only and total flux + interaction contours have been included for comparison.

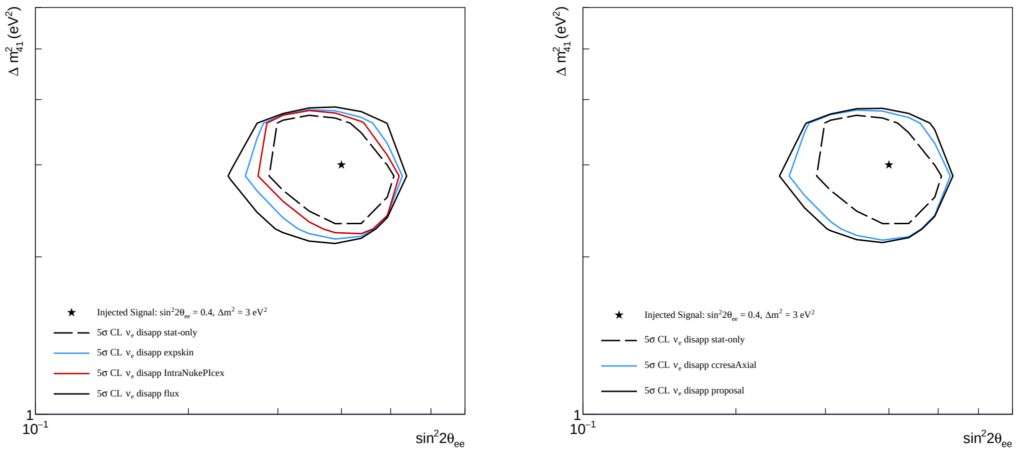

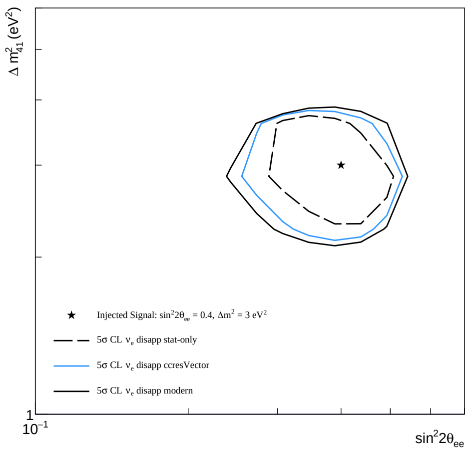

Figure 6.27.: The ν_e disappearance allowed region from an injected signal at $\sin^2 2\theta_{ee} = 0.4$, $\Delta m^2_{41} = 3$ eV^2 showing the impact of the $f_{expskin}$ compared to the total flux systematics (Top Left), the impact of $f_{M_A^{CCRes}}$ compared to the total proposal systematics (Top Right) and the impact of both $f_{M_V^{CCRes}}$ and $f_{R_N^{CEx}}$ on the total modern systematics (Bottom Left). The stat only and total flux + interaction contours have been included for comparison.

6.6.3. Impact of Additional Efficiency Systematics

As was mentioned in Section 5.5.3, efficiency systematics are not currently included in the *standard* analyses. In order to get a measure of the possible impact of efficiency systematics on the sensitivity, various covariance matrices were produced following the scheme outlined in Section 5.5.3. Matrices were produced to investigate the impact of;

1. Fully correlated errors only.
2. Various combinations of uncorrelated errors with a fixed correlated error.
3. Uncorrelated errors only applied to a single detector at a time.
4. A poorly constrained uncorrelated error on a single set of bins.

Unless otherwise stated, the uncertainties from efficiency covariance matrices are applied in addition to the flux and interaction systematics.

The study on the impact of different efficiency uncertainties was first done for the ν_μ disappearance channel because it was expected that there would be a greater impact than for either of the ν_e channels. This is because the typical event rate for the ν_μ channel is several order of magnitude greater than that of ν_e meaning that the ν_μ channel is systematics limited whereas the ν_e channels may tend towards being statistics limited. Once a contour becomes statistics limited, continuing to apply additional systematic uncertainties will begin to have diminishing impacts.

Sensitivities including efficiency uncertainties for the ν_μ disappearance channel are shown alongside the other figures in Appendix D. The impact of the efficiency uncertainties on both ν_e channels is discussed below.

Impact of Efficiency Systematics on ν_e Appearance Sensitivities

In order to gauge the contribution of some typical efficiency uncertainty, Figure 6.28 shows the impact on the ν_e appearance sensitivity from individual sets of systematic parameters as in Figure 6.23 but with the addition of a 2% correlated + 2% uncorrelated efficiency uncertainty. The impact of the efficiency uncertainty is comparable to the proposal interaction systematics having the smallest contribution to the sensitivity.

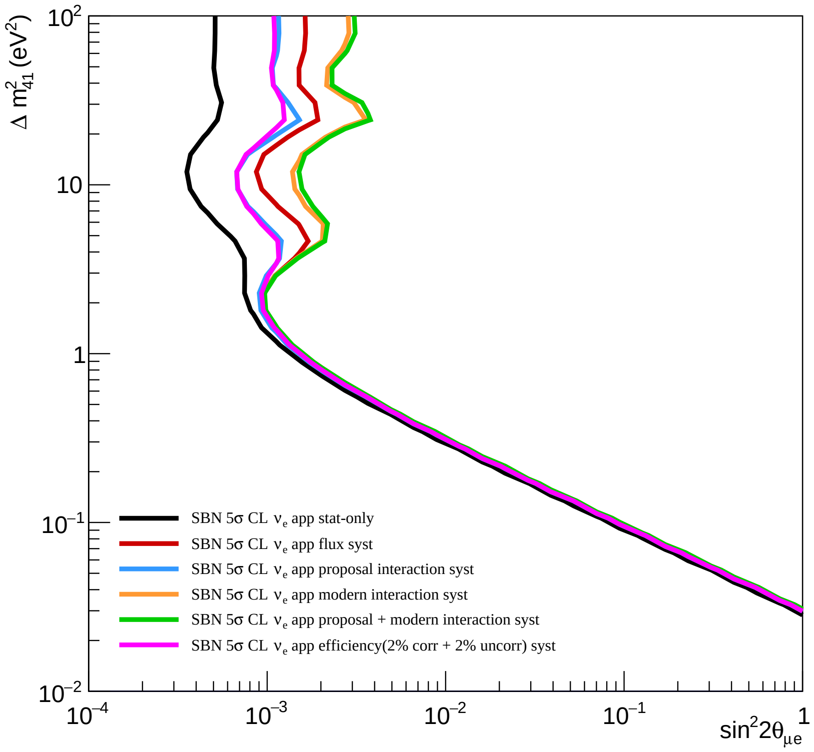

Figure 6.28.: The reduction in the ν_e appearance sensitivity from the stat-only contour when including each set of systematic parameters in the fits. Similar to Figure 6.23 but with the addition of a 2% correlated and 2% uncorrelated efficiency uncertainty.

The reduction in sensitivity from applying a 10% correlated uncertainty and a 2% correlated + 2% uncorrelated uncertainty are shown in Figure 6.29. Since a correlated error of 10% has a close to negligible impact, the results from applying correlated uncertainties less than 10% as was done for the ν_μ channel have been omitted. Similarly, applying smaller uncorrelated uncertainties would again only have a minor impact so these have also been omitted.

Figure 6.30 asses the impact of a 2% uncorrelated uncertainty which is applied to each detector one at a time. Applying the uncertainty to MicroBooNE and ICARUS appears to have a negligible impact across all Δm^2_{41} values. SBND has a

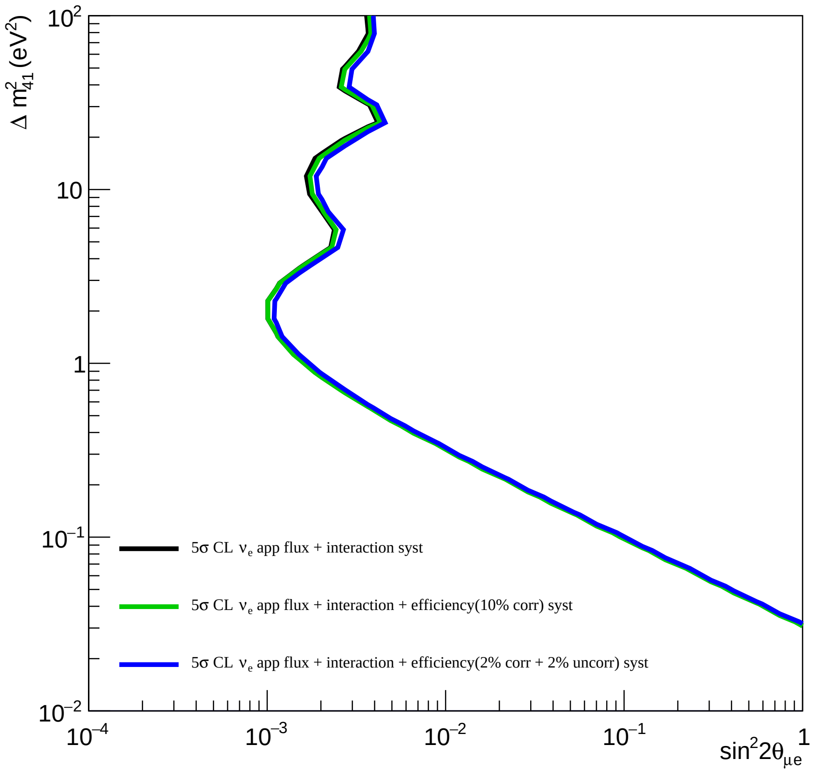

Figure 6.29.: The impact on the ν_e appearance exclusion sensitivity by applying a 10% fully correlated efficiency uncertainty to all bins and by applying 2% fully correlated + 2% uncorrelated efficiency uncertainty.

relatively small impact at high Δm^2_{41} values which resembles the loss in sensitivity that was seen by applying a 2% correlated + 2% uncorrelated uncertainty across all bins in Figure 6.29. It follows that any reduction in sensitivity due to efficiency uncertainties is driven by SBND. Since SBND is most sensitive to large Δm^2_{41} values and has higher statistics than MicroBooNE and ICARUS, the results are consistent with the idea that ν_e channel is close to becoming statistics limited.

Instead of exploring the impact from fully correlated uncertainties or a constant uncorrelated uncertainty across all bins in a detector, Figure 6.31 considers the case where a single set of bins are poorly constrained. The sets of bins considered are,

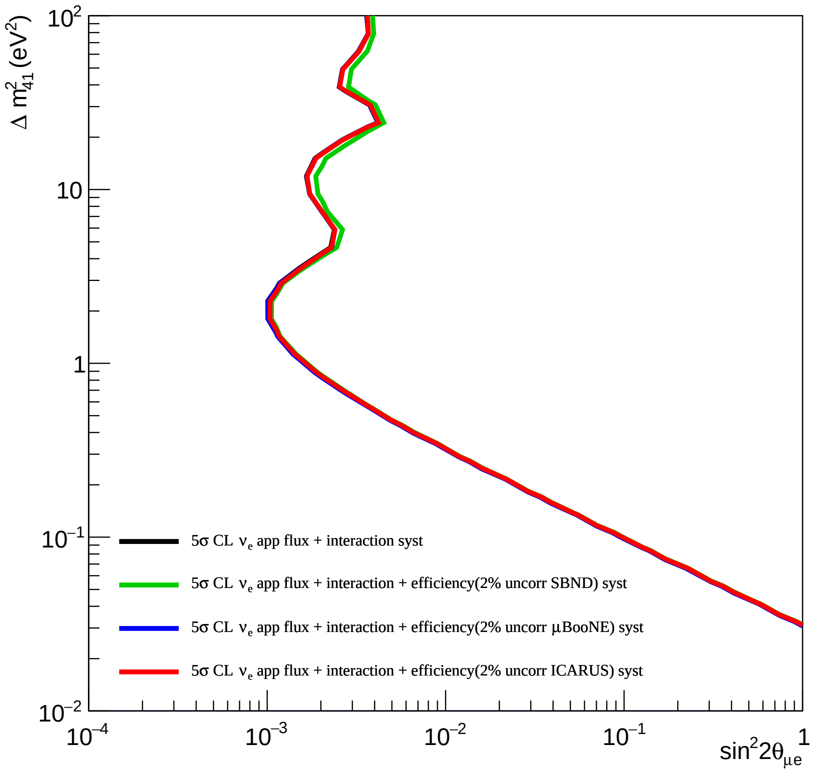

Figure 6.30.: The impact on the ν_e appearance exclusion sensitivity by applying a 2% uncorrelated efficiency uncertainty to a single one of the three SBN detectors.

- CC signal below the peak energy (< 0.6 GeV),
- CC signal at the peak energy ([0.6 - 1.0] GeV),
- CC signal above the peak energy (> 1.0 GeV),
- Background.

In each case, the uncorrelated uncertainty for the bins of interest are set to 2% in each of the SBN detectors, whilst the rest of the uncorrelated uncertainties are set to 0.5% and the fully correlated uncertainty is fixed at 2%. The background and low energy bins have the smallest impact with almost no visible difference whereas the peak and high energy bins do show some small reduction in the sensitivity at Δm^2_{41} greater than 1 eV^2.

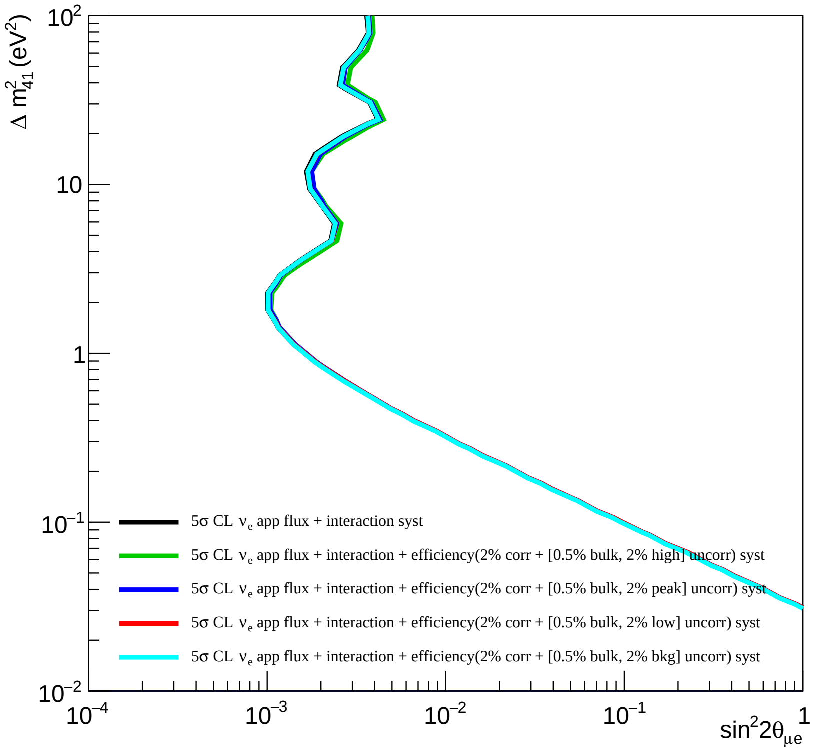

Figure 6.31.: The impact on the ν_e appearance exclusion sensitivity by applying a 2% fully correlated efficiency uncertainty for each of the SBN detectors and a 0.5% uncorrelated uncertainty for all but a single set of bins where the uncorrelated uncertainty is set to 2%. The 'peak' energy bins are defined as those covering an energy range of [0.6, 1.0] GeV. The 'high' and 'low' energy bins are defined as those covering energies above and below the peak energy respectively and the 'bkg' bins are all the bins associated with background events. The set of bins of interest are applied to each of the three detectors.

Impact of Efficiency Systematics on ν_e Disappearance Sensitivities

As was done for ν_e appearance, Figure 6.32 shows the impact from ν_e disappearance sensitivity from individual sets of systematic parameters as in Figure 6.24 but with the addition of a 2% correlated + 2% uncorrelated efficiency uncertainty. The efficiency uncertainty shows the smallest reduction in sensitivity across all ranges of $\Delta m^2_{41} \gtrsim 3$ and is comparable to the other systematic sets at Δm^2_{41} values below ~ 3.

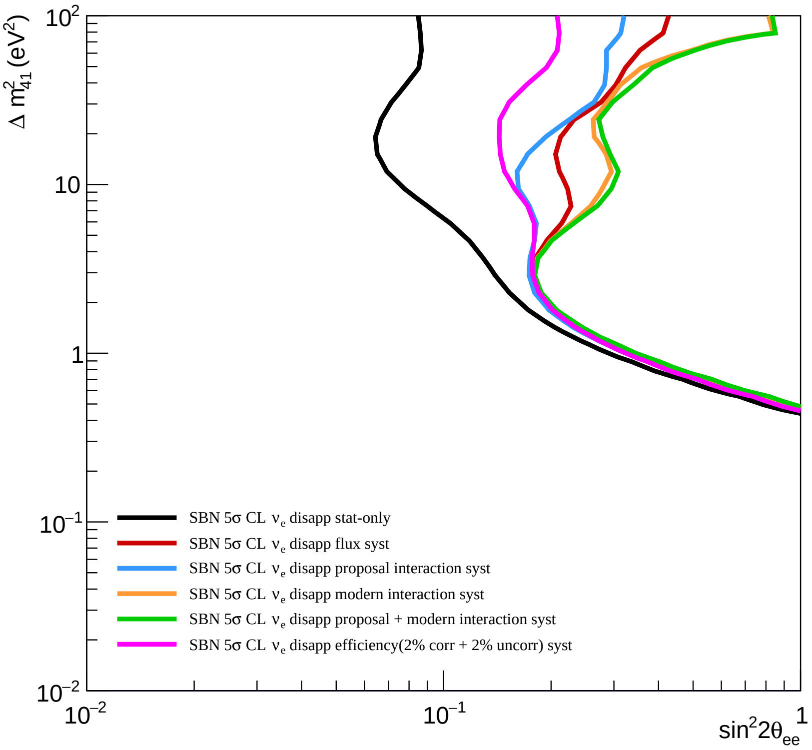

Figure 6.32.: The reduction in the ν_e disappearance sensitivity from the stat-only contour when including each set of systematic parameters in the fits. Similar to Figure 6.24 but with the addition of a 2% correlated and 2% uncorrelated efficiency uncertainty.

Mirroring what was done for ν_e appearance, Figure 6.33 shows the impact of applying a 10% correlated error and a 2% correlated + 2% uncorrelated error. The correlated error again has an almost negligible impact and whilst the uncorrelated error has a larger impact it is still relatively small.

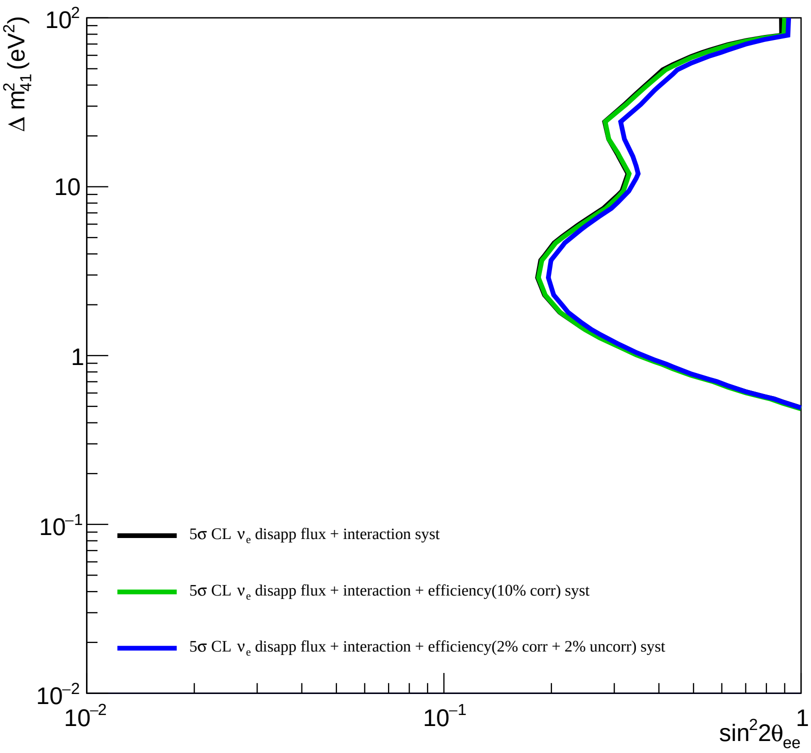

Figure 6.33.: The impact on the ν_e disappearance exclusion sensitivity by applying a 10% fully correlated efficiency uncertainty to all bins and by applying 2% fully correlated + 2% uncorrelated efficiency uncertainty.

A 2% uncorrelated uncertainty is then applied to each detector one at a time. Figure 6.34 shows that majority of the reduction is due to SBND at above $\Delta m^2_{41} \sim 10$ (where SBND is dominant). Both MicroBooNE and ICARUS only have a minimal impact for any Δm^2_{41} values. This is consistent with what is shown in Figure 6.33.

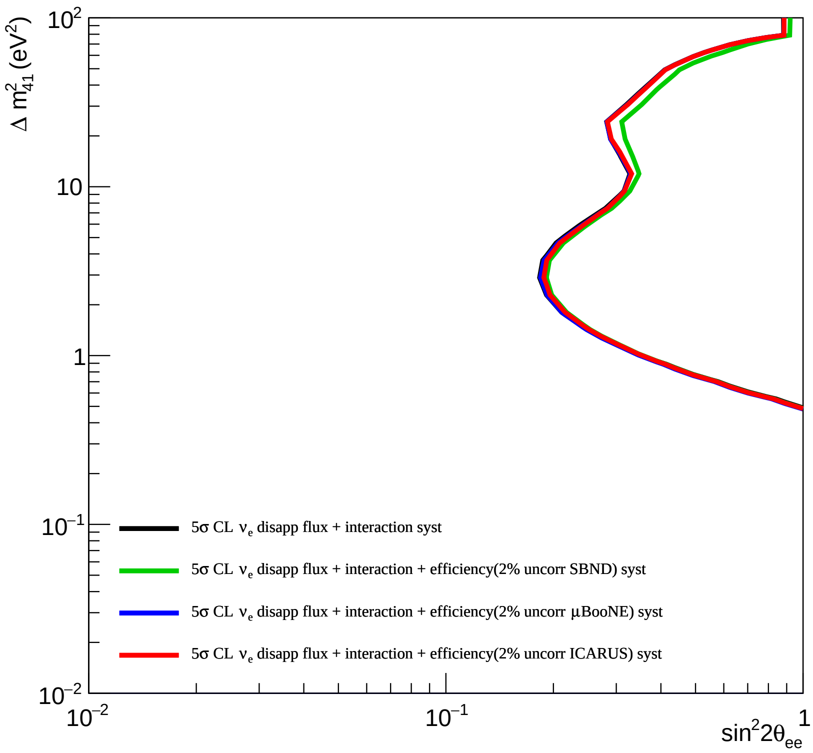

Figure 6.34.: The impact on the ν_e disappearance exclusion sensitivity by applying a 2% uncorrelated efficiency uncertainty to a single one of the three SBN detectors.

Finally, the impact of having a set of poorly constrained bins is investigated in Figure 6.35. Similar to the ν_e appearance case, the low energy and background bins only have a minimal impact, whereas the peak and high energy bins show a slightly larger impact but far less prominent than for the ν_μ channel.

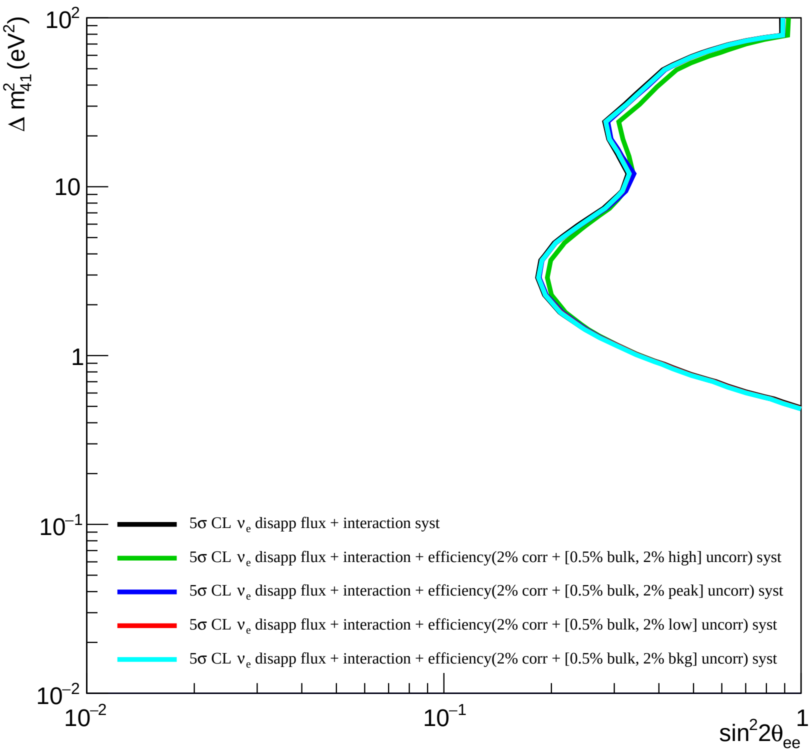

Figure 6.35.: The impact on the ν_e disappearance exclusion sensitivity by applying a 2% fully correlated efficiency uncertainty for each of the SBN detectors and a 0.5% uncorrelated uncertainty for all but a single set of bins where the uncorrelated uncertainty is set to 2%. The 'peak' energy bins are defined as those covering an energy range of [0.6, 1.0] GeV. The 'high' and 'low' energy bins are defined as those covering energies above and below the peak energy respectively and the 'bkg' bins are all the bins associated with background events. The set of bins of interest are applied to each of the three detectors.

6.6.4. Sensitivities Motivated by Shower Energy Reconstruction

The reconstructed neutrino energy used in the analyses shown so far is based on truth information where smearing has been applied to emulate a reconstructed value.

To better motivate the reconstructed energy used, the results from Chapter 4 have been used to tweak the true energy of the showering particles (electrons or photons) to emulate a reconstructed energy based on the reconstruction performance that has been observed with the currently available tools. Since only the reconstructed shower energy was actively investigated here, any non-showering particles continue to have their reconstructed energy estimated by directly smearing the true energy.

The two cases considered for estimating the reconstructed energy of the showering particle are,

- A flat negative bias of 20% is applied to the true energy for all particles.
- A flat negative bias applied to the true energy along with an additional variation to emulate the resolution of the reconstruction performance. The magnitude of the bias and the width of the resolution are functions of the true energy. The resolution was emulated by randomly choosing a number based on a Gaussian with a given standard deviation. The three categories used depending on the true energy are shown in Table 6.6.

E [MeV]	Bias	σ
E $<$ 100	40%	0.15
100 $\leq$ E $<$ 200	30%	0.125
E $>$ 200	20%	0.1

Table 6.6.: The variable bias and resolution used to emulate reconstructed energy.

The simplistic approach of applying a flat 20% bias was motivated by the conservative results from Figure 4.6 which shows that the typical bias is of order 20%. The more involved process of applying an energy dependent bias and resolution are motivated by Figure 4.15. It can be seen that above energies of $\sim$200 MeV, the bias and standard deviation remain fairly constant, but at energies below this, the bias and resolution increase as the energy decreases.

The full ν_e event selection as described in Section 5.3.2 was repeated but with the above changes applied. The events from these selections were then used to produce exclusion contours using the same systematic uncertainties as previously described. The overall event rate from the selections using the reconstructed information motivated by Chapter 4 is lower than than the traditional method which relied on energy smearing.

The exclusion contours comparing the three selections are shown on the left of Figure 6.36 and Figure 6.37 for ν_e appearance and disappearance respectively. The difference between the three exclusion contours is relatively minor and therefore the ratios of the contours to the contour from the original selection are shown on the right of their respective figures. Since the event rate is reduced in the updated selections, it is expected that the overall exclusion sensitivity would also be reduced. This indeed the case for most values of Δm^2_{41} with only a couple of areas where the selection with the flat 20% bias appears to improve the sensitivity.

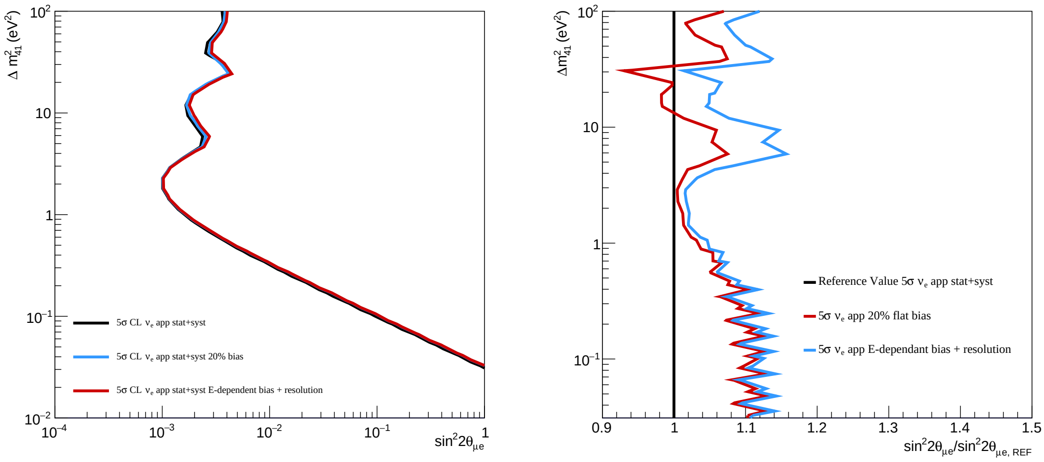

Figure 6.36.: Left: ν_e appearance exclusion contours with flux and interaction uncertainties using events from the original selection and the ones motivated by results from EM shower reconstruction. Right: The ratio of the exclusion contours to the contour from the original selection.

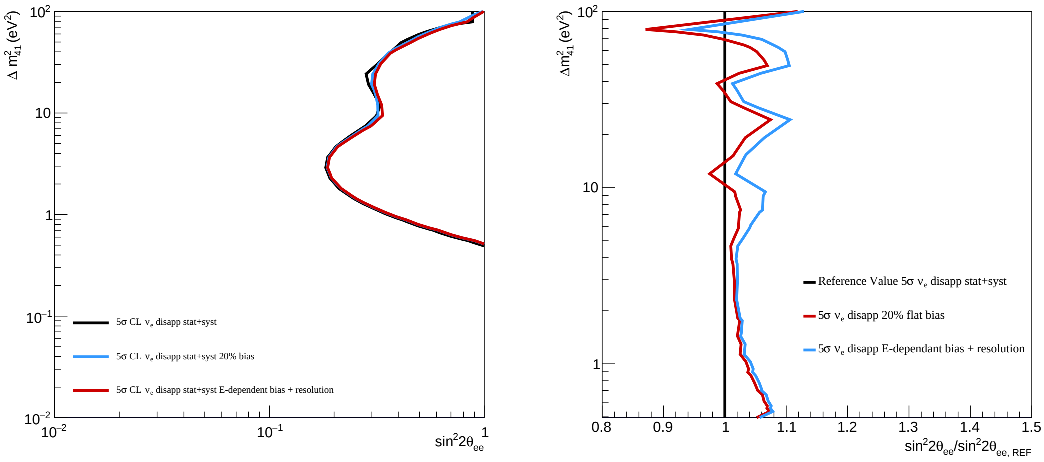

Figure 6.37.: Left: ν_e disappearance exclusion contours with flux and interaction uncertainties using events from the original selection and the ones motivated by results from EM shower reconstruction. Right: The ratio of the exclusion contours to the contour from the original selection.

Chapter 7.

Conclusion

The three SBN detectors are expected to provide a rich physics programme, with the main aims being to confirm or refute the possible existence of light sterile neutrinos, investigate neutrino-argon interactions and to develop large scale LArTPC technologies. Both the MicroBooNE and ICARUS detectors are currently taking data and the full SBN program is expected to come online in early 2024 once SBND is ready to also take data.

In this thesis, the development of two new EM shower reconstruction algorithms have been presented along with the necessary inputs and results from an oscillation analysis within SBN. The oscillation analysis focuses on the ν_e appearance and disappearance channels and uses a modern set of inputs which better reflect the actual SBN program and the relevant physics than what was used in the SBN proposal.

Both the *Shower Num Electrons Energy tool* and the *Shower ESTAR Energy tool* have been newly developed to work within SBND. The *Shower Num Electrons Energy tool* uses a nominal recombination factor and the pre-existing calibration within SBND that allows for the conversion of charge in ADC units to the number of electrons. This approach is much more flexible to physics changes than the previous algorithm, the *Shower Linear Energy tool*, which relied on in-house calibration curves produced from MIP muons. The *Shower ESTAR Energy tool* combines the modified box recombination model with the ESTAR database provided by NIST. This allows for the creation of a lookup curve relating the number of electrons to energy. In both tools, the charge associated with the hits is found and converted to energy using the respective method and the energy of all the hits is summed to find the total energy of the shower. All the reconstruction algorithms have been validated against truth information using events across the energy spectrum of the BNB. Assuming a 1σ hit width when calculating the true energy of the hits, it has been demonstrated that the *Shower ESTAR Energy tool* shows minimal bias in the reconstructed energy. The *Shower Num Electrons Energy tool* systematically applies a larger energy to all of the hits and therefore tends to overestimate the reconstructed hit energy. When comparing with the true energy of the showering particle, all methods underestimate the energy due to hit reconstruction inefficiencies and the expectation of an overall bias. The bias observed by *Shower ESTAR Energy tool* is of the order -20% and since the *Shower Num Electrons Energy tool* applies higher energies to the hits, the bias is a little smaller at around the -10% level.

The oscillation analysis was initially performed in order to recreate the work done in the SBN proposal with an updated and better motivated set of inputs. The focus was on using a ν_e CC inclusive sample as part of a (3+1) neutrino framework where both the ν_e appearance and disappearance channels were considered independently. Exclusion contours as well as allowed regions from an injected signal at $\sin^2 2\theta_{\mu e} = 0.003$, $\Delta m^2_{41} = 1.32$ eV^2 for the appearance channel and $\sin^2 2\theta_{ee} = 0.4$, $\Delta m^2_{41} = 3$ eV^2 for the disappearance channel have been created at the 5σ confidence level. The degradation in the sensitivities due to the inclusion of various efficiency uncertainties on top of the flux and interaction systematics have been investigated. It was shown that any uncorrelated efficiencies dominate the correlated component. On the whole, the impact from efficiency uncertainties on the sensitivity from either ν_e channel is relatively minor with the most significant contribution occurring for large Δm^2_{41} values where SBND is dominant.

Going forward, the oscillation analysis will be performed using a fully reconstructed MC sample (once it has been sufficiently completed) instead of using the current pseudo-reconstruction. The option to produce joint fits is also currently being developed which should provide an improvement to the sensitivities. Finally, the possibility of using exclusive samples instead of the CC-inclusive one are being investigated.

Appendix A.

Single Parameter Variations

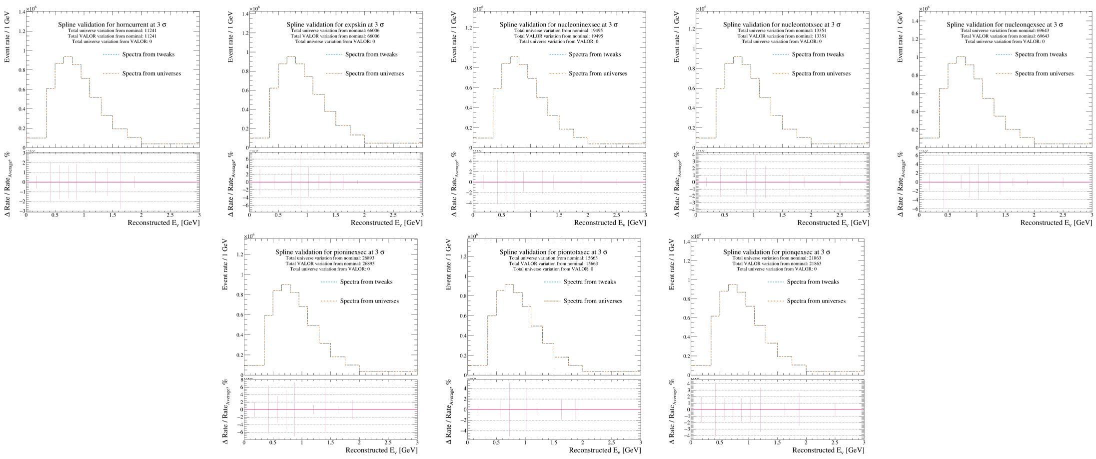

Figure A.1.: A comparison of the $+3\sigma$ variations from the response functions used by VALOR and the universes for the complete set of uncorrelated flux systematic parameters.

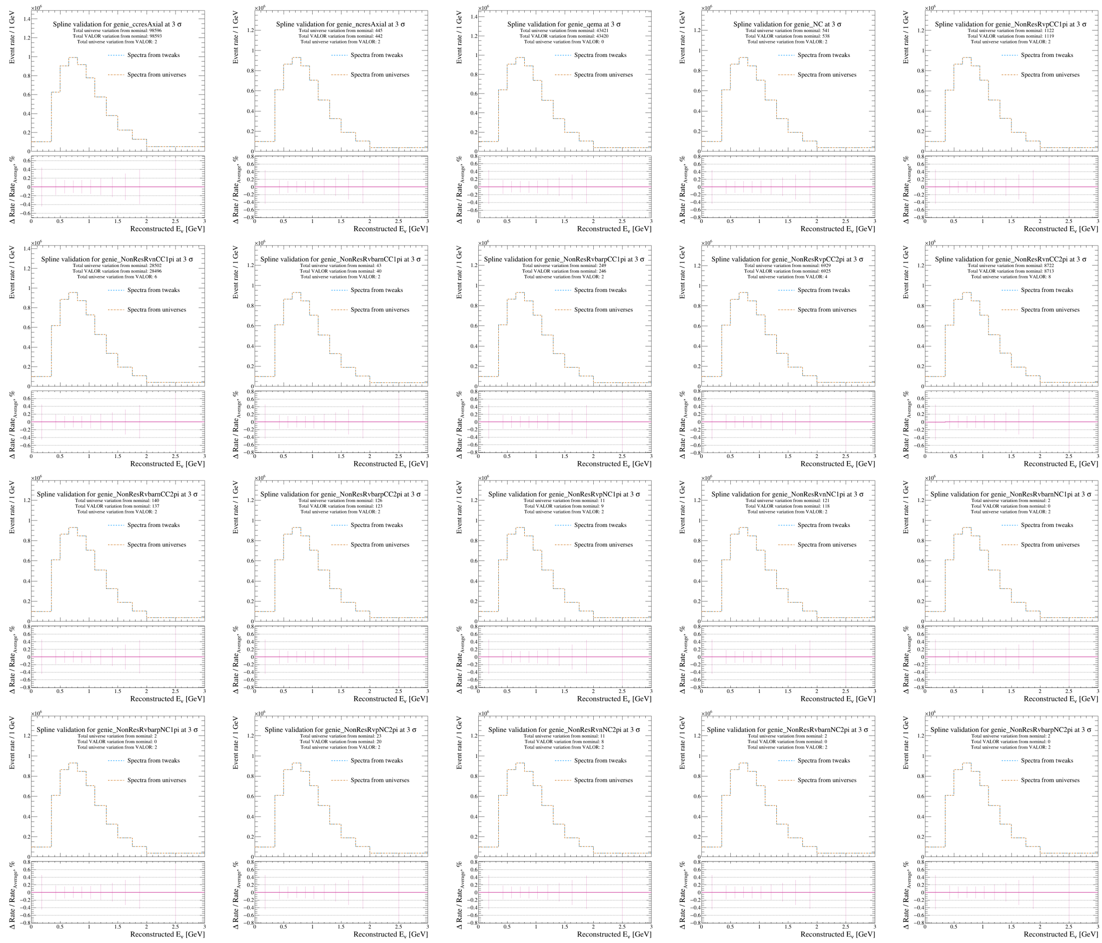

Figure A.2.: A comparison of the $+3\sigma$ variations from the response functions used by VALOR and the universes for the complete set of proposal interaction systematic parameters.

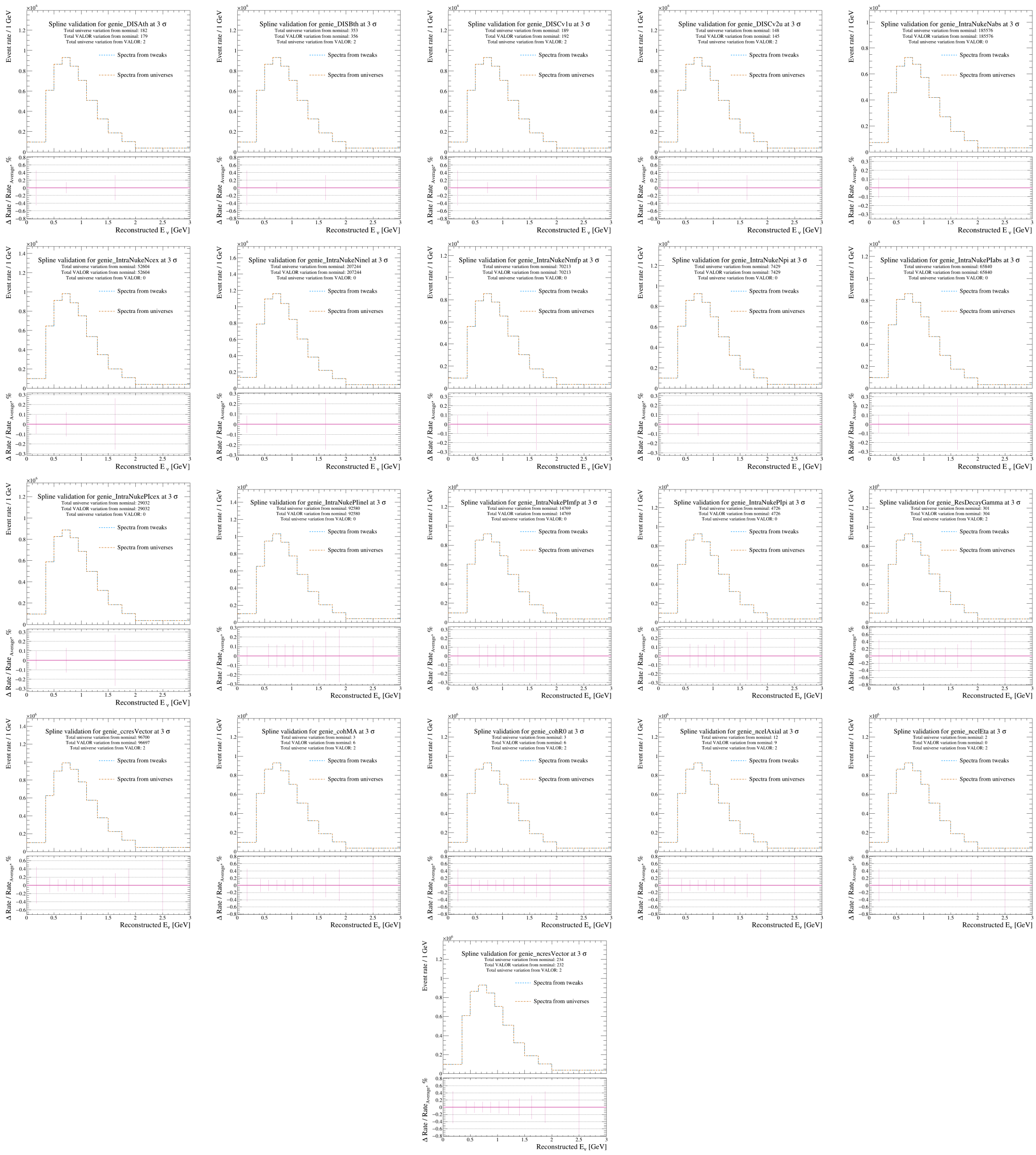

Figure A.3.: A comparison of the $+3\sigma$ variations from the response functions used by VALOR and the universes for the complete set of modern cross-section systematic parameters.

Appendix B.

Detector Volumes

	X [cm]	Y [cm]	Z [cm]
	Active Volume		
SBND	-199.15 – 199.15	-200.00 – 200.00	0.00 – 500.00
MicroBooNE	-1.55 – 254.80	-115.53 – 117.47	0.10 – 1036.90
ICARUS Module 1	-364.49 – -67.94	-173.41 – 143.41	-909.95 – 879.95
ICARUS Module 2	67.94 – 364.49	-173.41 – 143.41	-909.95 – 879.95
	Fiducial Volume		
SBND TPC 1	-190.90 – 5.60	-185.00 – 185.00	15.00 – 415.00
SBND TPC 2	10.90 – 190.90	-185.00 – 185.00	15.00 – 415.00
MicroBooNE	-1.55 – 229.80	-90.53 – 92.47	30.10 – 986.90
ICARUS TPC 1	-339.49 – -221.04	-148.41 – 118.41	-879.95 – 829.95
ICARUS TPC 2	-218.89 – -92.94	-148.41 – 118.41	-879.95 – 829.95
ICARUS TPC 3	92.94 – 211.39	-148.41 – 118.41	-879.95 – 829.95
ICARUS TPC 4	214.39 – 339.39	-148.41 – 118.41	-879.95 – 829.95

Table B.1.: The dimensions defining the active and fiducial volumes for each SBN detector using their respective coordinate systems.

Appendix C.

Reconstruction Performance

The figures in Chapter 4 showing the reconstruction performance were produced whilst running Pandora in cheating mode in order to decouple the reconstruction methods from inefficiencies within the pattern recognition. If Pandora is instead used without cheating mode enabled, the resolution of the reconstruction algorithms is expected to worsen owing to the fact that the number of hits associated with true and reconstructed information is no longer in perfect agreement.

With cheating mode no longer enabled in Pandora, the true vs reconstructed energy is shown for all three planes using the ESTAR method in Figure C.1. The fractional resolution from the collection plane is shown in Figure C.2 for all three reconstruction methods.

Comparing Figure C.1 to the ESTAR plot in Figure 4.4 and Figure 4.9, it can be seen that the resolution has degraded by disabling cheating mode in Pandora. Similarly, in Figure C.2, each of the distributions has a noticeable tail in the negative x-direction which isn't present in the distributions shown in Figure 4.6.

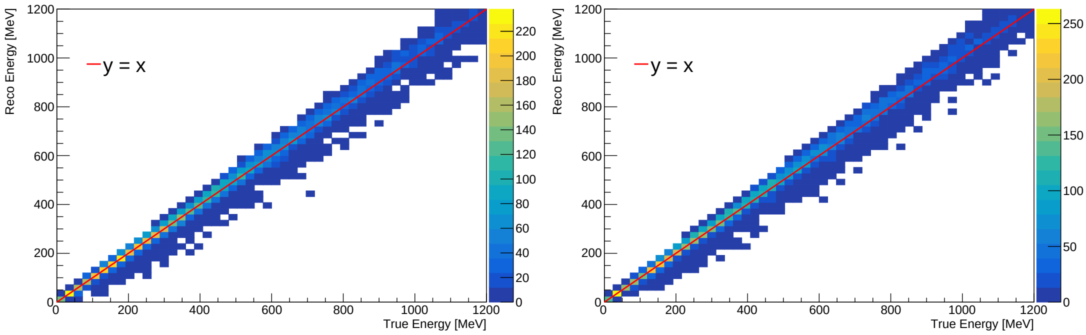

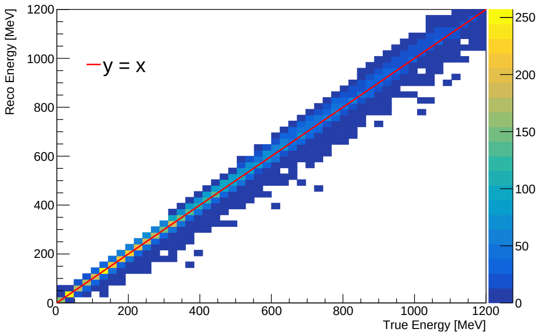

Figure C.1.: True vs reconstructed energy from a showering electron. The true energy has been evaluated from the hits of each shower. Pandora was not run in cheating mode. Top Left: Induction plane 0, Top Right: Induction plane 1 and Bottom Left: Collection plane.

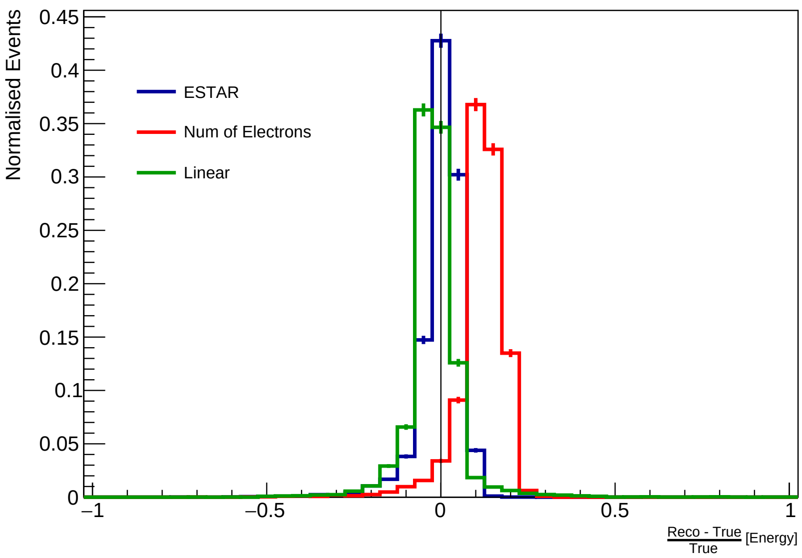

Figure C.2.: Comparison of the fractional energy resolution from a showering electron for the Shower Linear Energy tool, the Shower Num Electrons Energy tool and the Shower ESTAR Energy tool. The true energy is taken to be the true energy of the available hits and for the reconstruction, Pandora was run whilst not in cheating mode.

Appendix D.

ν_μ Disappearance Analysis

A similar analysis and validation to that described in Chapter 6 that was performed for the two ν_e channels was also done for the ν_μ disappearance channel.

The nominal event rate breakdown for each of the detectors is shown in Figure D.1 where an integrated spectrum with oscillation parameters $\sin^2 2\theta_{\mu\mu} = 0.072$, $\Delta m^2_{41} = 1.32$ eV^2 has been overlayed. The overall magnitude of the event rate is several order of magnitude greater than that for ν_e owing to the fact that the BNB consists predominantly of ν_μ. As was the case for ν_e disappearance, the reduction in events for SBND is relatively small whereas for MicroBooNE and ICARUS it is much more significant.

The complete ν_μ disappearance exclusion sensitivities and allowed regions for both the statistical only case and with the inclusion of flux and interaction systematics are shown in Figure D.2 for the entire SBN program alongside external limits from the combined results from SciBooNE and MiniBooNE, IceCube, MINOS and its successor MINOS+ [105] [107] [48] [119]. The results for the SBN program are shown at a 5σ confidence level whereas the exclusion region from the SciBooNE/MiniBooNE, IceCube and MINOS/MINOS+ experiments are shown at the 90% confidence. The IceCube experiment also shows an allowed region at the 99% confidence level. The results from SBN show a stronger sensitivity to that obtained by MiniBooNE/SciBooNE for all mass splitting values. The exclusion contour is also comparable to that from MINOS/MINOS+ for $\Delta m^2_{41} \gtrsim 1$ eV^2, however below this value MINOS/MINOS+ provides a stronger limit. The exclusion contour from IceCube again provides a stronger limit at $\Delta m^2_{41} \lesssim 1$ eV^2, but for higher values, SBN expects to improve on the results from IceCube. The allowed region from IceCube intersect the one from SBN so they aren't fully compatible.

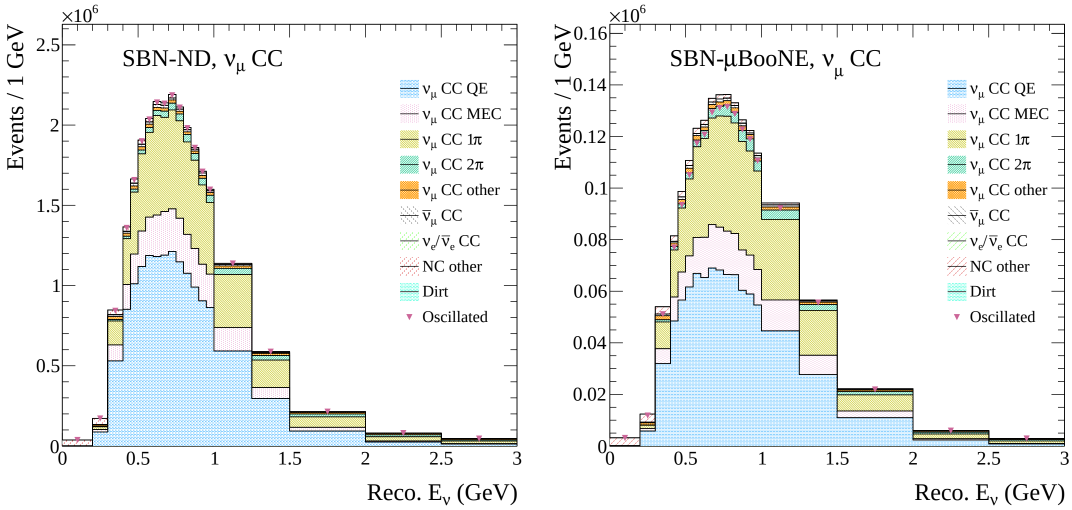

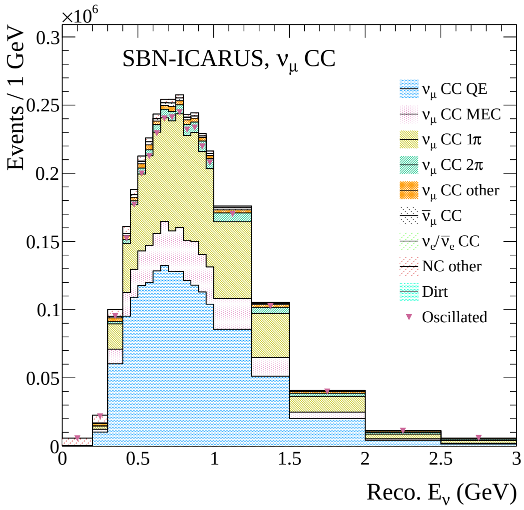

Figure D.1.: The breakdown of the nominal ν_μ disappearance spectra overlayed with an integrated oscillated spectrum with oscillation parameters, $\sin^2 2\theta_{\mu\mu} = 0.072$ and $\Delta m^2_{41} = 1.32$ eV^2 showing the decrease in event rate.

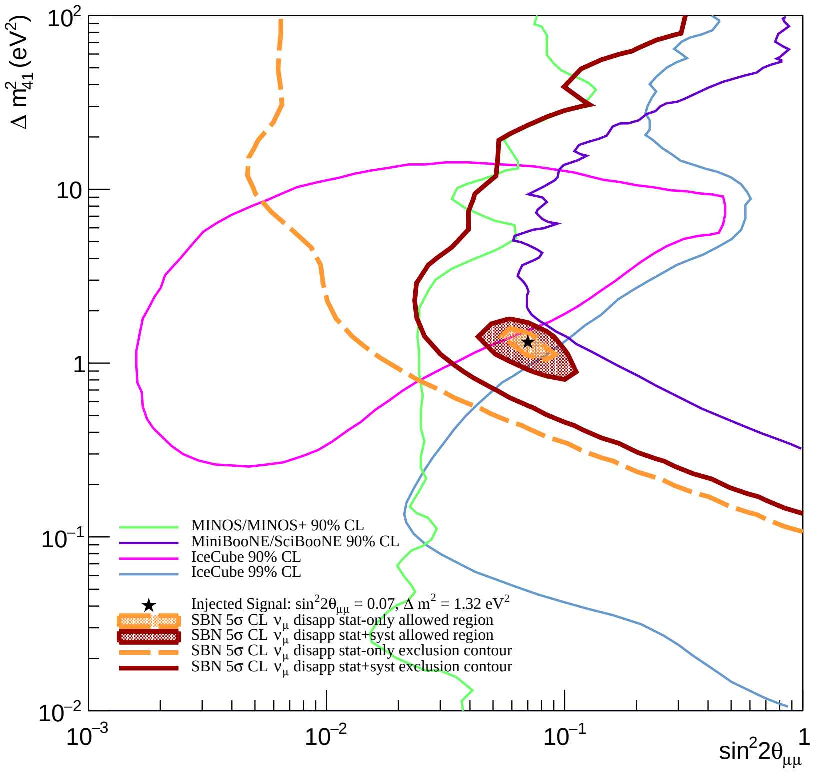

Figure D.2.: ν_μ disappearance exclusion contours and allowed regions for the stat only case and with flux and interaction systematic uncertainties included. External limits from the MiniBooNE/SciBooNE, MINOS/MINOS+ and IceCube experiments have been overlayed [105] [106] [107]. (The confidence intervals for each contour are shown in the legend and it should be noted that those from external limits are not the same as those from the contours produced for the SBN program.)

Impact of Efficiency Systematics on ν_μ Disappearance Sensitivities

The impact of fully correlated uncertainties up to 10% are shown on the left of Figure D.3 whilst keeping the uncorrelated uncertainty at 0%. The right plot shows the impact of increasing the uncorrelated uncertainties uniformly across all bins with a fixed correlated uncertainty of 2%. It follows that for even relatively large correlated uncertainties the impact on the sensitivity is minor and that any reduction in sensitivities will be largely dominated by the uncorrelated uncertainty.

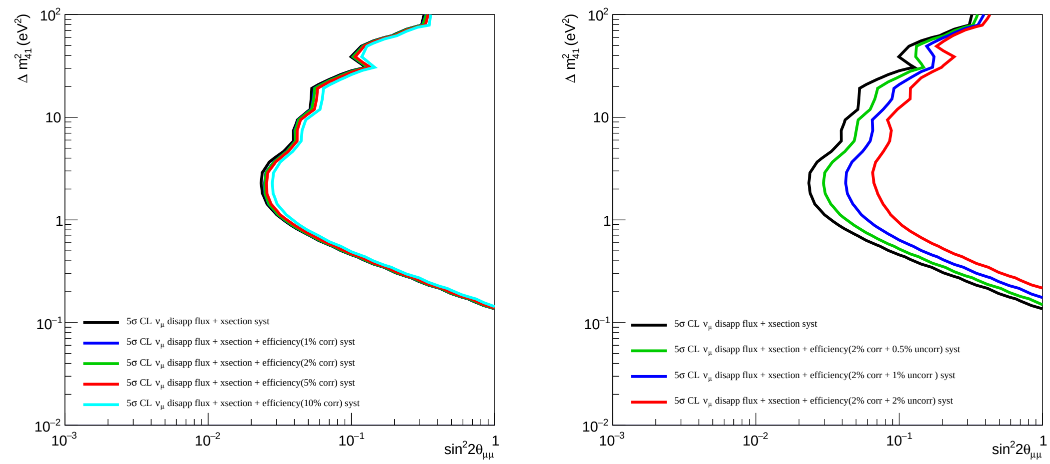

Figure D.3.: The impact on the ν_μ disappearance exclusion sensitivity by applying fully correlated uncertainties ranging from 1% to 10% to all bins (Left) and by applying a fixed 2% fully correlated uncertainty with additional uncorrelated uncertainty ranging from 0.5% to 2% across all bins (Right).

Figure D.4 shows the impact of applying a 2% uncorrelated uncertainty only to each of the SBN detectors one at a time. The MicroBooNE detector has a minor impact at around $\Delta m^2_{41} = 10$ eV^2 and close to no impact at small and large Δm^2_{41} values. The ICARUS detector has a larger impact for most Δm^2_{41} values but again only has a minor contribution at very large Δm^2_{41} values. Across most Δm^2_{41} values greater than ~ 0.5 eV^2, SBND dominates the sensitivity. At values below 0.5 eV^2 the reduction in sensitivity due to SBND and ICARUS are comparable. This point is emphasised in Figure D.5 where the fully correlated uncertainty is fixed at 2% and the uncorrelated uncertainty is set to 2% for one of the three SBN detectors whilst being set to 0.5% for the other two detectors. The contour where SBNDs uncorrelated uncertainty is set to 2% looks similar to the corresponding contour in Figure D.4. It has been shown that the uncorrelated component of the uncertainty has a large impact when compared to the correlated component and that any efficiency uncertainties impact SBND more than the other two detectors so this result ought to be expected. Similarly, the two contours where uncorrelated uncertainty is set to 2% for MicroBooNE and ICARUS are pulled towards the SBND contour since despite it having a smaller associated uncorrelated uncertainty, it will still contribute significantly.

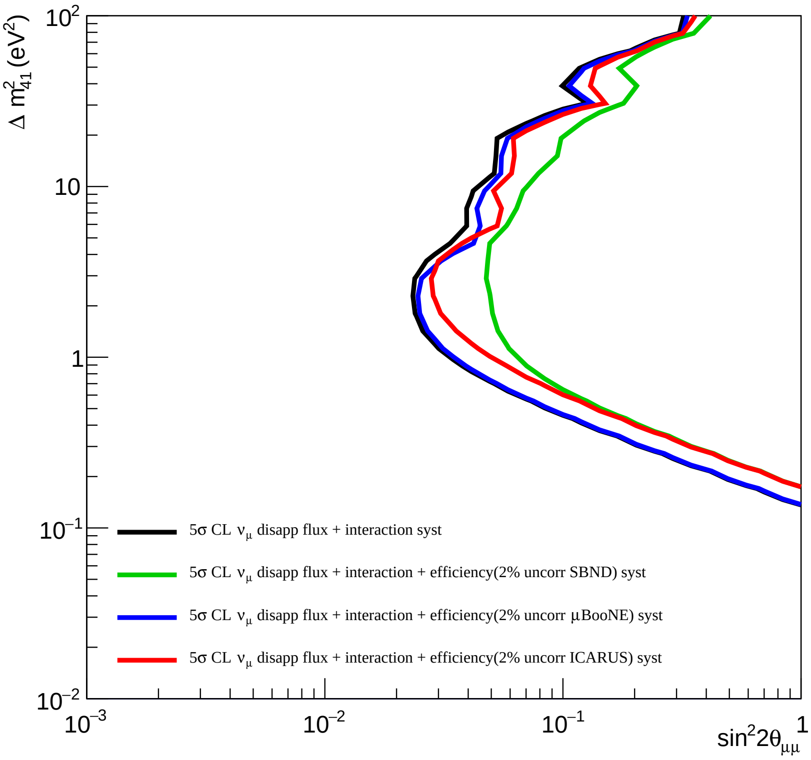

Figure D.4.: The impact on the ν_μ disappearance exclusion sensitivity by applying a 2% uncorrelated efficiency uncertainty to a single one of the three SBN detectors.

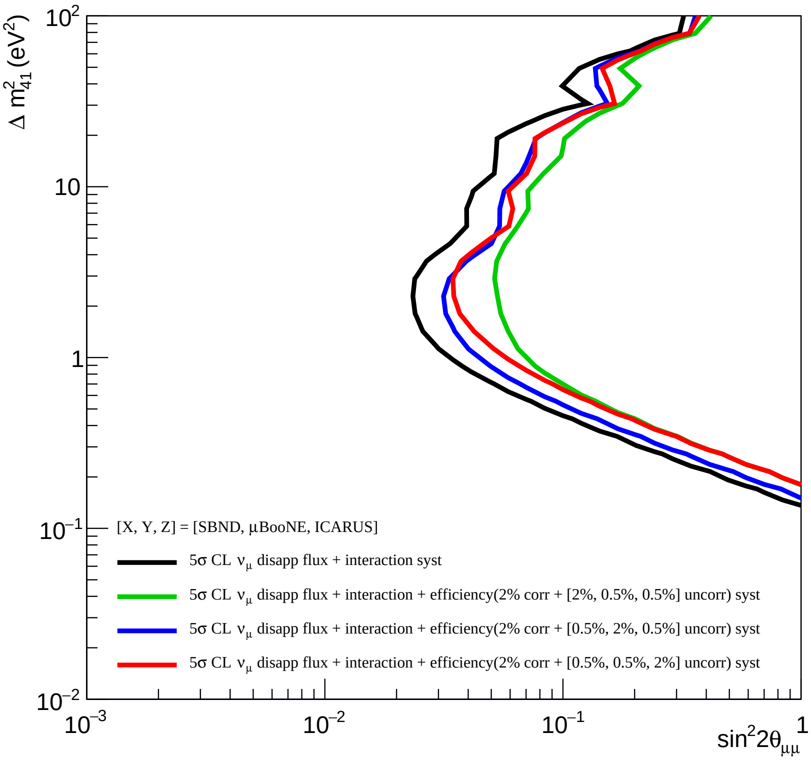

Figure D.5.: The impact on the ν_μ disappearance exclusion sensitivity by applying a 2% fully correlated efficiency uncertainty for each of the SBN detectors and a 2% uncorrelated uncertainty for one of detectors and a 0.5% uncorrelated uncertainty for the other two detectors. This is repeated for each of the detectors. The associated covariance matrix used for the case where SBNDs uncorrelated uncertainty was set to 2% is shown in the bottom left plot of Figure 5.2.

Figure D.6 considers the case where a single set of bins are poorly constrained using the same scheme outlined in Section 6.6.3. In each case, the uncorrelated uncertainty for the bins of interest are again set to 2% in each of the SBN detectors, whilst the rest of the uncorrelated uncertainties are set to 0.5% and the fully correlated uncertainty is fixed at 2%. Increasing the uncertainty associated with the background bins has the smallest impact whereas increasing the uncertainty for the high and low energy bins has the largest impact at large and small Δm^2_{41} respectively. The peak energy bins also contribute significantly around Δm^2_{41} equal to 1 eV^2 and 10 eV^2.

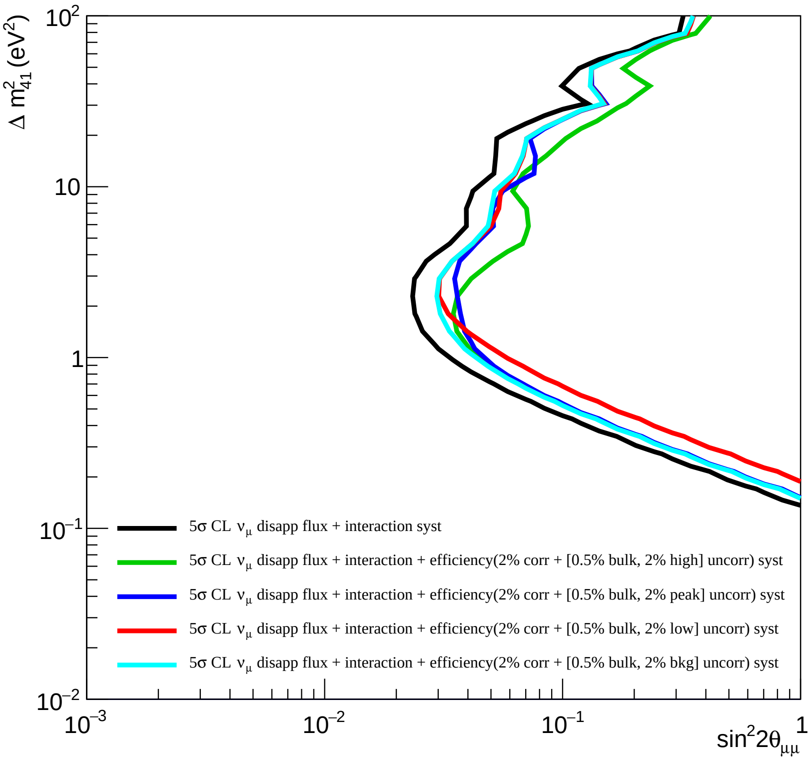

Figure D.6.: The impact on the ν_μ disappearance exclusion sensitivity by applying a 2% fully correlated efficiency uncertainty for each of the SBN detectors and a 0.5% uncorrelated uncertainty for all but a single set of bins where the uncorrelated uncertainty is set to 2%. The 'peak' energy bins are defined as those covering an energy range of [0.6, 1.0] GeV. The 'high' and 'low' energy bins are defined as those covering energies above and below the peak energy respectively and the 'bkg' bins are all the bins associated with background events. The set of bins of interest are applied to each of the three detectors and the covariance matrix for where the peak energy bins are the ones in question is shown in the bottom right plot of Figure 5.2.

Colophon

This thesis was made in $\LaTeX\,2_\varepsilon$ using the “hepthesis” class.

Bibliography

[1] S. Braibant, G. Giacomelli, and M. Spurio, *Particles and Fundamental Interactions: An Introduction to Particle Physics* Undergraduate Lecture Notes in Physics (Springer Netherlands, 2011).

[2] W. Pauli, Pauli letter collection: letter to Lise Meitner, https://cds.cern.ch/record/83282, Typed copy, [Accessed September 2021].

[3] C. L. Cowan, Jr., F. Reines, F. B. Harrison, H. W. Kruse, and A. D. McGuire, Detection of the Free Neutrino: A Confirmation, doi:10.1126/science.124.3212.103, Science **124**, 103 (1956).

[4] G. Danby *et al.*, Observation of High-Energy Neutrino Reactions and the Existence of Two Kinds of Neutrinos, doi:10.1103/PhysRevLett.9.36, Physical Review Letters **9**, 36 (1962).

[5] DONUT, K. Kodama *et al.*, Observation of tau neutrino interactions, doi:10.1016/S0370-2693(01)00307-0, Phys. Lett. **B504**, 218 (2001), hep-ex/0012035.

[6] Y. Fukuda *et al.*, Evidence for Oscillation of Atmospheric Neutrinos, doi:10.1103/physrevlett.81.1562, Physical Review Letters **81**, 1562–1567 (1998).

[7] K. Lande *et al.*, Results from the Homestake solar neutrino observatory, Conf. Proc. **C900802**, 867 (1990), [Conf. Proc.C900802V1,C900802V1:667(1990)].

[8] Super-Kamiokande, J. G. Learned, The Atmospheric neutrino anomaly: Muon neutrino disappearance, p. 89 (2000), hep-ex/0007056.

[9] W. Rodejohann, Neutrino-less Double Beta Decay and Particle Physics, doi:10.1142/s0218301311020186, International Journal of Modern Physics E **20**, 1833 (2011).

[10] K. N. Abazajian *et al.*, Light Sterile Neutrinos: A White Paper, FERMILAB-PUB-12-881-PPD, arXiv:1204.5379, 2012, 1204.5379.

[11] LAr1-ND, ICARUS-WA104, MicroBooNE, M. Antonello *et al.*, A Proposal for a Three Detector Short-Baseline Neutrino Oscillation Program in the Fermilab Booster Neutrino Beam, arXiv:1503.01520, 2015, 1503.01520.

[12] A. Schukraft, SBND Project Overview: progress, schedule and resources, https://sbn-docdb.fnal.gov/cgi-bin/sso/ShowDocument?docid=26247, 2022, [Accessed: Aug, 2022].

[13] P. A. Machado, O. Palamara, and D. W. Schmitz, The Short-Baseline Neutrino Program at Fermilab, doi:10.1146/annurev-nucl-101917-020949, Annual Review of Nuclear and Particle Science **69**, 363–387 (2019).

[14] M. L. Perl *et al.*, Evidence for Anomalous Lepton Production in $e^+ - e^-$ Annihilation, doi:10.1103/PhysRevLett.35.1489, Phys. Rev. Lett. **35**, 1489 (1975).

[15] A. Blondel, The Number of Neutrinos and the Z Line Shape, doi:10.1142/9789814733519_0008, (2016).

[16] ALEPH, D. Decamp *et al.*, Determination of the Number of Light Neutrino Species, doi:10.1016/0370-2693(89)90704-1, Phys. Lett. B **231**, 519 (1989).

[17] LSND Collaboration, A. Aguilar *et al.*, Evidence for neutrino oscillations from the observation of $\overline{\nu}_e$ appearance in a $\overline{\nu}_\mu$ beam, doi:10.1103/PhysRevD.64.112007, Phys. Rev. D **64**, 112007 (2001).

[18] MiniBooNE Collaboration, A. A. Aguilar-Arevalo *et al.*, Significant Excess of Electron like Events in the MiniBooNE Short-Baseline Neutrino Experiment, doi:10.1103/PhysRevLett.121.221801, Phys. Rev. Lett. **121**, 221801 (2018).

[19] GALLEX, W. Hampel *et al.*, Final results of the Cr-51 neutrino source experiments in GALLEX, doi:10.1016/S0370-2693(97)01562-1, Phys. Lett. B **420**, 114 (1998).

[20] F. Kaether, W. Hampel, G. Heusser, J. Kiko, and T. Kirsten, Re-analysis of the Gallex solar neutrino flux and source experiments, doi:https://doi.org/10.1016/j.physletb.2010.01.030, Physics Letters B **685**, 47 (2010).

[21] J. N. Abdurashitov *et al.*, Measurement of the response of a Ga solar neutrino experiment to neutrinos from a ^{37}Ar source, doi:10.1103/PhysRevC.73.045805, Phys. Rev. C **73**, 045805 (2006).

[22] G. Mention *et al.*, Reactor antineutrino anomaly, doi:10.1103/physrevd.83.073006, Physical Review D **83** (2011).

[23] E. Majorana, A Symmetric Theory of Electrons and Positrons, in *Scientific Papers of Ettore Majorana: A New Expanded Edition*, edited by L. Cifarelli, pp. 113–128, Springer International Publishing, Cham, 2020.

[24] T. Morii , C. S. Lim , S. N. Mukherjee, *The Physics Of The Standard Model And Beyond* (World Scientific Publishing Co. Pte. Ltd., 2004).

[25] W. H. Furry, On Transition Probabilities in Double Beta-Disintegration, doi:10.1103/PhysRev.56.1184, Phys. Rev. **56**, 1184 (1939).

[26] V. Barger, D. Marfatia, and K. Whisnant, *The Physics of Neutrinos* (Princeton University Press, 2012).

[27] B. R. Martin and G. Shaw, *Particle Physics, Third Edition* (John Wiley and Sons, Ltd, Publication, 2008).

[28] M. Goldhaber, L. Grodzins, and A. W. Sunyar, Helicity of Neutrinos, doi:10.1103/PhysRev.109.1015, Phys. Rev. **109**, 1015 (1958).

[29] Alessandro De Angelis, Mário Pimenta, *Introduction to Particle and Astroparticle Physics: Multimessenger Astronomy and its Particle Physics Foundations*, second ed. (Springer International Publishing AG, 2018).

[30] C. Giunti and C. W. Kim, *Fundamentals of Neutrino Physics and Astrophysics.* (Oxford: Oxford University Press, 2007).

[31] Particle Data Group, R. L. Workman and Others, Review of Particle Physics: Particle Detectors for Non-Accelerator Physics, doi:10.1093/ptep/ptac097, PTEP **2022**, 083C01 (2022).

[32] C. S. Wu, E. Ambler, R. W. Hayward, D. D. Hoppes, and R. P. Hudson, Experimental Test of Parity Conservation in Beta Decay, doi:10.1103/PhysRev.105.1413, Physical Review **105**, 1413 (1957).

[33] J. H. Christenson, J. W. Cronin, V. L. Fitch, and R. Turlay, Evidence for the 2π Decay of the K_2^0 Meson, doi:10.1103/PhysRevLett.13.138, Phys. Rev. Lett. **13**, 138 (1964).

[34] A. D. Sakharov, Violation of CP invariance, C asymmetry, and baryon asymmetry of the universe, doi:10.1070/pu1991v034n05abeh002497, Soviet Physics Uspekhi **34**, 392 (1991).

[35] G. C. Branco, R. G. Felipe, and F. R. Joaquim, Leptonic CP Violation, doi:10.1103/RevModPhys.84.515, Rev. Mod. Phys. **84**, 515 (2012), 1111.5332.

[36] F. Halzen and A. Martin, *Quarks and Leptons: An Introductory Course in Modern Particle Physics* (John Wiley, New York, 1984).

[37] B. Pontecorvo, Neutrino Experiments and the Problem of Conservation of Leptonic Charge, Zh. Eksp. Teor. Fiz. **53**, 1717 (1967).

[38] Z. Maki, M. Nakagawa, and S. Sakata, Remarks on the Unified Model of Elementary Particles, doi:10.1143/PTP.28.870, Progress of Theoretical Physics **28**, 870 (1962), https://academic.oup.com/ptp/article-pdf/28/5/870/5258750/28-5-870.pdf.

[39] Y. Chan, RESULTS FROM SNO, https://www.osti.gov/servlets/purl/822831, 2001, DOE Contract No. DE-AC03-76SF00098.

[40] SNO Collaboration, Q. R. Ahmad *et al.*, Measurement of the Rate of $\nu_e + d \to p + p + e^-$ Interactions Produced by ^8B Solar Neutrinos at the Sudbury Neutrino Observatory, doi:10.1103/PhysRevLett.87.071301, Phys. Rev. Lett. **87**, 071301 (2001).

[41] Particle Data Group, P. Zyla *et al.*, Review of Particle Physics, doi:10.1093/ptep/ptaa104, PTEP **2020**, 083C01 (2020).

[42] X. Qian and P. Vogel, Neutrino mass hierarchy, doi:10.1016/j.ppnp.2015.05.002, Progress in Particle and Nuclear Physics **83**, 1–30 (2015).

[43] R. N. Cahn *et al.*, White Paper: Measuring the Neutrino Mass Hierarchy, doi:10.48550/ARXIV.1307.5487, 2013.

[44] L. Wolfenstein, Neutrino oscillations in matter, doi:10.1103/PhysRevD.17.2369, Phys. Rev. D **17**, 2369 (1978).

[45] S. Parke, Determining the Neutrino Mass Hierarchy, 2006, FERMILAB-CONF-06-248-T.

[46] A. Diaz, C. Argüelles, G. Collin, J. Conrad, and M. Shaevitz, Where are we with light sterile neutrinos?, doi:10.1016/j.physrep.2020.08.005, Physics Reports **884**, 1 (2020).

[47] KARMEN, K. Eitel, KARMEN: Present neutrino oscillation limits and perspectives after the upgrade, in *32nd Rencontres de Moriond: Electroweak Interactions and Unified Theories*, pp. 267–274, 1997, hep-ex/9706023.

[48] MINOS Collaboration, P. Adamson *et al.*, Search for Sterile Neutrinos Mixing with Muon Neutrinos in MINOS, doi:10.1103/PhysRevLett.117.151803, Phys. Rev. Lett. **117**, 151803 (2016).

[49] J. Kostensalo, J. Suhonen, C. Giunti, and P. Srivastava, The gallium anomaly revisited, doi:https://doi.org/10.1016/j.physletb.2019.06.057, Physics Letters B **795**, 542 (2019).

[50] Micheal E. Peskin and Daniel V. Schroeder, *An Introduction to Quantum Field Theory* (Perseus Books Publishing, 1995).

[51] C. Rubbia, The Liquid Argon Time Projection Chamber: A New Concept for Neutrino Detectors, (1977).

[52] W. Walkowiak, Drift velocity of free electrons in liquid argon, doi:https://doi.org/10.1016/S0168-9002(99)01301-7, Nuclear Instruments and Methods in Physics Research Section A: Accelerators, Spectrometers, Detectors and Associated Equipment **449**, 288 (2000).

[53] R. Acciarri *et al.*, Design and Construction of the MicroBooNE Detector, doi:10.1088/1748-0221/12/02/P02017, Journal of Instrumentation **12** (2016).

[54] M. Schenk, *Studies with a Liquid Argon Time Projection Chamber: Addressing Technological Challenges of Large-Scale Detectors* BestMaster, 1 ed. (Springer Specktrum, 2015).

[55] Y. Li *et al.*, Measurement of longitudinal electron diffusion in liquid argon, doi:10.1016/j.nima.2016.01.094, Nuclear Instruments and Methods in Physics Research Section A: Accelerators, Spectrometers, Detectors and Associated Equipment **816**, 160–170 (2016).

[56] C. Anderson *et al.*, The ArgoNeuT detector in the NuMI low-energy beam line at Fermilab, doi:10.1088/1748-0221/7/10/p10019, Journal of Instrumentation **7**, P10019–P10019 (2012).

[57] MicroBooNE, A Measurement of the Attenuation of Drifting Electrons in the MicroBooNE LArTPC, doi:10.2172/1573054, (2017).

[58] G. Jaffé, Zur Theorie der Ionisation in Kolonnen, doi:https://doi.org/10.1002/andp.19133471205, Annalen der Physik **347**, 303 (1913), https://onlinelibrary.wiley.com/doi/pdf/10.1002/andp.19133471205.

[59] J. Thomas and D. A. Imel, Recombination of electron-ion pairs in liquid argon and liquid xenon, doi:10.1103/PhysRevA.36.614, Phys. Rev. A **36**, 614 (1987).

[60] M. Mooney, The MicroBooNE Experiment and the Impact of Space Charge Effects, doi:10.48550/ARXIV.1511.01563, 2015.

[61] S. Palestini and K. Mcdonald, Space charge in ionization detectors, https://physics.princeton.edu/examples/spacecharge.pdf, 2016, [Accessed: August, 2022].

[62] V. Shiltsev, Fermilab Proton Accelerator Complex Status and Improvement Plans, doi:10.1142/S0217732317300129, Mod. Phys. Lett. A **32**, 1730012 (2017), 1705.03075.

[63] SciBooNE, A. A. Aguilar-Arevalo *et al.*, Bringing the SciBar detector to the booster neutrino beam, (2006), hep-ex/0601022.

[64] MiniBooNE Collaboration, A. A. Aguilar-Arevalo *et al.*, Neutrino flux prediction at MiniBooNE, doi:10.1103/PhysRevD.79.072002, Phys. Rev. D **79**, 072002 (2009).

[65] C. E. Patrick, *Measurement of the Antineutrino Double-Differential Charged-Current Quasi-Elastic Scattering Cross Section at MINERvA* (Springer International Publishing, Cham, 2018).

[66] E. Scantamburlo, *Measurement of the Water to Scintillator Charged-Current Cross-Section Ratio for Muon Neutrinos at the T2K Near Detector*, PhD thesis, UNIVERSITÉ DE GENÈVE, 2017, Presented 06 Jun 2017.

[67] M. Acero *et al.*, Adjusting neutrino interaction models and evaluating uncertainties using NOvA near detector data, doi:10.1140/epjc/s10052-020-08577-5, The European Physical Journal C **80** (2020).

[68] T. Van Cuyck, N. Jachowicz, R. González-Jiménez, J. Ryckebusch, and N. Van Dessel, Seagull and pion-in-flight currents in neutrino-induced $1n$ and $2n$ knockout, doi:10.1103/PhysRevC.95.054611, Phys. Rev. C **95**, 054611 (2017).

[69] K. Majumdar and K. Mavrokoridis, Review of Liquid Argon Detector Technologies in the Neutrino Sector, doi:10.3390/app11062455, Applied Sciences **11**, 2455 (2021).

[70] M. Auger *et al.*, A novel cosmic ray tagger system for liquid argon tpc neutrino detectors, doi:10.48550/ARXIV.1612.04614, 2016.

[71] C. Adams *et al.*, Design and construction of the MicroBooNE Cosmic Ray Tagger system, doi:10.1088/1748-0221/14/04/p04004, Journal of Instrumentation **14**, P04004–P04004 (2019).

[72] A. Machado and E. Segreto, ARAPUCA a new device for liquid argon scintillation light detection, doi:10.1088/1748-0221/11/02/c02004, Journal of Instrumentation **11**, C02004 (2016).

[73] A. Machado *et al.*, The X-ARAPUCA: an improvement of the ARAPUCA device, doi:10.1088/1748-0221/13/04/c04026, Journal of Instrumentation **13**, C04026–C04026 (2018).

[74] R. Acciarri *et al.*, Design and construction of the MicroBooNE detector, doi:10.1088/1748-0221/12/02/p02017, Journal of Instrumentation **12**, P02017–P02017 (2017).

[75] Sandbox Studio, Chicago, Schematic of the ICARUS detector., https://www.symmetrymagazine.org/article/sterile-neutrino-sleuths, [Accessed: January, 2022].

[76] ICARUS Collaboration, C. Rubbia and C. S. Montanari, Status and plans of WA104/ICARUS, CERN-SPSC-2017-012, SPSC-SR-207, https://cds.cern.ch/record/2256748, 2017.

[77] C. Frugiuele, Probing sub-GeV dark sectors via high energy proton beams at LBNF/DUNE and MiniBooNE, doi:10.1103/PhysRevD.96.015029, Phys. Rev. D **96**, 015029 (2017).

[78] P. Ballett, S. Pascoli, and M. Ross-Lonergan, MeV-scale sterile neutrino decays at the Fermilab Short-Baseline Neutrino program, doi:10.1007/jhep04(2017)102, Journal of High Energy Physics **2017** (2017).

[79] E. Bertuzzo, S. Jana, P. A. N. Machado, and R. Zukanovich Funchal, Dark Neutrino Portal to Explain MiniBooNE Excess, doi:10.1103/PhysRevLett.121.241801, Phys. Rev. Lett. **121**, 241801 (2018).

[80] A. P. Furmanski and C. Hilgenberg, Neutrino energy estimation in neutral current interactions and prospects for sterile neutrino searches, doi:10.1103/PhysRevD.103.112011, Phys. Rev. D **103**, 112011 (2021).

[81] C. Andreopoulos *et al.*, The GENIE Neutrino Monte Carlo Generator, doi:10.1016/j.nima.2009.12.009, Nucl. Instrum. Meth. A **614**, 87 (2010), 0905.2517.

[82] GEANT4 A Simulation Toolkit, https://geant4.web.cern.ch/, [Accessed August, 2022].

[83] S. Agostinelli *et al.*, Geant4—a simulation toolkit, doi:https://doi.org/10.1016/S0168-9002(03)01368-8, Nuclear Instruments and Methods in Physics Research Section A: Accelerators, Spectrometers, Detectors and Associated Equipment **506**, 250 (2003).

[84] MicroBooNE, R. Acciarri *et al.*, The Pandora multi-algorithm approach to automated pattern recognition of cosmic-ray muon and neutrino events in the MicroBooNE detector, doi:10.1140/epjc/s10052-017-5481-6, Eur. Phys. J. C **78**, 82 (2018), 1708.03135.

[85] LArSoft, https://larsoft.org/, [Accessed: July, 2022].

[86] E. L. Snider and G. Petrillo, LArSoft: Toolkit for Simulation, Reconstruction and Analysis of Liquid Argon TPC Neutrino Detectors, doi:10.1088/1742-6596/898/4/042057, J. Phys. Conf. Ser. **898**, 042057 (2017).

[87] T. Usher, GausHitFinder Hit Finding and Fitting, https://indico.fnal.gov/event/18523/contributions/47921 /attachments/29850/36753/GaussHitFinder121118.pdf, 2018, [Accessed: July, 2022].

[88] R. Acciarri *et al.*, A study of electron recombination using highly ionizing particles in the ArgoNeuT Liquid Argon TPC, doi:10.1088/1748-0221/8/08/p08005, Journal of Instrumentation **8**, P08005–P08005 (2013).

[89] C. Adams *et al.*, Reconstruction and measurement of $\mathcal{O}(100)$ MeV energy electromagnetic activity from $\pi^0 \to \gamma\gamma$ decays in the MicroBooNE

LArTPC, doi:10.1088/1748-0221/15/02/p02007, Journal of Instrumentation **15**, P02007–P02007 (2020).

[90] E. Tyley, SBND Recombination Study for Shower Calorimetry, https://sbn-docdb.fnal.gov/cgi-bin/sso/ShowDocument?docid=12033, 2019, [Accessed: July, 2022].

[91] R. Acciarri *et al.*, Demonstration of MeV-scale physics in liquid argon time projection chambers using ArgoNeuT, doi:10.1103/PhysRevD.99.012002, Phys. Rev. D **99**, 012002 (2019).

[92] M. Berger, J. Coursey, M. Zucker, and J. Chang, ESTAR, PSTAR, and ASTAR: Computer Programs for Calculating Stopping-Power and Range Tables for Electrons, Protons, and Helium Ions (version 2.0.1)., http://physics.nist.gov/Star, National Institute of Standards and Technology, Gaithersburg, MD., [Accessed: September, 2021].

[93] GENIE, L. Alvarez-Ruso *et al.*, Recent highlights from GENIE v3, doi:10.1140/epjs/s11734-021-00295-7, Eur. Phys. J. ST **230**, 4449 (2021), 2106.09381.

[94] GENIE, J. Tena-Vidal *et al.*, Neutrino-nucleon cross-section model tuning in GENIE v3, doi:10.1103/PhysRevD.104.072009, Phys. Rev. D **104**, 072009 (2021), 2104.09179.

[95] D. Schmitz, SBND POT and Event Estimates, https://sbn-docdb.fnal.gov/cgi-bin/sso/ShowDocument?docid=27405, 2022, [Accessed: Aug, 2022].

[96] A. Ankowski *et al.*, Measurement of through-going particle momentum by means of multiple scattering with the ICARUS T600 TPC, doi:10.1140/epjc/s10052-006-0051-3, The European Physical Journal C - Particles and Fields **48**, 667 (2006).

[97] D. Barker, *Developments Towards a ν_e CC Sterile Appearance Sensitivity in the Short-Baseline Neutrino Programme*, PhD thesis, uk.bl.ethos.832514, University of Sheffield, 2020.

[98] C. Andreopoulos *et al.*, The GENIE Neutrino Monte Carlo Generator: Physics and User Manual, 2015, 1510.05494.

[99] MicroBooNE Collaboration, Booster Neutrino Flux Prediction at MicroBooNE, doi:10.2172/1573216, (2018).

[100] C. Andreopoulos *et al.*, The VALOR Group, https://valor.pp.rl.ac.uk.

[101] C. Andreopoulos *et al.*, VALOR DUNE Joint Oscillation and Systematics Constraint Fit (Version 2016a v2), DUNE DocID 1291, 2016.

[102] P. G. Hoel, *Introduction to Mathematical Statistics*, Fourth ed. (John Wiley & Sons, 1971).

[103] G. Cowan, K. Cranmer, E. Gross, and O. Vitells, Asymptotic formulae for likelihood-based tests of new physics, doi:10.1140/epjc/s10052-011-1554-0, The European Physical Journal C **71** (2011).

[104] G. Karagiorgi and J. Zennamo, SBND Oscillations Working Group Kick-off, https://sbn-docdb.fnal.gov/cgi-bin/sso/ShowDocument?docid=27844, 2022, [Accessed: Oct, 2022].

[105] K. B. M. Mahn *et al.*, Dual baseline search for muon neutrino disappearance at $0.5\text{eV}^2 < \Delta m^2 < 40\text{eV}^2$, doi:10.1103/physrevd.85.032007, Physical Review D **85** (2012).

[106] P. Adamson *et al.*, Search for Sterile Neutrinos in MINOS and MINOS+ Using a Two-Detector Fit, doi:10.1103/physrevlett.122.091803, Physical Review Letters **122** (2019).

[107] M. Aartsen *et al.*, Searching for eV-scale sterile neutrinos with eight years of atmospheric neutrinos at the IceCube Neutrino Telescope, doi:10.1103/physrevd.102.052009, Physical Review D **102** (2020).

[108] MiniBooNE, A. A. Aguilar-Arevalo *et al.*, Improved Search for $\bar{\nu}_\mu \to \bar{\nu}_e$ Oscillations in the MiniBooNE Experiment, doi:10.1103/PhysRevLett.110.161801, Phys. Rev. Lett. **110**, 161801 (2013), 1303.2588.

[109] M. Antonello *et al.*, Experimental search for the "LSND anomaly" with the ICARUS detector in the CNGS neutrino beam, doi:10.1140/epjc/s10052-013-2345-6, The European Physical Journal C **73** (2013).

[110] KARMEN, B. Armbruster *et al.*, Upper limits for neutrino oscillations $\bar{\nu}_\mu \to \bar{\nu}_e$ from muon decay at rest, doi:10.1103/PhysRevD.65.112001, Phys. Rev. D **65**, 112001 (2002), hep-ex/0203021.

[111] P. Astier *et al.*, Search for $\nu_\mu \to \nu_e$ oscillations in the NOMAD experiment, doi:10.1016/j.physletb.2003.07.029, Physics Letters B **570**, 19 (2003).

[112] OPERA Collaboration *et al.*, Search for $\nu_\mu \to \nu_e$ oscillations with the OPERA experiment in the CNGS beam, doi:10.48550/ARXIV.1303.3953, (2013).

[113] L. Borodovsky *et al.*, Search for Muon-Neutrino Oscillations $\nu_\mu \to \nu_e$ ($\bar{\nu}_\mu \to \bar{\nu}_e$) in a Wide-Band Neutrino Beam, doi:10.1103/PhysRevLett.68.274, Phys. Rev. Lett. **68**, 274 (1992).

[114] M. Dentler *et al.*, Updated global analysis of neutrino oscillations in the presence of eV-scale sterile neutrinos, doi:10.1007/jhep08(2018)010, Journal of High Energy Physics **2018** (2018).

[115] K. Abe *et al.*, Search for short baseline ν_e disappearance with the T2K near detector, doi:10.1103/physrevd.91.051102, Physical Review D **91** (2015).

[116] R. Jones, *Muon-neutrino disappearance with multiple liquid argon time projection chambers in the Fermilab Booster neutrino beam*, PhD thesis, doi:10.17638/03143192, University of Liverpool, 2021.

[117] A. G. Frodesen, O. Skjeggestad, H. Tøfte, *PROBABILITY AND STATISTICS IN PARTICLE PHYSICS* (Columbia University Press, 1979).

[118] K. Abe *et al.*, The T2K experiment, doi:https://doi.org/10.1016/j.nima.2011.06.067, Nuclear Instruments and Methods in Physics Research Section A: Accelerators, Spectrometers, Detectors and Associated Equipment **659**, 106 (2011).

[119] MINOS+, G. Tzanankos *et al.*, MINOS+: a Proposal to FNAL to run MINOS with the medium energy NuMI beam, doi:10.2172/1028838, (2011).